ISSN 1688-2806

Universidad de la República
Facultad de Ingeniería

Tunable integrated radio frequency active resonators

Tesis presentada a la Facultad de Ingeniería de la Universidad de la República por

Andrés Seré

en cumplimiento parcial de los requerimientos para la obtención del título de Magister en Ingeniería Eléctrica.

Directores de Tesis

Fernando Silveira ..... Universidad de la República, Uruguay
Sylvain Bourdel ..... Instituto Politécnico de Grenoble, Francia

Tribunal

Leonardo Barboni ..... Universidad de la República, Uruguay
Pablo Monzón ..... Universidad de la República, Uruguay
Pietro Ferreira (Revisor Externo) ..... Université Paris-Saclay, Francia

Director Académico

Fernando Silveira ..... Universidad de la República, Uruguay

Montevideo
2022-07-01

Tunable integrated radio frequency active resonators, Andrés Seré.

ISSN 1688-2806

Esta tesis fue preparada en LaTeX usando la clase iietesis (v1.2).
Contiene un total de 120 páginas.
Compilada el 2022-07-01.
`http://iie.fing.edu.uy/`

Agradecimientos

En primer lugar agradezco al Prof. Fernando Silveira por su apoyo, paciencia y acompañamiento en todo el proceso, así como al Prof. Sylvain Bourdel por los valiosos intercambios a la distancia. A ambos por sus respuestas, pero también por sus preguntas.

A los miembros del tribunal, Prof. Leonardo Barboni, Prof. Pablo Monzón y Prof. Pietro Ferreira, les agradezco por su tiempo, por la lectura detenida y por los comentarios significativos que realizaron de este trabajo.

Agradezco el apoyo de la beca ANII POS_NAC_2019_1_157656, CSIC Universidad de la República y el proyecto STIC AmSud O2ERF.

Mi sincero agradecimiento, también, al Grupo de Microelectrónica y al Instituto de Ingeniería Eléctrica en su conjunto, por haber apoyado de diversas formas este trabajo. Especialmente a Mariana Siniscalchi y Nicolás Gammarano por su acompañamiento.

Finalmente, pero no menos importante, a familia y amigos, a quienes no precisan entenderlo todo para estar en todo, y muy especialmente a María Rosa; gracias.

This page was intentionally left blank.

Acknowledgements

First of all, I would like to thank Prof. Fernando Silveira for his support, patience and guidance throughout the process, as well as to Prof. Sylvain Bourdel for the valuable exchanges at a distance. To both of them for their answers, but also for their questions.

To the examiners, Prof. Pietro Ferreira, Prof. Pablo Monzón and Prof. Leonardo Barboni, I thank them for their time, for their careful reading and significant comments on this work.

I am grateful for the support of the grant ANII POS_NAC_2019_1_157656, CSIC Universidad de la República and the STIC AmSud O2ERF project.

My sincere thanks also goes to the Grupo de Microelectrónica and the Instituto de Ingeniería Eléctrica as a whole, for supporting this work in various ways. Especially to Mariana Siniscalchi and Nicolás Gammarano for their technical exchanges.

Last but not least, to family and friends, to those people who do not need to understand everything to be in everything, and most especially to María Rosa; thank you.

This page was intentionally left blank.

Resumen

Los avances en las comunicaciones celulares y su difundido uso han impulsado a los fabricantes de transceptores de radiofrecuencia a integrar sus productos y a disminuir el número de componentes fuera del chip. Además, la proliferación de diferentes estándares para sistemas de radiofrecuencia motiva la realización de diseños flexibles en los que un mismo circuito puede ser utilizado para diferentes esquemas de comunicación. En este contexto, los inductores activos constituyen una herramienta atractiva para la configuración del hardware en tiempo real.

Un inductor activo es un circuito sin inductores cuya impedancia vista de pequeña señal, en uno de sus puertos, es inductiva. Generalmente ocupa mucho menos área que su equivalente pasivo y ofrece posibilidad de sintonización. Las principales desventajas son el rango lineal limitado, el consumo de energía adicional y el ruido generado por el circuito.

En esta tesis los resonadores activos –construidos con inductores activos– son presentados en varios niveles. Partiendo de la motivación, la necesidad del girador como núcleo del resonador activo se convierte en algo natural. A partir de una definición generalizada del girador, pasando por el concepto de *resonador activo ideal*, este trabajo desarrolla el modelo de *resonador activo perfecto* como un primer paso, que incorpora la conductancia de salida de los transconductores, y un modelo de *resonador activo completo* como una aproximación más precisa que también tiene en cuenta los efectos capacitivos de entrada-salida de los dispositivos.

En el desarrollo del modelo se introdujeron definiciones clave y se obtuvieron algunos resultados novedosos. Este trabajo propone un *factor de calidad del girador* y muestra su relevancia en los diseños de resonadores activos (AR); limita, bajo ciertos supuestos, el máximo factor de calidad que el resonador activo puede alcanzar. También se analizan las relaciones de compromiso entre el ruido, la linealidad y el consumo de energía, y se contrastan con simulaciones.

El modelo de resonador activo perfecto ha demostrado ser muy potente para diseñar, analizar y comparar cualitativamente arquitecturas de resonadores activos, mientras que el modelo más completo brinda resultados precisos para realizar análisis computacional.

Por último, una de las arquitecturas estándar se probó en un diseño global de un amplificador de bajo ruido (LNA), colocándolo como etapa de entrada, proporcionando una red de adaptación sintonizable. Se demostró que los resultados del modelo siguen siendo válidos en este diseño completo que incorpora el transistor del LNA y las fuentes de corriente reales.

This page was intentionally left blank.

Abstract

The progress in cellular communications and its spread applications have propelled manufacturers of transceivers to integrate their products and decrease the number of off-chip components. Also, the proliferation of different standards of radio frequency systems motivates flexible designs in which the same circuit could be suitable for different communication schemes. In this context, active inductors become an attractive tool for real-time hardware customization.

An active inductor is an inductorless circuit whose small signal impedance, at one of its ports, is inductive. Generally, it occupies much less area than its passive counterpart, and offers tunability. The principal disadvantages are the limited linear range, the additional power consumption and the noise generated by the circuit.

In this thesis, active resonators—built with active inductors—were presented in several levels. Starting from the motivation, the need of the gyrator as the active resonator core becomes natural. From a generalized gyrator definition, passing through the *ideal active resonator* concept, this work develops the *perfect active resonator model* as a first step model which incorporates the output conductance of transconductors, and a *complete active resonator model* as a more accurate approach which also takes into account the input-output capacitive effects of the devices.

In the model development, key definitions were introduced, and some novel results were achieved. This work proposes a *gyrator quality factor* and proves its relevance in the active resonator (AR) designs; it limits, under certain assumptions, the maximum active resonator quality factor that can be achieved. The trade-offs between noise, linearity and power consumption are also analysed and contrasted with simulations.

The *perfect active resonator model* proved to be very powerful to design, analyse and compare qualitatively active resonator architectures, while the more complete model gives accurately results when performing computational analysis.

Finally, one of the standard architectures was proven in an overall design of a low noise amplifier (LNA) as its input stage, providing a tunable matching network. It is shown that the model results are still valid in this complete design that incorporates the LNA core transistor and real current sources.

This page was intentionally left blank.

Table of contents

Chapter 1

Introduction

The motivation of this work was to explore the active inductors in the context of the possibilities offered by new technologies, as the nanometre scale fully depleted silicon on insulator (FD-SOI).

The progress in cellular communications and its spread applications have propelled manufacturers of transceivers to integrate their products and decrease the number of off-chip components [1]. Also, the proliferation of different standards of radio frequency systems motivates flexible designs in which the same circuit could be suitable for different communication schemes. In this context, active inductors become an attractive tool for real-time hardware customization.

Active inductors could be placed at different stages of radio frequency systems. Most common applications are in tunable matching networks, as shown by Ma and Hu [2], Saberkari et al. [3] for low noise amplifiers (LNA) and Saberkari et al. [1] for power amplifiers (PA), and in tunable band-pass filters, used by Mehra et al. [4]. The example case in this work focused the design on a matching network as the input stage of an LNA.

An active inductor is an inductorless circuit whose small signal impedance, at one of its ports, is inductive. Generally, it occupies much less area than its passive counterpart, and offers tunability [5]. The principal disadvantages are the limited linear range, the additional power consumption and the noise generated by the circuit [6].

To achieve an inductive behaviour it is required some kind of *memory*, i.e. the current through the inductor (as happens with its passive counterpart). To get an analogue memory, it is needed a capacitor, so the current through the *simulated inductor* must be converted to the voltage at the capacitor terminals. Analogous, the capacitor voltage must be converted to a current at the *simulated inductor* terminals. The circuit that performs these operations is called a *gyrator*, was proposed by Tellegen [7] and is presented in Chapter 2. This approach, the understanding of the active inductor as a capacitor loaded gyrator, used here, is the traditional one and is also used by Belmas [8], Szczepkowski [9], Szczepkowski and Farrell [10, 11], Kaunisto [12] and Shin and Bult [13] among others.

However, there are other approaches to analyse an active inductor like see it as an amplifier with feedback network as used by Van Vliet et al. [14] and Leuzzi et al. [15], or those that see it as a particular Gm-C filter like Kuhn et al. [16] and Efthivoulidis et al. [17].

This work will use the gyrator as a two-port network (also called *quadripole*) with its mathematical definition, as is used by Szczepkowski [9] and Kaunisto [12]. The

former is focused on oscillators while the other does it on filters. Although Kaunisto [12] does a very deep analysis of noise, linearity and dynamic range, giving very interesting results, it doesn't provide a practical model to apply directly over a given architecture. Their work was focused on the comparison between active resonators and negative resistance filters. On the other side, Szczepkowski [9] propose the phase addition to the transconductors input, but focused his work on oscillators.

In contrast to those works, this one will focus on developing a practical model that will lead to explore and characterize new architectures, and shows the principal constraints of the design. The study will focus on active resonators, built with active inductors. Although the architectures of active inductors and active resonators are quite the same, the analysis of the former is over a frequency range in which the behaviour is inductive, while the latter (i.e. the one carried out in this work) is focused on the resonance frequency region.

This work is organized as follows: Chapter 2 analyses the gyrator concept and shows the operation of an active resonator; Chapter 3 develops the *perfect active resonator model* (PAR model) including basic trade-offs between noise, linearity and power consumption; Chapter 4 analyses the PAR model through simulations, applies it to two standard implementations of active inductors in MOS technology, proposes a more complete model and derives two new active resonator architectures; Chapter 5 uses one of the classic implementations of active inductors as a tunable matching network placed at the input of an LNA, with the aim to show an interesting result of the PAR model; finally, Chapter 6 concludes the thesis and raises future works.

Chapter 2

Ideal Active Resonator

This chapter presents the fundamentals of gyrators as the core of active resonators.

2.1 Tellegen's gyrator

The gyrator is a network element defined by Bernard D. H. Tellegen in 1948 that "completes the system of network elements" [7]. He was trying to answer the question "Besides the four known network elements are other, similar elements, conceivable?". Based the analysis in the following properties of the 2n-poles networks:

- the relation between voltages and currents is formed by a system of ordinary linear differential equations;
- the differential equations have constant coefficients;
- the 2n-pole is passive (i.e., it can deliver no energy);
- the 2n-pole satisfy the reciprocity relation (i.e., for the 2-pole case, the admittance matrix is symmetric);

Tellegen figured out that any two-pole and four-pole possessing these four properties can be realized by a network composed of the four known elements (resistor, capacitor, inductor and transformer).

To extend the possibilities, Tellegen dropped the fourth property and proposed the *ideal gyrator* as the fifth network element, with the symbol shown in Figure 2.1a and

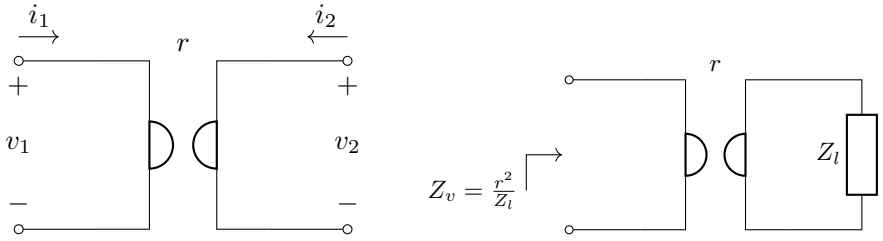

(a) Gyrator representation. (b) Gyrator of impedance.

Figure 2.1: The gyrator element.

described by the following equations:

$$\begin{cases} v_1 = -ri_2 \\ v_2 = ri_1 \end{cases} \tag{2.1}$$

where the parameter r is called the *gyration resistance*[1] and has units of Ω.

Figure 2.1b illustrates one of the most important property of the gyrator -at least for this work-; when an impedance Z_l is connected on port 2, the equivalent Thevenin impedance (from now on the *equivalent impedance*) on port 1 is

$$Z_v = \frac{r^2}{Z_l}. \tag{2.2}$$

2.1.1 A generalized gyrator

In the following chapters it will be needed a more general gyrator device, in which the two equations in 2.1 has different gyration resistance value. Also, it will be more practical to work with transconductances instead of resistances. Our *generalized gyrator* is shown in Figure 2.2, and is defined by the following pair of equations:

$$\begin{cases} i_a = g_{ma} v_b \\ i_b = -g_{mb} v_a \end{cases}. \tag{2.3}$$

Or, in an admittance matrix form:

$$[Y] = \begin{pmatrix} 0 & g_{ma} \\ -g_{mb} & 0 \end{pmatrix}. \tag{2.4}$$

Equation 2.3 is equivalent to 2.1 when

$$g_{ma} = g_{mb} = \frac{1}{r}. \tag{2.5}$$

A question must be answered: "is our *generalized gyrator* still a *gyrator*?" The answer is *yes*, it is still an *impedance gyrator* since equation 2.2 becomes

$$Z_v = \frac{1}{g_{ma} g_{mb} Z_l}. \tag{2.6}$$

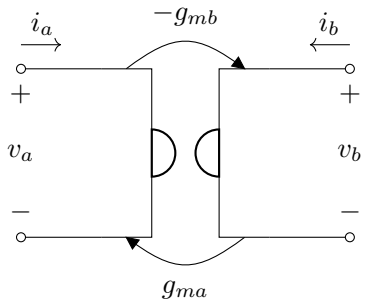

Figure 2.2: The *generalized gyrator*.

[1] In the original work, Tellegen uses the letter s for the *gyration resistance* parameter, but in this work is preferable the use of letter r to avoid confusions with the complex frequency.

However, the difference introduced in the definition is not a minor detail; the device is still linear and non-reciprocal, but it can be not lossless nor passive. In fact,

$$i_a v_a + i_b v_b = v_a v_b (g_{ma} - g_{mb}) \neq 0 \qquad \text{if } g_{ma} \neq g_{mb}. \tag{2.7}$$

In a more formal approach, if the total voltages and currents on ports a and b are $\tilde{V}_a$, $\tilde{I}_a$, $\tilde{V}_b$ and $\tilde{I}_b$ respectively, the transconductances are defined by the following equations

$$g_{ma} = \frac{\partial \tilde{I}_a}{\partial \tilde{V}_b} \qquad g_{mb} = \frac{\partial \tilde{I}_b}{\partial \tilde{V}_a} \tag{2.8}$$

with equation 2.3 being the *small signal model*.

From now on, the term *gyrator* will refer to the device shown in Figure 2.2.

2.1.2 Gyrator implementation

There are multiple forms to build a gyrator, sometimes including the passage to the mechanical domain through transducers. However, the most common implementation is schematized -ideally- in Figure 2.3 using two transconductance amplifiers with values g_{ma} and g_{mb} respectively. It can be seen easily that the admittance matrix becomes

$$\begin{pmatrix} 0 & g_{ma} \\ -g_{mb} & 0 \end{pmatrix} \tag{2.9}$$

and agrees with equation 2.3.

2.2 Ideal active resonator

The most common implementation of an active inductor is loading a gyrator with a capacitor, as shown in the circuit of Figure 2.4. It doesn't matter which port on the gyrator the capacitor is connected to; if it is connected to one port, the impedance seen from the other port is the same. In fact, the study will be based in a resonator (tank) circuit implemented by a gyrator loaded by one capacitor on each of its ports, as shown in Figure 2.5a. Figure 2.5b shows the ideal equivalent circuit seen from port a and Figure 2.5c shows the same circuit seen from port b. It is interesting to note that although the equivalent circuits are different, both are resonant circuits with the same resonance frequency:

$$\omega_0 = \frac{1}{\sqrt{LC}} = \sqrt{\frac{g_{ma} g_{mb}}{C_a C_b}} \tag{2.10}$$

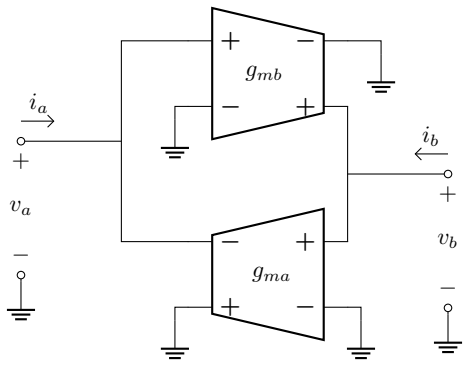

Figure 2.3: Gyrator implementation.

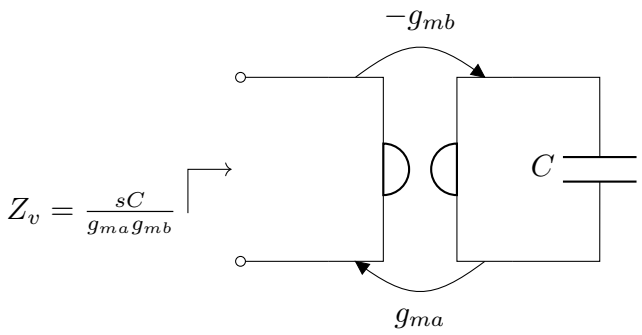

Figure 2.4: Active inductor implementation. A *generalized gyrator* loaded by a capacitor C. s is the complex frequency.

and infinite quality factor. Through this document, it will be used the letter a to denote the port from which the overall circuit is seen. If it is needed to swap the ports, the new g_{ma} will be the previous $-g_{mb}$ and the new g_{mb} will be the previous $-g_{ma}$.

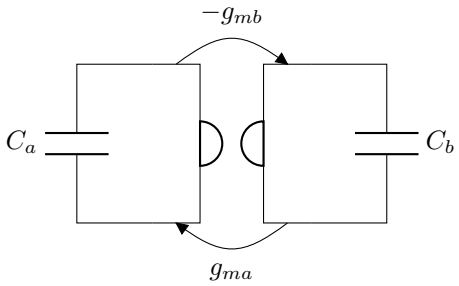

(a) Implementation of tank circuit.

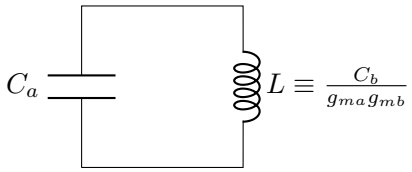

(b) Equivalent circuit seen from port a.

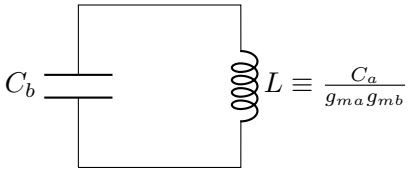

(c) Equivalent circuit seen from port b.

Figure 2.5: The gyrator application for a tank circuit implementation.

Chapter 3

Perfect active resonator

3.1 Motivation

Figure 3.1 shows two of the most simple implementations of gyrator circuits used to build active inductors. Neglecting the parasitic capacitances, the -small signal- admittance matrix of the *simple grounded active inductor* (Figure 3.1a) seen from port 1 is

$$[Y_{\text{sgai}}]_{p1} = \begin{pmatrix} g_{ds1} & g_{m1} \\ -g_{m2} & g_{ds2} + ng_{m2} \end{pmatrix} \tag{3.1a}$$

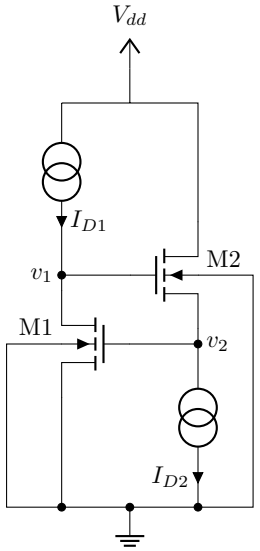

(a) Simple grounded active inductor proposed in Ismail et al. [18].

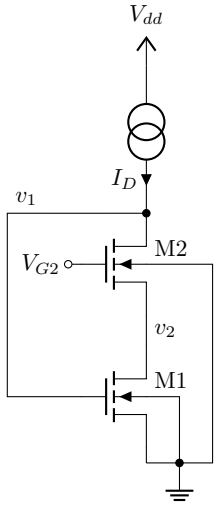

(b) Basic flipped-active inductor proposed in Yue Wu et al. [19].

Figure 3.1: Practical implementations examples of active inductors.

and for the *basic flipped active inductor* (Figure 3.1b) seen from port 1 is

$$[Y_{\text{bfai}}]_{p1} = \begin{pmatrix} g_{ds2} & -(ng_{m2} + g_{ds2}) \\ g_{m1} - g_{ds2} & g_{ds1} + g_{ds2} + ng_{m2} \end{pmatrix} \tag{3.1b}$$

where g_m is the gate transconductance, g_{ms} the source transconductance, g_{ds} the output conductance and n the slope factor. They will be referred as *active inductors* because they were proposed for that purpose and are used with capacitive load [18, 19].

The above matrices include non-idealities not considered in the diagonal matrix of equation 2.4. This fact leads to consider a more general model exposed in the following sections.

Some mathematical results, which equations are tagged with square brackets, are developed in the Appendix B.

3.2 The model

As it was shown in the previous section, real implementation of an active resonator will differ greatly from the circuit schematized in Figure 2.5a; it will contain several non-idealities that must be modelled. Many of these non-idealities (output conductance of each transconductor, for example), can be modelled adding a parallel resistor to each capacitor, as shown in Figure 3.2a.

The circuit of Figure 3.2a is a particular case of the more general circuit shown in Figure 3.2b where

$$Z_v = Z_a || \frac{1}{Z_b g_{ma} g_{mb}} \tag{3.2}$$

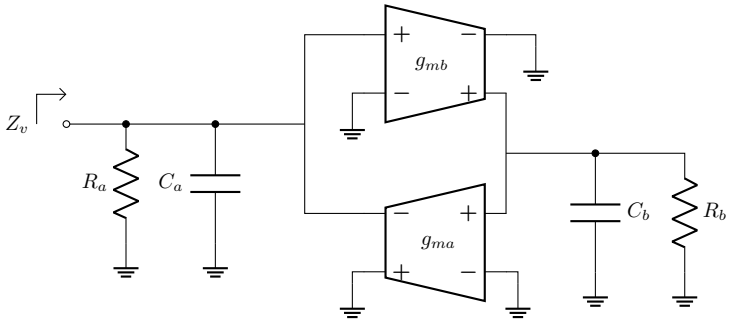

(a) Active resonator circuit considering output conductance of transconductors.

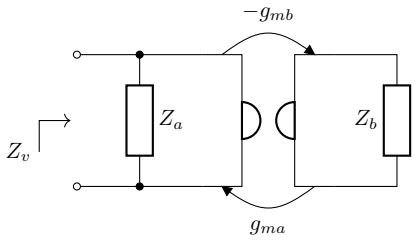

(b) Compact and general representation.

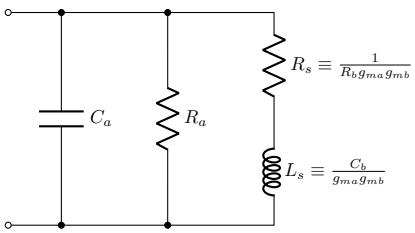

(c) Equivalent model.

Figure 3.2: A first approach to the model.

From the circuit in Figure 3.2a

$$Z_a = \frac{1}{C_a s} || R_a = \frac{R_a}{R_a C_a s + 1} \tag{3.3}$$

and

$$Z_b = \frac{1}{C_b s} || R_b = \frac{R_b}{R_b C_b s + 1}. \tag{3.4}$$

The impedance Z_b connected to port b, results in an impedance Z_{ba} seen from port a, as follows:

$$Z_{ba} = \frac{1}{Z_b g_{ma} g_{mb}} = \frac{C_b s}{g_{ma} g_{mb}} + \frac{1}{R_b g_{ma} g_{mb}}. \tag{3.5}$$

With the above expressions, the equivalent circuit is an RL series in parallel with an RC parallel, as shown in Figure 3.2c. As will be analysed in Section 3.2.4, the finite output conductance of the transconductors reduces the quality factor of the active inductor (through R_s) and further reduces the quality factor of the overall tank circuit (through R_a).

3.2.1 The active inductor

If capacitor C_a is removed from the circuit of Figure 3.2a the equivalent circuit becomes that of the Figure 3.3.

The equivalent steady-state impedance is

$$Z_L = R_a || (R_s + j\omega L_s) = \frac{R_a \left(1 + \frac{j\omega}{\omega_b}\right)}{x + 1 + \frac{j\omega}{\omega_b}} \tag{3.6}$$

where

$$R_s \equiv \frac{1}{R_b g_{ma} g_{mb}} \quad \text{and} \quad L_s \equiv \frac{C_b}{g_{ma} g_{mb}} \tag{3.7}$$

are the equivalent series resistance and inductance respectively,

$$\omega_b = \frac{1}{R_b C_b} \tag{3.8}$$

is the characteristic angular frequency on port b and

$$x = R_a g_{ma} R_b g_{mb} \tag{3.9}$$

is the product of the intrinsic gain of the transconductors, which is also equal to the relationship between R_a and R_s:

$$x = \frac{R_a}{R_s} = R_a g_{ma} R_b g_{mb} \tag{3.10}$$

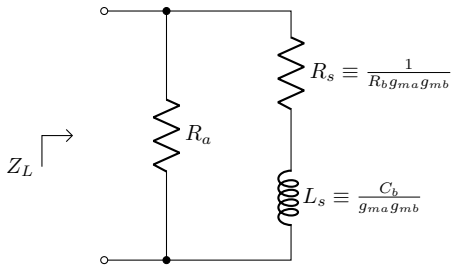

Figure 3.3: Equivalent circuit of the active inductor.

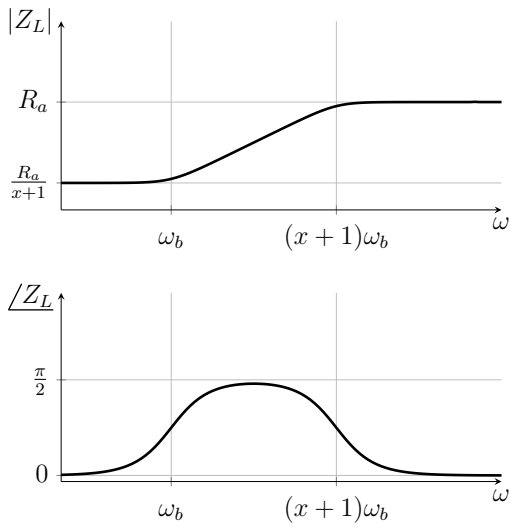

Figure 3.4: Bode plots of the equivalent impedance of the active inductor.

Figure 3.4 shows the Bode plots of Z_L. It can be seen that for frequencies below ω_b and above $(x+1)\omega_b$ the behaviour of the circuit is practically resistive, while for frequencies in the middle the behaviour is inductive. So, the region of interest is

$$\omega_b << \omega << (x+1)\omega_b \tag{3.11a}$$

which implies

$$\frac{\omega}{\omega_b} >> 1 \qquad \text{and} \qquad x >> 1 \tag{3.11b}$$

The above conditions will be used throughout the development of the model. Considering that x should be much greater than 1, the value of $x+1$ will be approximated by x.

3.2.2 The resonance frequency

If the capacitor C_a is placed back in the circuit terminals of Figure 3.3, the equivalent impedance becomes

$$Z_v = Z_L || \frac{1}{j\omega C_a} = \frac{R_a\left(1+\frac{j\omega}{\omega_b}\right)}{\left(1+\frac{j\omega}{\omega_a}\right)\left(1+\frac{j\omega}{\omega_b}\right)+x} \tag{3.12}$$

where

$$\omega_a = \frac{1}{R_a C_a} \tag{3.13}$$

is the characteristic angular frequency of port a. The impedance module, $|Z_v|$, for different values of C_a, is plotted in Figure 3.5 (where the approximation $x+1 \approx x$ was used). For low values of C_a (right part of the plot) the behaviour is resistive at low frequencies, then inductive, then resistive again and finally, for higher frequencies, the behaviour is capacitive. For high values of C_a (left part of the plot) the behaviour is resistive and then capacitive (like that of a parallel RC circuit). At middle values of

C_a, where $\omega_b < \frac{1}{\sqrt{L_s C_a}} < x\omega_b$, the circuit resonates. The resonance frequency can be calculated by cancelling the imaginary part of Z_v in equation 3.12, obtaining:

$$\omega_0^2 = x\omega_a\omega_b - \omega_b^2. \tag{3.14}$$

Using the definitions

$$x = g_{ma}R_a g_{mb}R_b \qquad \omega_a = \frac{1}{R_a C_a} \qquad \omega_b = \frac{1}{R_b C_b} = \frac{R_s}{L_s} \tag{3.15}$$

the equation 3.14 can be written

$$\omega_0^2 = \frac{1}{L_s C_a} - \frac{R_s^2}{L_s^2}, \tag{3.16}$$

and it becomes clear that the left part of equation 3.14 corresponds to the resonance frequency of a parallel RLC circuit while the right part responds to the effect of the series resistance of the equivalent circuit which can be neglected if $\omega_0 >> \omega_b$. Under this assumption, resonance frequency can be written

$$\omega_0^2 \approx x\omega_a\omega_b. \tag{3.17}$$

3.2.3 Observed impedance at resonance frequency

At resonance frequency, the equivalent impedance is real. Evaluating 3.12 at $\omega = \omega_0$ and substituting ω_a from equation 3.14 gives

$$R_v = Z_v(\omega = \omega_0) = \frac{R_a\left(1 + \frac{\omega_0^2}{\omega_b^2}\right)}{x + 1 + \frac{\omega_0^2}{\omega_b^2}}. \tag{3.18}$$

The plot of R_v was superposed in black in Figure 3.5; it has a double zero at $\omega = \omega_b$ and a double pole at $\omega = \omega_b\sqrt{x}$.

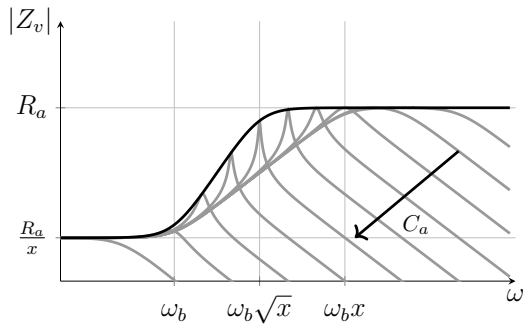

Figure 3.5: Plot of the resonator equivalent impedance module varying the value of C_a (gray). In black is the equivalent impedance at resonance frequency. The arrow indicates the direction of increasing C_a.

3.2.4 Quality factor

Quality factor of a device can be defined as 2π − times the ratio of the maximum (peak) energy stored in one cycle to the energy dissipated in the same cycle. And is, naturally, frequency dependent. In the Figure 3.2c, the equivalent circuit shows a resistor R_a in parallel with the capacitor C_a and a resistor R_s in series with the inductor L_s. To calculate the quality factor, both parts can be considered separated; the parallel RC has a quality factor

$$Q_C = \omega C_a R_a = \frac{\omega}{\omega_a} \tag{3.19}$$

and the series RL has a quality factor

$$Q_L = \frac{\omega L_s}{R_s} = \frac{\omega}{\omega_b} \tag{3.20}$$

so, it can be shown that the quality factor of the whole circuit becomes the *parallel* of Q_C and Q_L [20]:

$$Q = \frac{1}{\frac{1}{Q_C} + \frac{1}{Q_L}} = \frac{\omega}{\omega_a + \omega_b}. \tag{3.21}$$

Evaluating 3.21 at $\omega = \omega_0$ and substituting ω_a from equation 3.14 follows

$$Q(\omega_0) = \frac{x\frac{\omega_0}{\omega_b}}{\frac{\omega_0^2}{\omega_b^2} + x + 1} \approx \frac{x\frac{\omega_0}{\omega_b}}{\frac{\omega_0^2}{\omega_b^2} + x} \tag{3.22}$$

which is plotted in Figure 3.6. The maximum can be calculated by cancelling its derivative and results in

$$\omega_0^2\big|_{Q_{max}} = \omega_b^2(x+1) \approx \omega_b^2 x \tag{3.23}$$

which substituted in 3.14 implies

$$\omega_a = \omega_b \tag{3.24}$$

and the maximum value of Q is

$$Q_{\max} = \frac{x}{2\sqrt{x+1}} \approx \frac{\sqrt{x}}{2} \tag{3.25}$$

which motivates the denomination of *gyrator quality factor* to the parameter x. This is an important result because x is the product of the intrinsic gain of the transconductors, so they limit the maximum quality factor that can be reached. In other words, to increase the quality factor it is necessary to increase the intrinsic gain of the transconductors.

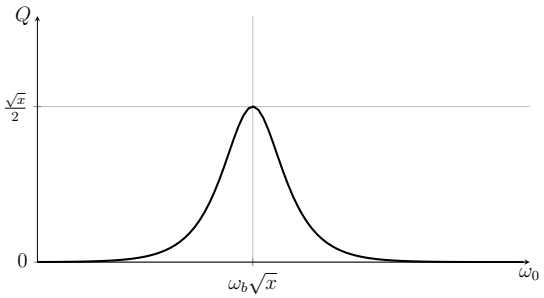

Figure 3.6: Plot of the quality factor as a function of the resonance frequency, with fixed values of ω_b and x.

3.2.5 Noise analysis

One of the principal disadvantages of active inductors in comparison of the passive counterpart is the poor noise performance [6, 5]. How the transistors thermal noise is translated to the gyrator ports? Figure 3.7 shows four possible locations of noise power source.

It is easy to see that a noise power source[1] located at V_{na}^2 is equivalent to a noise power source located at I_{nb}^2 with

$$I_{nb}^2(f) = g_{mb}^2 V_{na}(f)^2. \tag{3.26}$$

The same applies to the equivalence between V_{nb}^2 and I_{na}^2 with

$$I_{na}^2(f) = g_{ma}^2 V_{nb}(f)^2. \tag{3.27}$$

Also, if the circuit is "seen" from port a[2], the current noise power source I_{nb}^2 can be translated to a voltage noise power source on V_{nb}^2 with

$$V_{nb}^2(f) = |Z_b|^2 I_{nb}^2. \tag{3.28}$$

A common approach to model the noise of an active inductor is assuming the transconductances are obtained with single transistors and each one has an equivalent input power noise voltage $V_{gni}^2(f)$ assumed constant (white noise) and neglecting the flicker noise [21]. If it is assumed transconductances obtained with saturated single transistors in weak inversion, the power spectral density (PSD) of noise is[3] [24]

$$V_{gni}^2(f) = \frac{2k_B T n}{g_m} \tag{3.29}$$

where k_B is the Boltzman constant, T is the temperature in Kelvins, n is the *slope factor* and g_m the corresponding transconductance of the transistors.

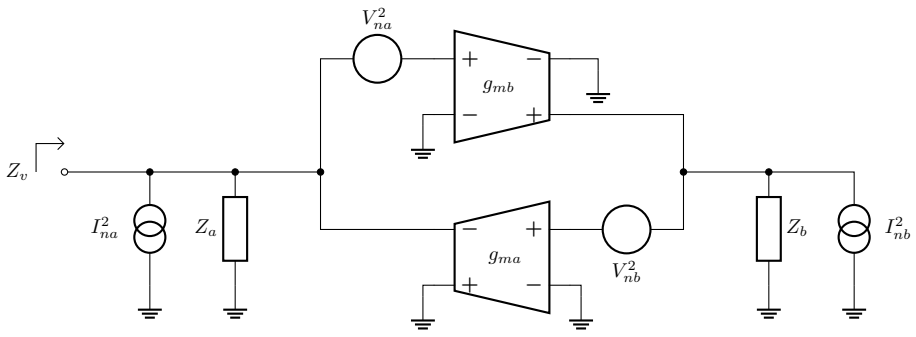

Figure 3.7: Possible locations of noise power sources.

[1] There is an abuse of notation where V_{ni}^2 and I_{nk}^2 are noise power sources with noise power spectral density of values $V_{ni}^2(f)$ and $I_{nk}^2(f)$ respectively.

[2] This assumption is important since the equivalence is not valid if the noise is measured on the Z_b terminals.

[3] A concern could be whether shot noise must be also included as a separate noise contribution. However, this is not necessary since it is already included in the white noise component [22, 23].

With the above assumption, there are only two noise power sources located at V_{na}^2 and V_{nb}^2, with values

$$V_{na}^2(f) = \frac{2k_BTn_b}{g_{mb}} \qquad V_{nb}^2(f) = \frac{2k_BTn_a}{g_{ma}} \tag{3.30}$$

with units of V^2/Hz. Using the relations 3.26, 3.27 and 3.28, the noise can be modelled by a single current noise power source of value

$$I_n^2(f) = V_{na}^2 g_{ma}^2 g_{mb}^2 |Z_b|^2 + V_{nb}^2 g_{ma}^2 \tag{3.31}$$

located in I_{na}^2 of Figure 3.7, i.e. in terminals of the active resonator. Incorporating the value of Z_b from equation 3.4, equation 3.31 becomes

$$I_n^2(\omega) = V_{na}^2 g_{ma}^2 g_{mb}^2 \frac{R_b^2}{1+\frac{\omega^2}{\omega_b^2}} + V_{nb}^2 g_{ma}^2. \tag{3.32}$$

Sometimes is useful to know the PSD of the noise voltage (V_n^2) while sometimes is better to know the PSD of the noise current (I_n^2). For example, for passive resistors, a larger resistance implies larger V_n^2 but smaller I_n^2. For a useful comparison and easier analysis, could be better to use the *normalized power spectral density of noise* defined by

$$\frac{S_n}{S_{n0}} \equiv \frac{S_{nv}}{S_{nv0}} = \frac{S_{ni}}{S_{ni0}} \tag{3.33}$$

where S_{nv} and S_{ni} are the PSD of noise (voltage and current respectively) generated by the active resonator, and S_{nv0} and S_{ni0} are the PSD of noise (voltage and current respectively) generated by the passive counterpart (with parallel resistor equal R_v). The quantity defined by equation 3.33 will be of particular interest and, in Section 3.3.1, it will be proved that, under certain assumptions, for an active resonator placed at the input of an LNA, its noise factor can be written as:

$$F = 1 + \frac{S_n}{S_{n0}} \tag{3.34}$$

With the above definitions, the normalized PSD of noise can be calculated as

$$\frac{S_n}{S_{n0}} = I_n^2(f)\frac{R_v}{4k_BT} = \frac{n}{2} g_{ma} R_a \frac{\frac{R_b}{R_a}x + 1 + \frac{\omega_0^2}{\omega_b^2}}{x + 1 + \frac{\omega_0^2}{\omega_b^2}} \approx \frac{n}{2} g_{ma} R_a \frac{\frac{R_b}{R_a}x + \frac{\omega_0^2}{\omega_b^2}}{x + \frac{\omega_0^2}{\omega_b^2}}. \tag{3.35}$$

Equation 3.35 is a very important result; the PSD of noise at resonance frequency is independent of the value of g_{mb}. g_{mb} could be increased, increasing also the value of x and therefore the value of Q with small impact the generated noise by the active resonator. This refutes the idea that noise of active resonators grows with Q, proposed by several works, in particular by [21], which only holds when both transconductances are imposed to be fixed.

If the value of ω_0 which maximizes Q is used, equation 3.35 is reduced to

$$\frac{S_n}{S_{n0}} = \frac{n}{2}(R_a + R_b) g_{ma}. \tag{3.36}$$

However is valid to ask whether the noise can be reduced at the cost of working in a non-optimal point for the quality factor. Equation 3.35 has a double pole in $\omega_b\sqrt{x}$ and a double zero in $\omega_b\sqrt{x\frac{R_b}{R_a}}$. The behaviour of S_n/S_{n0} is sketched in Figure 3.8

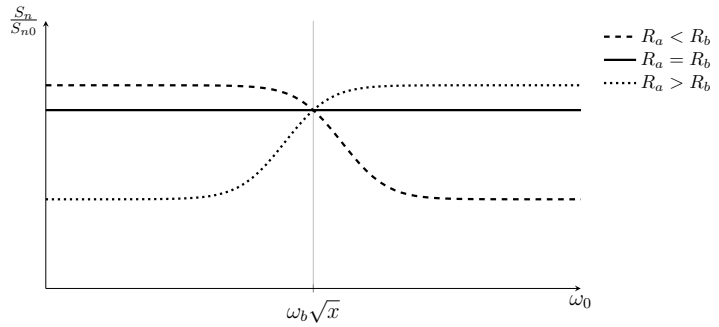

Figure 3.8: Behaviour of the normalized PSD of noise.

for three different relationships between R_a and R_b. If $R_a < R_b$, for $\omega_0 < \omega_b\sqrt{x}$ the normalized PSD of noise could be lower, while if $R_a > R_b$ the same applies for $\omega_0 > \omega_b\sqrt{x}$. Is it better to reduce noise at the cost of reducing Q? The answer is "yes", at least, it makes sense because noise decrease at 20 dB/dec while Q decrease only at 10 dB/dec; in other words, moving ω_0 a factor of 2 from $\omega_b\sqrt{x}$ implies a reduction of the normalized PSD of noise by a factor of 4 but only reduce the value of Q (or increase the bandwidth) by a factor of 2. To complete this discussion, it can be defined a figure of merit as

$$\frac{\hat{S}_n}{S_{n0}} \equiv \frac{S_n}{S_{n0}}\frac{1}{Q} = \frac{n}{2}g_{ma}R_a\frac{\frac{R_b}{R_a}x + 1 + \frac{\omega_0^2}{\omega_b^2}}{x\frac{\omega_0}{\omega_b}} \approx \frac{n}{2}g_{ma}R_a\frac{\frac{R_b}{R_a}x + \frac{\omega_0^2}{\omega_b^2}}{x\frac{\omega_0}{\omega_b}} \tag{3.37}$$

which has the advantage that includes the bandwidth ($\propto \frac{1}{Q}$). The equation 3.37 is sketched in Figure 3.9 for three different relations of R_a/R_b. The minimum is at

$$\omega_{\min}^2 = \left(x\frac{R_b}{R_a} + 1\right)\omega_b^2 \approx \omega_b\sqrt{x\frac{R_b}{R_a}} \tag{3.38}$$

and its value is

$$\left.\frac{\hat{S}_n}{S_{n0}}\right|_{\omega=\omega_{\min}} = ng_{ma}\sqrt{\frac{R_aR_b}{x} + \frac{R_a^2}{x^2}} \approx ng_{ma}\sqrt{\frac{R_aR_b}{x}} = n\frac{g_{ma}}{g_{mb}}. \tag{3.39}$$

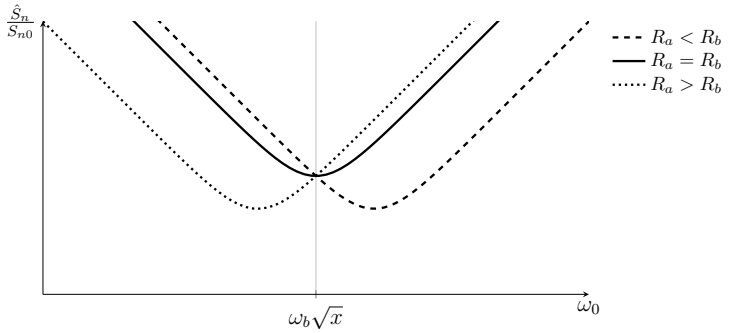

Figure 3.9: Behaviour of the figure of merit $\frac{\hat{S}_n}{S_{n0}}$.

In conclusion, it could be better to work in an operating point different of $\omega_0 = \omega_b\sqrt{x}$. Nevertheless, this last analysis was carried out towards the end of this work so, in this document, the chosen operating point will be $\omega_0 = \omega_b\sqrt{x}$.

3.2.6 The two-port network approach

The model exposed in previous subsections can be developed, also, over the two-port network shown in Figure 3.10. The admittance matrix of the two-port network is

$$[Y] = \begin{bmatrix} y_{aa} & y_{ab} \\ y_{ba} & y_{bb} \end{bmatrix} = \begin{bmatrix} \frac{1}{R_a}\left(1 + j\frac{\omega}{\omega_a}\right) & g_{ma} \\ -g_{mb} & \frac{1}{R_b}\left(1 + j\frac{\omega}{\omega_b}\right) \end{bmatrix} \tag{3.40}$$

where

$$\omega_a = \frac{1}{R_a C_a} \qquad \text{and} \qquad \omega_b = \frac{1}{R_b C_b}.$$

The Thevenin equivalent admittance from port a can be calculated as

$$\frac{1}{Z_v(j\omega)} = Y_v(j\omega) = \frac{i_a}{v_a} = y_{aa} - \frac{y_{ab}y_{ba}}{y_{bb}} = G + jB \tag{3.41}$$

where G and B are the conductance and susceptance given by the following expressions

$$\begin{cases} G = \dfrac{1}{R_a}\left[1 + \dfrac{x}{1 + \frac{\omega^2}{\omega_b^2}}\right] \\ B = \dfrac{1}{R_a}\left[\dfrac{\omega}{\omega_a} - \dfrac{x\frac{\omega}{\omega_b}}{1 + \frac{\omega^2}{\omega_b^2}}\right] \end{cases} \tag{3.42}$$

where

$$x = R_a g_{ma} R_b g_{mb}$$

as was defined in Section 3.2.1.

The resonance frequency ω_0 can be calculated by cancelling the susceptance B of equation 3.42:

$$B = 0 \Longleftrightarrow \frac{\omega_0}{\omega_a} - \frac{x\frac{\omega_0}{\omega_b}}{1 + \frac{\omega_0^2}{\omega_b^2}} = 0 \Longleftrightarrow \omega_0^2 = x\omega_a\omega_b - \omega_b^2. \tag{3.43}$$

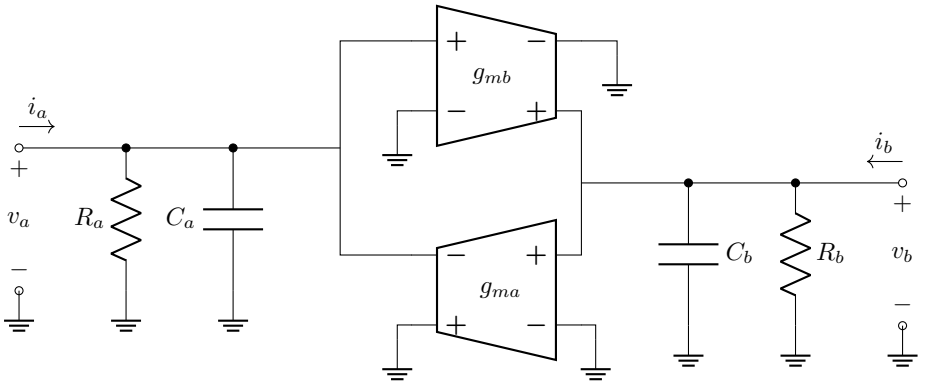

Figure 3.10: Two-port network model of the active resonator.

The equivalent impedance is simply

$$Z_v = \frac{1}{G} = \frac{R_a\left(1+\frac{\omega^2}{\omega_b^2}\right)}{x+1+\frac{\omega^2}{\omega_b^2}}. \tag{3.44}$$

The quality factor Q can be calculated as

$$Q = \frac{R_p}{\omega L_p} = R_p \omega C_p \tag{3.45}$$

where R_p is the equivalent parallel resistance $(1/G)$, L_p is the equivalent parallel inductance and C_p is the parallel capacitance. From equation 3.42, if $\omega_0 >> \omega_b$,

$$L_p \equiv \frac{R_a}{x\omega_b} \qquad C_p \equiv \frac{1}{R_a\omega_a} \tag{3.46}$$

then

$$Q(\omega_0) = R_p\omega_0 C_p = \frac{1}{G}\omega_0\frac{1}{R_a\omega_a} = \frac{\frac{\omega_0}{\omega_a}\left(1+\frac{\omega_0^2}{\omega_b^2}\right)}{x+1+\frac{\omega_0^2}{\omega_b^2}} = \frac{x\omega_0\omega_b}{\omega_0^2+(x+1)\omega_b^2}. \tag{3.47}$$

The noise can be analysed from the output current noise power of each transconductor as shown in Figure 3.11. With

$$I_{na}^2 = 2nk_BTg_{ma} \quad \text{and} \quad I_{nb}^2 = 2nk_BTg_{mb}, \tag{3.48}$$

I_n^2 results in

$$I_n^2 = I_{na}^2 + \left|\frac{y_{ab}}{y_{bb}}\right|^2 I_{nb}^2 = 2nk_BT\left[g_{ma} + \frac{g_{ma}^2R_b^2}{1+\frac{\omega^2}{\omega_b^2}}g_{mb}\right] \tag{3.49}$$

which is equivalent to equation 3.32.

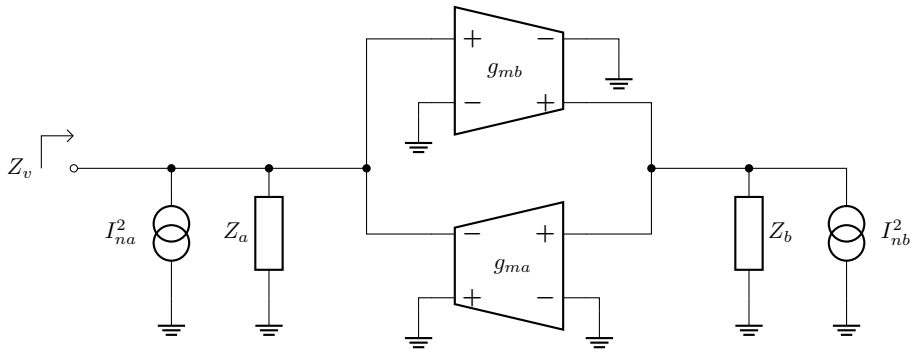

Figure 3.11: Simple noise model using the two-port network approach.

3.3 Noise, linearity and power consumption: the tradeoffs

Based on the model presented previously, this section will try to show some tradeoffs associated with the design of active resonator circuits, in particular applied to use in low noise amplifiers (LNA). There is no intention to show strong constraints, but the idea is to expose the relations between the relevant parameters.

The analysis will be based in the LNA schematized in Figure 3.12 where R_{in} is the input resistance (typically 50 Ω), R_{out} the output resistance (or load resistance), and g_m an ideal noiseless transconductance of value g_m, with infinity input and output resistance. The signal power gain is

$$G = g_m^2 R_{out}^2. \tag{3.50}$$

The idea is to replace one of the resistances by an active resonator circuit with the aim to build a frequency filter. It will be analysed both cases, replacing R_{in} or R_{out}, separately.

Every result will be evaluated at $\omega_0 = \omega_b\sqrt{x}$, the operating point at which the quality factor is maximized (see equation 3.23).

In this work the linearity will be quantified by the 3rd order Intercept Input Point (IIP3). It is a figure of merit usually applied to quantify the linearity of an RF block. It corresponds to the input power where the amplitude of the third harmonic at the output would equal the amplitude of the fundamental [25]. To analyse the linearity, the active resonator circuit will be modelled by the schematic of Figure 3.10 and using the matrix of equation 3.40. There are, at least, two nodes (v_a and v_b) whose maximum voltage range will determine the IIP3. The relationship between the amplitude signal in each port at $\omega_0 = \omega_b\sqrt{x}$ is

$$\left|\frac{v_b}{v_a}\right| = \left|\frac{y_{ba}}{y_{bb}}\right| = \left|\frac{g_{mb}R_b}{\sqrt{1+\frac{\omega_0^2}{\omega_b^2}}}\right| \approx \left|\frac{g_{mb}R_b}{\sqrt{x}}\right| = \left|\frac{g_{mb}R_b}{g_{ma}R_a}\right|^{\frac{1}{2}}. \tag{3.51}$$

If $\hat{v}_a$ and $\hat{v}_b$ are the maximum voltage swing in each port (with a strong limit), then the voltage swing of the active resonator will be

$$\hat{v}_{ar} = \min\left\{\hat{v}_a; \left|\frac{g_{ma}R_a}{g_{mb}R_b}\right|^{\frac{1}{2}} \hat{v}_b\right\}. \tag{3.52}$$

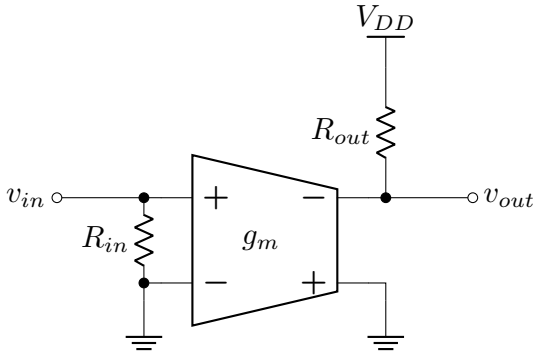

Figure 3.12: Simple LNA model used to analyse the tradeoffs.

If $\omega_0 = \omega_b\sqrt{x}$ then $Q \approx \frac{\sqrt{x}}{2}$, so the above equation can be written as

$$\hat{v}_{ar} = \min\left\{\hat{v}_a; \left|\frac{g_{ma}R_a}{2Q}\right| \hat{v}_b\right\}. \tag{3.53}$$

3.3.1 Active resonator at the input of the LNA

If R_{in} is replaced by an active resonator circuit, the voltage v_{in} will be v_a. Then, using equation 3.53, can be considered that

$$\text{IIP3} \propto \frac{\hat{v}_{in}^2}{R_{in}} = \min\left\{\frac{\hat{v}_a^2}{R_{in}} \; ; \; \left|\frac{g_{ma}R_a}{2Q}\right|^2 \frac{\hat{v}_b^2}{R_{in}}\right\}. \tag{3.54}$$

The *spot noise factor* F (i.e. considering a 1 Hz bandwidth [26]) is

$$F = \frac{\text{SNR}_i}{\text{SNR}_o} = \frac{S_i}{S_o}\frac{N_o}{N_i} = \frac{1}{G}\frac{N_iG + \frac{S_n}{S_{n0}}S_{n0}G}{N_i} = 1 + \frac{S_n}{S_{n0}} \tag{3.55}$$

where was used, by definition of both, that $S_{n0} = N_i$.

Evaluated at the frequency that maximizes the quality factor, the normalized power spectral density (PSD) of noise is

$$\frac{S_n}{S_{n0}} = \frac{n}{2}(R_a + R_b)g_{ma}. \tag{3.56}$$

Considering only the first term (both terms will be considered later), it becomes

$$\frac{S_n}{S_{n0}} \approx \frac{n}{2}R_a g_{ma} = F - 1 \tag{3.57}$$

where the spot noise factor was used. Substituting the last relation in equation 3.54 results in

$$\text{IIP3} \propto \min\left\{\frac{\hat{v}_a^2}{R_{in}} \; ; \; \frac{(F-1)^2}{Q^2}\frac{\hat{v}_b^2}{nR_{in}}\right\}. \tag{3.58}$$

The above expression is sketched in Figure 3.13. The design region is below-right the corresponding curve. If Q is greater, the design region moves to right (noisier design), but always has a maximum IIP3 determined by the voltage swing of port a.

If each transconductor is made by a single transistor with a given inversion level, and, again, using $\omega_0 = \omega_b\sqrt{x}$, the equivalent impedance at resonance frequency is

$$R_v = \frac{R_a}{2} = \frac{1}{2\left(\frac{g_{ds}}{I_D}\right)_a I_{Da}} \Longrightarrow I_{Da} = \frac{1}{2\left(\frac{g_{ds}}{I_D}\right)_a R_v}. \tag{3.59}$$

Then, the second part of the normalized PSD of noise (equation 3.56) becomes

$$R_b g_{ma} = \frac{\left(\frac{g_m}{I_D}\right)_a I_{Da}}{\left(\frac{g_{ds}}{I_D}\right)_b I_{Db}} = \frac{\frac{\left(\frac{g_m}{I_D}\right)_a}{\left(\frac{g_{ds}}{I_D}\right)_a}}{2\left(\frac{g_{ds}}{I_D}\right)_b I_{Db}R_v} = \frac{R_a g_{ma}}{2\left(\frac{g_{ds}}{I_D}\right)_b I_{Db}R_v}. \tag{3.60}$$

The term $I_{Db}R_v$ can be written in terms of the total current I_{Dt}:

$$I_{Dt} = I_{Da} + I_{Db} = \frac{1}{2\left(\frac{g_{ds}}{I_D}\right)_a R_v} + I_{Db} \Longrightarrow I_{Db}R_v = I_{Dt}R_v - \frac{1}{2\left(\frac{g_{ds}}{I_D}\right)_a}. \tag{3.61}$$

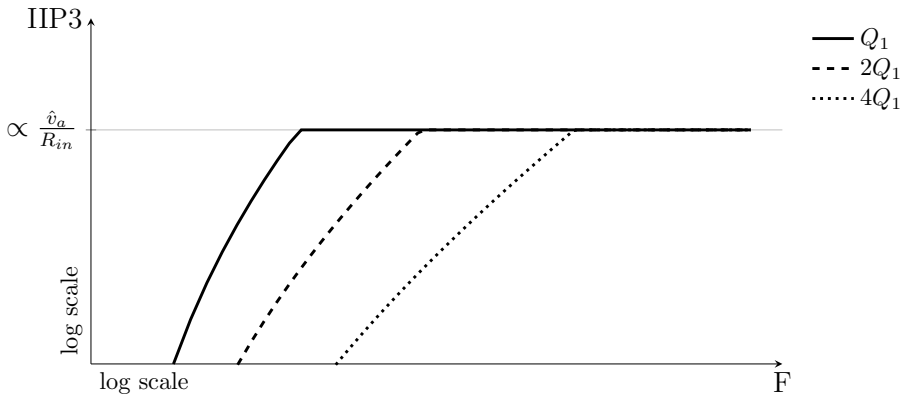

Figure 3.13: Sketch of equation 3.58 showing the tradeoffs between IIP3, F and Q. The sketch is for three different values of quality factor Q (normalized to an arbitrary value of Q_1). The design region is below-right the corresponding curve. IIP3 is the 3rd order input intercept point, F is the spot noise factor, $\hat{v}_a$ is the maximum voltage swing of node a and R_{in} the input resistance of the LNA.

Then, the normalized PSD of noise becomes

$$\frac{S_n}{S_{n0}} = \frac{n}{2}(R_a + R_b)g_{ma} = \frac{n}{2}g_{ma}R_a \left\{ 1 + \frac{1}{2\left(\frac{g_{ds}}{I_D}\right)_b \left[I_{Dt}R_v - \frac{1}{2\left(\frac{g_{ds}}{I_D}\right)_a} \right]} \right\} \tag{3.62}$$

and the IIP3, considering only the limitation at port b (second part of the expression in 3.54), is

$$\text{IIP3} \propto \frac{(F-1)^2}{Q^2} \left[\frac{I_{Dt}R_v - \frac{1}{2\left(\frac{g_{ds}}{I_D}\right)_a}}{I_{Dt}R_v + \frac{1}{2\left(\frac{g_{ds}}{I_D}\right)_b} - \frac{1}{2\left(\frac{g_{ds}}{I_D}\right)_a}} \right]^2 \frac{\hat{v}_b^2}{nR_{in}}. \tag{3.63}$$

Equation 3.63 is sketched in Figure 3.14 The design region is below-right the corresponding curve. If Q is greater, the design will need more current, but the performance $\text{IIP3}/(F-1)^2$ always has a maximum determined by the value of $\hat{v}_b^2/Q^2$.

3.3.2 Active resonator at the output of the LNA

The analysis for substituting the output resistance by an active resonator circuit is analogous to that for substituting the input resistance.

In this case, v_a is the output voltage so

$$\text{IIP3} \propto \frac{\hat{v}_{in}^2}{R_{in}} = \frac{\hat{v}_{out}^2}{GR_{in}} = \min\left\{ \frac{\hat{v}_a^2}{GR_{in}} \; ; \; \left|\frac{g_{ma}R_a}{2Q}\right|^2 \frac{\hat{v}_b^2}{GR_{in}} \right\}. \tag{3.64}$$

The spot noise factor is

$$F = \frac{\text{SNR}_i}{\text{SNR}_o} = \frac{S_i}{S_o}\frac{N_o}{N_i} = \frac{1}{G}\frac{N_iG + \frac{S_n}{S_{n0}}S_{n0}}{N_i} = 1 + \frac{S_n}{S_{n0}}\frac{1}{g_m R_{in}\sqrt{G}} \tag{3.65}$$

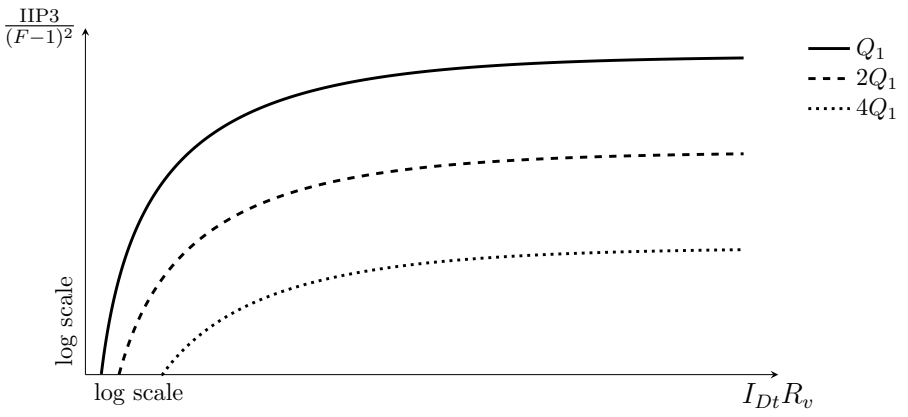

Figure 3.14: Sketch of equation 3.63 for three different values of the quality factor Q (normalized to an arbitrary value of Q_1). The design region is below-right the corresponding curve. IIP3 is the 3rd order input intercept point, F is the spot noise factor, I_{Dt} is the total current of the active resonator circuit and R_v is the equivalent impedance of the active resonator circuit.

because

$$G = g_m^2 R_L^2 \Longrightarrow R_L^2 = \frac{G}{g_m^2} \Longrightarrow \frac{S_{n0}}{N_i} = \frac{R_L}{R_{in}} = \frac{\sqrt{G}}{g_m R_{in}}. \tag{3.66}$$

Doing a similar analysis that done in the previous subsection, IIP3 satisfies

$$\text{IIP3} \propto \min\left\{ \frac{\hat{v}_a^2}{G R_{in}} \; ; \; \frac{(F-1)^2}{Q^2} g_m^2 R_{in} \frac{\hat{v}_b^2}{n} \right\}. \tag{3.67}$$

The behaviour of the equation 3.67 is the same to that for the first case, but with a lower horizontal limit imposed by the first term of the minimum expression.

The analysis considering both terms of normalized PSD of noise is analogous; the equation 3.62 is still valid. The IIP3, considering only the second term of the minimum expression in 3.64 is

$$\text{IIP3} \propto \frac{(F-1)^2}{Q^2} \left[\frac{I_{Dt}R_v - \frac{1}{2\left(\frac{g_{ds}}{I_D}\right)_a}}{I_{Dt}R_v + \frac{1}{2\left(\frac{g_{ds}}{I_D}\right)_b} - \frac{1}{2\left(\frac{g_{ds}}{I_D}\right)_a}} \right]^2 g_m^2 R_{in} \frac{\hat{v}_b^2}{n}. \tag{3.68}$$

The behaviour of equation 3.68 (i.e. placing the active resonator at the output of the LNA) is the same as the equation 3.63 sketched in Figure 3.14 (i.e. placing the active resonator at the input of the LNA). The only difference is the term $1/R_{in}$ in the first one, replaced by $g_m^2 R_{in}$ in the last one.

In conclusion, most the cases, is more convenient to put the active resonator filter at the input instead of at the output, because the maximum IIP3 that can be achieved by the former is greater than that can be achieved by the last one. There is an example of that convenience at the end of Section 5.2.2. The exception could be when

$$\frac{1}{R_{in}} \ll g_m^2 R_{in} \quad \Longrightarrow \quad g_m R_{in} \gg 1 \tag{3.69}$$

what, if $R_{in} = 50\ \Omega$, would imply a very high current consumption in the LNA transistor.

The most relevant cause for the above conclusion were the strong limits imposed for the IIP3 in equations 3.54 and 3.64. Also, the bias current dependence for the noise factor (equations 3.55 and 3.65) is much stronger (i.e. g_m dependence) than that for the IIP3 (i.e. the intrinsic gain $g_{ma}R_a$). Finally, this analysis is incomplete; it needs to incorporate the linearity and noise of the transconductance g_m. This last aspect will be analysed later, in sections 4.5 and 4.6.

Chapter 4

Architecture analysis and model limitations

This chapter gives an overview of some architectures and shows how to apply the model presented in Chapter 3. The circuits are simulated in a 28 nm FD-SOI technology [27] and the results are contrasted with the model predictions. This process will highlight some limitations of the model that will be addressed by adding some complexity to it. The simulation details are reported in the Appendix C and referenced here with the simulation number.

4.1 Applying the model

As was shown on Section 3.1, two of the most common and simple implementations of gyrators (and therefore, of active resonators) are the *simple grounded active inductor* (SGAI) proposed by Ismail et al. [18] and schematized in Figure 4.1a, and the *basic flipped active inductor* (BFAI) proposed by Yue Wu et al. [19] and schematized in Figure 4.1b.

Appendix A.1 shows an interesting approach to create an equivalency between the two-port network of Figure 3.10 and the circuits of Figure 4.1. However, in this chapter, the model will be applied from the *generic* admittance matrix:

$$[Y] = \begin{pmatrix} y_{aa} & y_{ab} \\ y_{ba} & y_{bb} \end{pmatrix} \tag{4.1a}$$

which will have its correspondence with the admittance matrix of the circuit seen by each port, either 1:

$$[Y]_{p1} = \begin{pmatrix} y_{aa} & y_{ab} \\ y_{ba} & y_{bb} \end{pmatrix} = \begin{pmatrix} y_{11} & y_{12} \\ y_{21} & y_{22} \end{pmatrix} \tag{4.1b}$$

or 2:

$$[Y]_{p2} = \begin{pmatrix} y_{aa} & y_{ab} \\ y_{ba} & y_{bb} \end{pmatrix} = \begin{pmatrix} y_{22} & y_{21} \\ y_{12} & y_{11} \end{pmatrix}. \tag{4.1c}$$

Letter a or b corresponds to the model; a is used always to denote the port from the active resonator is seen from. Number 1 or 2 corresponds to the *physical* port of the circuit, it can be seen from port 1 or from port 2.

Computing the admittance matrix is quite easy either analytical or by simulations. y_{11} and y_{22} are the signal admittance seen by the corresponding port (1 or 2) when

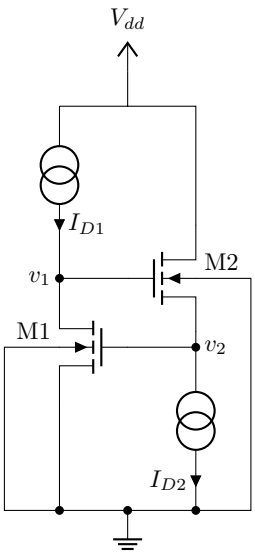

(a) Simple grounded active inductor (SGAI) proposed by Ismail et al. [18].

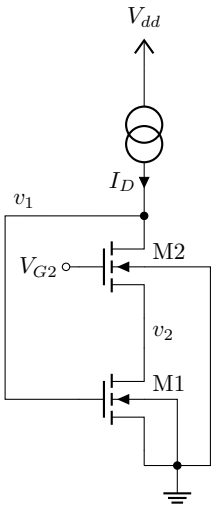

(b) Basic flipped-active inductor (BFAI) proposed by Yue Wu et al. [19].

Figure 4.1: Practical implementations examples of active inductors.

the other is at signal ground. y_{12} and y_{21} are the signal transconductances defined as

$$y_{12} \equiv \left.\frac{i_1}{v_2}\right|_{v_1=0} \quad \text{and} \quad y_{21} \equiv \left.\frac{i_2}{v_1}\right|_{v_2=0} \tag{4.2}$$

respectively.

For the SGAI and BFAI examples, neglecting the parasitic capacitances, their admittance matrix, seen from port 1, are those of the equation 3.1 (which are recalled here):

$$[Y_{\text{SGAI}}] = \begin{pmatrix} y_{11} & y_{12} \\ y_{21} & y_{22} \end{pmatrix} = \begin{pmatrix} g_{ds1} & g_{m1} \\ -g_{m2} & g_{ds2} + n g_{m2} \end{pmatrix} \tag{4.3a}$$

and

$$[Y_{\text{BFAI}}] = \begin{pmatrix} y_{11} & y_{12} \\ y_{21} & y_{22} \end{pmatrix} = \begin{pmatrix} g_{ds2} & -(n g_{m2} + g_{ds2}) \\ g_{m1} - g_{ds2} & g_{ds1} + g_{ds2} + n g_{m2} \end{pmatrix} \tag{4.3b}$$

respectively. And their x values (defined by equation 3.9) are

$$x_{\text{SGAI}} = \frac{g_{m1} g_{m2}}{g_{ds1}(g_{ds2} + n g_{m2})} \tag{4.4a}$$

$$\approx \frac{1}{n} \frac{g_{m1}}{g_{ds1}} \qquad g_{m2} \gg g_{ds2} \tag{4.4b}$$

and

$$x_{\text{BFAI}} = \frac{(g_{m1} - g_{ds2})(n g_{m2} + g_{ds2})}{g_{ds2}(g_{ds1} + g_{ds2} + n g_{m2})} \tag{4.4c}$$

$$\approx n \frac{g_{m1}}{g_{ds1}} \frac{g_{m2}}{g_{ds2}} \qquad I_{D1} \gg I_{D2} \tag{4.4d}$$

respectively (which are independent of the port from which are seen).

At this point, some information of each architecture could be obtained. For example, SGAI has a more simple admittance matrix, so its parameters could be modified easier than for BFAI. If it is searching a low equivalent impedance, the architecture BFAI seen by port 2 could be a better option because its value y_{22} is the greatest of the other y_{nn} of each architecture. The value of x, assuming $g_{m2} \gg g_{ds2}$, for the SGAI is $\approx g_{m1}/g_{ds1}$ (i.e. the intrinsic gain of the transistor M1). For the BFAI is not as simple, but if $I_{D1} \gg I_{D2}$, i.e. $g_{ds1} \gg g_{ds2} + ng_{m2}$, x is $\approx (g_{m1}/g_{ds1})(g_{m2}/g_{ds2})$, the product of the intrinsic gains of each transistor.

Once the inversion level and drain current of each transistor are fixed, the next step is to set the load capacitances at each port (which must take into account the parasitic capacitances calculated or simulated as the imaginary part of the admittance matrix terms y_{11} and y_{22}). Is in this step in which the relation ω_0/ω_b (and ω_0/ω_a) is tuned. For example, for maximum value of Q, the relation ω_0/ω_b needs to be equal to ω_0/ω_a and also to $\sqrt{x}$ (see Section 3.2.4).

In this chapter, it will be shown several simulations with the aim to illustrate the fundamental characteristics of the model developed in Chapter 3. All the simulation points were realized in the following conditions:

1. The current sources are ideal.
2. The inversion level (and hence, the g_m/I_D ratio), back-plane bias `Vbp`, length `L` and drain current `ID` of each transistor are defined by the designer or from some kind of sweep over a region in the design space.
3. From the above parameters, the width `W` (in fact the number of 206 nm wide fingers)[1] and the bias voltages are calculated from the look-up tables (details in Appendix A.2).
4. With the above parameters, the admittance matrix is obtained from two ac simulations using the schematic of Figure 4.2:
   (a) In the first ac simulation, at the desired ω_0 angular frequency, 1 V amplitude signal is set in V_1 while V_2 remains constant (0 V);
   (b) the first two parameters can be extracted:

$$y_{11} = \mathrm{Re}\{i_1\} + j\omega \frac{\mathrm{Im}\{i_1\}}{\omega_0} \tag{4.5a}$$

$$y_{21} = -\mathrm{Re}\{i_2\} - j\omega \frac{\mathrm{Im}\{i_2\}}{\omega_0}; \tag{4.5b}$$

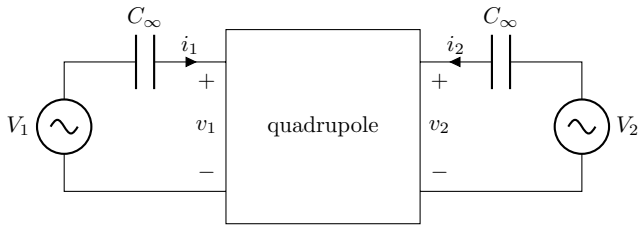

Figure 4.2: Schematic of circuit to extract the two-port network parameters through simulations.

[1] 206 nm is the minimum finger width in the RF design kit for the 28 nm FD-SOI process.

(c) the second ac simulation is performed, at the same desired angular frequency ω_0 with 1 V amplitude signal set in V_2 while V_1 remains constant (0 V);

(d) the last two parameters can be extracted:

$$y_{12} = -\mathrm{Re}\{i_1\} - j\omega\frac{\mathrm{Im}\{i_1\}}{\omega_0} \tag{4.6a}$$

$$y_{22} = \mathrm{Re}\{i_2\} + j\omega\frac{\mathrm{Im}\{i_2\}}{\omega_0}. \tag{4.6b}$$

The proportionality of the imaginary parts with the angular frequency ω implicitly neglects the inductive components of the admittance matrix. This is an hypothesis of the models developed in this work. Imaginary part of y_{12} and y_{21} will not be taken into account except in Section 4.7.

5. External capacitors, C_{ae}—connected between port a and ground—and C_{be}—connected between port b and ground—are calculated from the admittance matrix (using the desired values of ω_0/ω_a and ω_0/ω_b).

6. The final simulation is realized, with ideal current sources and the calculated external capacitors.

4.2 Equivalent resistance and quality factor

Figures 4.3 and 4.4 shows the results of a simulation (Simulation C.1) of SGAI architecture varying the characteristic frequency ω_b trying to reach a constant resonance frequency $f_0 = 2.4\ GHz$ using the equation 3.17. The simulations were carried out from both ports. Figure 4.3 shows the resulting frequency f_0 which is a bit greater than the predicted frequency. Figure 4.4a shows the resulting quality factor, superposed with the model prediction (equation 3.22). Although the results differ in about a 20 % with the model predictions, the behaviour, and, also, the maximum quality factor point ($\omega_0/\omega_b \approx \sqrt{x}$), are as expected. The equivalent impedance at resonance frequency, shown in Figure 4.4b has also the same behaviour as the superposed model (equation 3.18), but also with about 20 % of difference. The normalized PSD of noise,

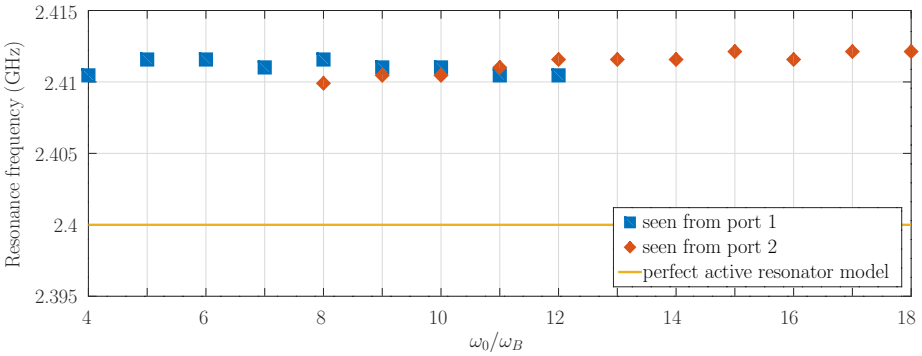

Figure 4.3: Resonance frequency results from the SGAI architecture simulation, searching a resonance frequency of 2.4 GHz. The architecture was seen from both ports, 1 (squared blue marks), and 2 (diamond orange marks). More details in Simulation C.1.

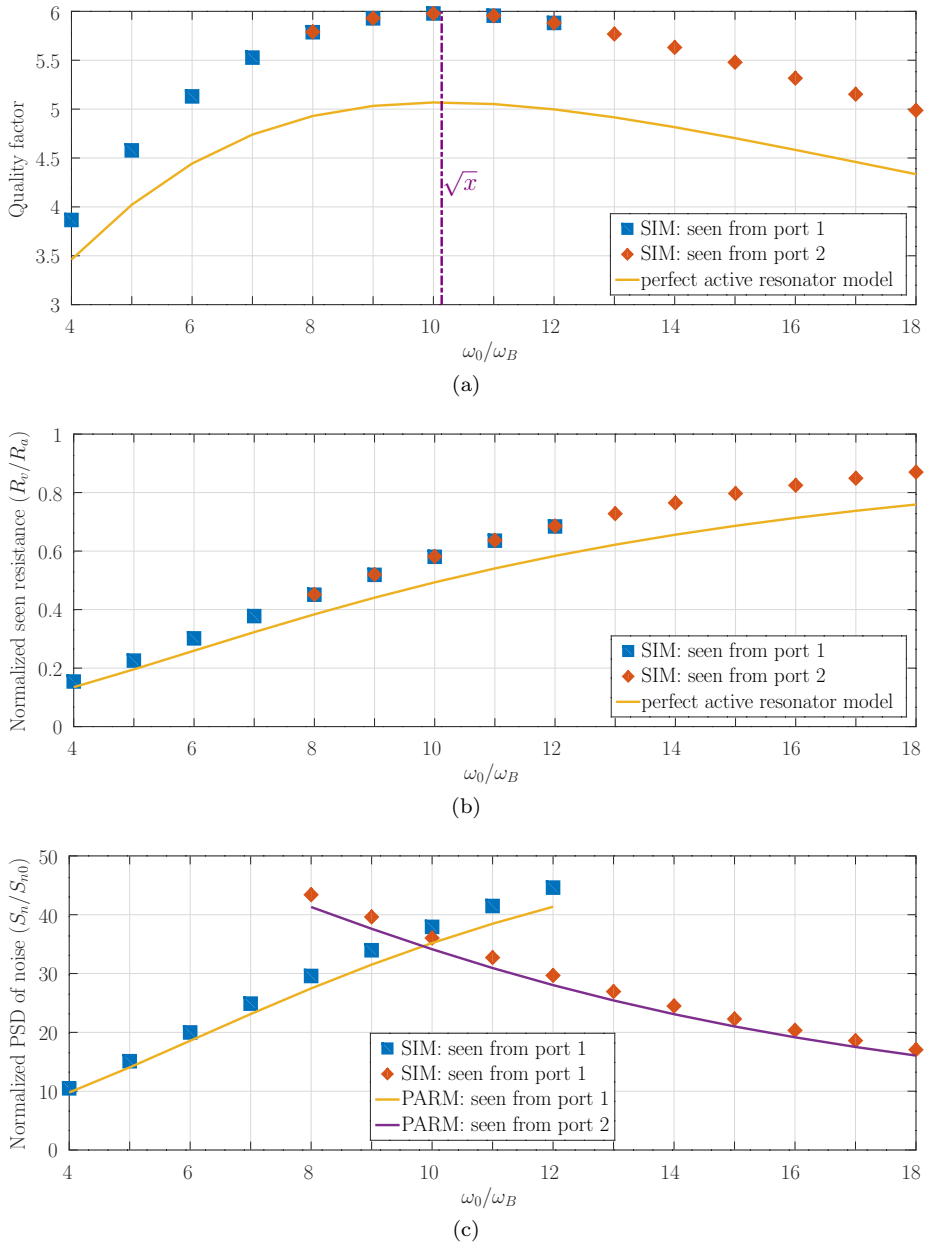

Figure 4.4: Simulation of SGAI architecture seen from both ports, 1 (squared blue marks), and 2 (diamond orange marks), superposed with the Perfect Active Resonator model (continuos yellow line). The searched resonance frequency was $2.4\ GHz$. More details in Simulation C.1.

shown in Figure 4.4c has also a better accuracy with the model[2].

Figures 4.5 and 4.6 show similar results for a simulation (Simulation C.2) using BFAI architecture. The most important difference is the behaviour of noise; the model developed in Section 3.2.5 is not applicable to the BFAI architecture because the value of the transconductances used to calculate the noise is different to the value of the transconductances between ports 1 and 2. For example, for the BFAI architecture seen from port 1, the model assumes a noise current power source of value $I_{na}^2 = 2k_BTg_{ma}$; but in this configuration, the value of g_{ma} is $ng_{m2} + g_{ds2}$ while the *real* noise source at port 1 has a value of $I_{na}^2 = 2k_BTg_{m2}$. In fact, in this architecture, the noise generated by transistor M2 must be modelled with two correlated current sources, one between port 1 and ground, and the other between port 2 and ground. This topology was not taken into account in the noise model developed in Section 3.2.5. There is a noise analysis applied to this architecture in Ou and Ferreira [28].

The differences between model and simulations, in particular with regard to quality factor and equivalent resistance, will be taken up later, in Section 4.7, in which the transcapacitances will be taken into account.

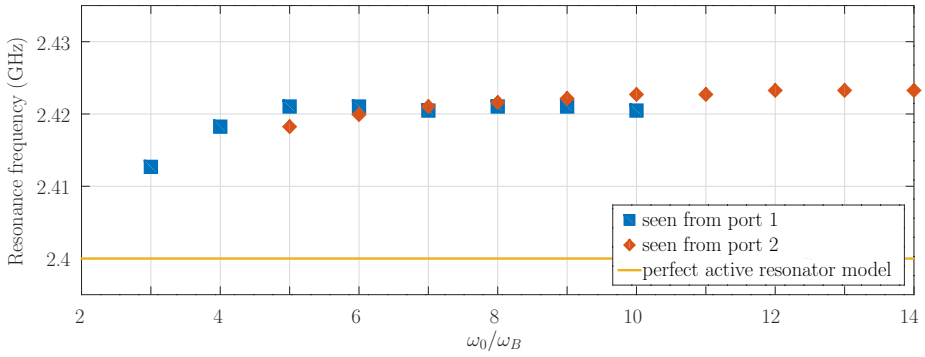

(a)

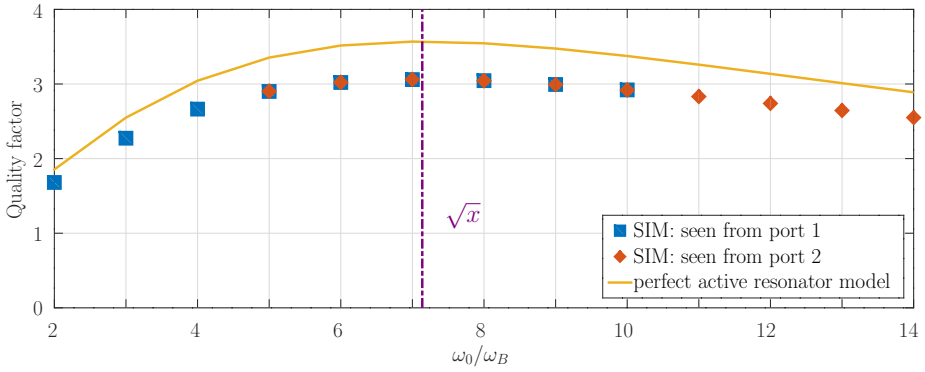

(b)

Figure 4.5: Resonance frequency and quality factor results from the BFAI architecture simulation, seen from both ports, 1 (squared blue marks), and 2 (diamond orange marks), superposed with the Perfect Active Resonator model (continuos yellow line). More details in Simulation C.2.

[2]The model assumes weak inversion level and the simulation was realized with $\text{gmoID}_1 = 16$ and $\text{gmoID}_2 = 15$, which corresponds to a moderate inversion level.

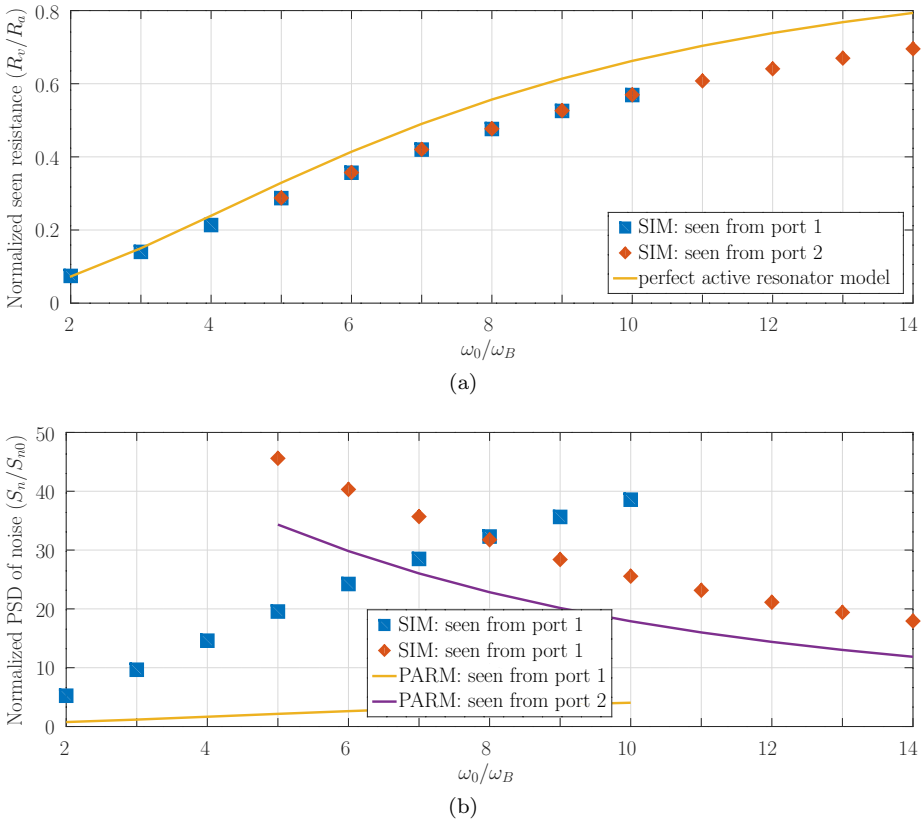

Figure 4.6: Equivalent resistance and normalized noise PSD results from the BFAI architecture simulation, seen from both ports, 1 (squared blue marks), and 2 (diamond orange marks), superposed with the Perfect Active Resonator model (continuos yellow line). The searched resonance frequency was 2.4 GHz. More details in Simulation C.2.

4.3 Tunability

Tuning can be implemented with a coarse and fine adjustment. Coarse tunability could be used to select a band, for example to change between GSM900 and Bluetooth or between the different LTE bands, while fine tunability could be used to choose a channel or to obtain resilience from the manufacturing spread.

The tunability can be implemented by switching the capacitors at each port, or by changing the bias current of the transistors. In this work, fine tunability will be implemented by changing the bias current, while coarse tunability will be implemented by switching the added (externally to the transconductors—but integrated—) capacitors C_{ae} and C_{be}.

4.3.1 Coarse tunability

In this section, coarse tunability switching the capacitors at each port is implemented. Ideal capacitors are considered.

Figure 4.7 shows the impedance module for a coarse tuning of SGAI architecture (Simulation C.4). The tuning was realized for 600 MHz, 1.2 GHz and 2.4 GHz,

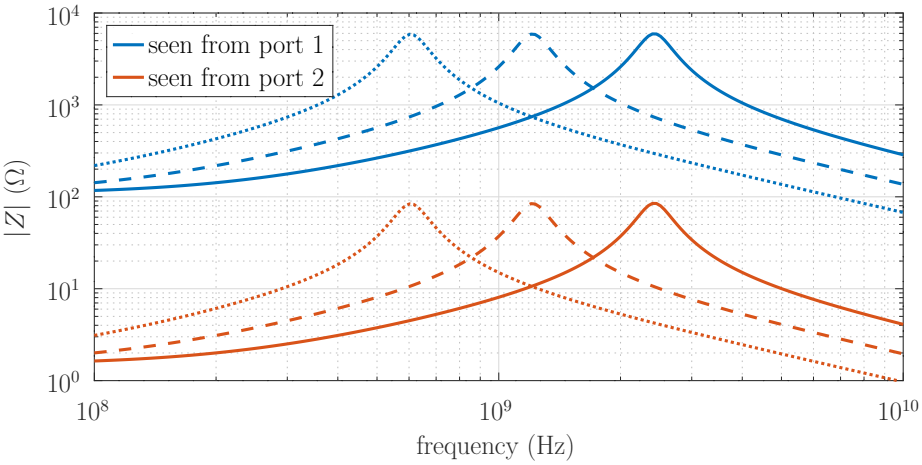

Figure 4.7: Simulations of a coarse frequency tuning using the SGAI architecture, trying to achieve resonance frequencies of 600 MHz, 1.2 GHz and 2.4 GHz. More details in Simulation C.4.

switching the capacitors at each port, and for both, seen from port 1 and seen from port 2. The admittance matrix was obtained from a 2.4 GHz simulation, then the tuning was done by change the external capacitors at port 1 and 2 as specified in Table 4.1. In the same table it is shown the results of resonance frequency, quality factor, equivalent resistance (at resonance frequency) and normalized PSD of noise.

Table 4.1 shows the power of the model; setting the same value of ω_0/ω_b for all the cases (in the example was set $\omega_0/\omega_b = \sqrt{x}$), the resulting quality factor, equivalent resistance and normalized PSD of noise remains constant at each port. Also, the quality factor is independent of the port which is seen from.

This method of coarse tuning of the active resonant circuit is similar to the approach patented by Masuda and Mori [29].

The simulation result for the SGAI architecture was also carried out for BFAI architecture. The results are similar as for SGAI case and are shown in Figure 4.8 and in Table 4.2.

4.3.2 Fine and continuous tunability

In this section, fine and continuous tunability, adjusting the transconductance bias current is presented, although not simulated. The simulations will be realized with

port	C_{ae} (fF)	C_{be} (fF)	f_0 (GHz)	R_v (Ω)	Q	$\frac{S_n}{S_{n0}}$
	203	16640	0.603	5861	5.23	64.1
1	84.4	8295	1.202	5892	5.23	63.6
	25.2	4123	2.399	5924	5.23	63.4
	16481	20.5	0.603	83.8	5.23	20.2
2	8216	85.5	1.202	84.3	5.23	19.9
	4083	25.8	2.399	84.8	5.22	19.9

Table 4.1: Capacitor settings and results of simulation of SGAI architecture with a coarse tuning. C_{ae} and C_{be} are the external capacitors at port a and b respectively. More details in Simulation C.4.

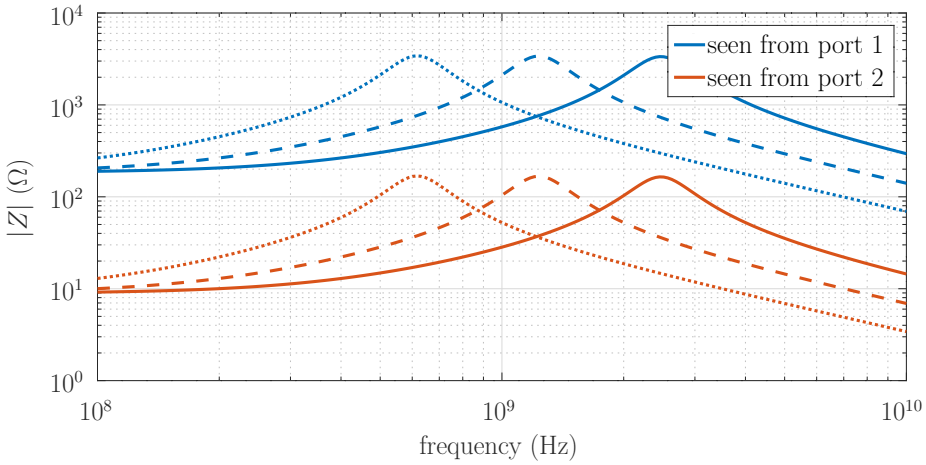

Figure 4.8: Simulations of a coarse frequency tuning using the BFAI architecture, trying to achieve resonance frequencies of 600 MHz, 1.2 GHz and 2.4 GHz. More details in Simulation C.3.

the application example of Chapter 5.

Based on the assumption that

- the transconductance g_m and the output conductance g_o of each transconductor grow as it does its bias current;
- the intrinsic gain g_m/g_o of each transconductor falls as it does its bias current

the behaviour of the angular resonance frequency ω_0, equivalent resistance at resonance frequency R_v and quality factor Q will be analysed.

To remember here, resonance frequency can be calculated as (equation 3.17):

$$\omega_0 \approx x\omega_a\omega_b = \frac{g_{ma}g_{mb}}{C_aC_b} \tag{4.7}$$

equivalent resistance at resonance frequency can be calculated as (equation 3.18)

$$R_v \approx \frac{R_a\frac{\omega_0^2}{\omega_b^3}}{x+\frac{\omega_0^2}{\omega_b^2}} = \frac{1}{\frac{1}{R_a}+\frac{x\omega_b^2}{R_a\omega_0^2}} = \frac{1/C_a}{\frac{g_{oa}}{C_a}+\frac{g_{ob}}{C_b}} \tag{4.8}$$

port	C_{ae} (fF)	C_{be} (fF)	f_0 (GHz)	R_v (Ω)	Q	$\frac{S_n}{S_{n0}}$
1	205	4796	0.617	3422	3.02	21.9
	89.6	2392	1.230	3403	2.99	21.6
	31.9	1190	2.455	3353	2.93	21.2
2	4663	211	0.617	168	3.02	22.6
	2325	92.8	1.230	167	2.99	21.8
	1157	33.6	2.455	165	2.94	21.1

Table 4.2: Capacitor settings and results of simulation of BFAI architecture with a coarse tuning. C_{ae} and C_{be} are the external capacitors at port a and b respectively. More details in Simulation C.3.

and quality factor at resonance frequency can be calculated as (equation 3.21)

$$Q = \frac{\omega_0}{\omega_a + \omega_b} = \frac{1}{\frac{\omega_a}{\omega_0} + \frac{\omega_b}{\omega_0}} = \frac{1}{\sqrt{\frac{C_b}{C_a}\frac{g_{oa}}{g_{ma}/g_{oa}}\frac{1}{g_{mb}}} + \sqrt{\frac{C_a}{C_b}\frac{g_{ob}}{g_{mb}/g_{ob}}\frac{1}{g_{ma}}}}. \tag{4.9}$$

From equation 4.7 it is clear that the resonance frequency grows either with I_{Da} or I_{Db}, bias current of transconductances g_{ma} and g_{mb} respectively.

The equivalent resistance, expanded in equation 4.8 falls as either I_{Da} or I_{Db} grows because the fall of the output conductances g_{oa} or g_{ob} respectively.

The quality factor, expanded in equation 4.9, has a more complicated behaviour because with a growth of bias current of any transconductor, the $g_o/(g_m/g_o)$ grows but the factor $1/g_m$ falls.

Simulation results related with the above analysis will be done in Section 5.2.3.

4.4 Low noise active resonator

In order to demonstrate the conclusions drawn from equation 3.35, i.e. the fact that the noise could be independent of the g_{mb} value, it was simulated an SGAI architecture (Simulation C.5), varying the relation I_{D2}/I_{D1}, i.e. the relation between g_{ma} and g_{mb}.

The results are shown in Figure 4.9. Figure 4.9a shows the normalized PSD of noise at resonance frequency, where, for the case in which the system is seen from port 2, the PSD of noise at resonance frequency, for $I_{D2}/I_{D1} < 10^{-1}$, is smaller than the generated by a passive resonator. The value of Q, shown in Figure 4.9b, is not as expected, because differs significantly from the result $Q \approx \sqrt{x}/2$ (the x value is plotted in figure 4.9c). This phenomenon will be explained in Section 4.7.

As an example, it was simulated an SGAI, seen from port 2, with $I_{D2}/I_{D1} = 0.09$. Figure 4.10a shows the transient response of both, nodes v_1 and v_2. It can be seen the larger swing of v_1 (v_b) than v_2 (v_a), as was analysed in Section 3.3. Figure 4.10c shows the frequency response (left) and the PSD of noise (right), both superposed with the calculated response of a passive RLC resonator with the same resonance frequency, equivalent resistance and quality factor. It can be seen the lower PSD of noise at resonance frequency of the active resonator, which maximum is not exactly at the resonance frequency. Figure 4.10d shows the two main noise contributions in which is clear that the noise performance depends mostly on M3.

4.5 Noise and linearity tradeoffs

Analysing the SGAI architecture, it can be concluded that, on the majority of cases, the linearity is limited by transistor M2. This is because, the gate signal at M1 is $v_{gs1} = v_2$ while the gate signal at M2, neglecting its output conductance -so i_2 and v_1 are in quadrature-, is $v_{gs2} \approx \sqrt{v_1^2 + v_2^2} > v_{gs1}$.

To improve the linearity of SGAI architecture, a resistance R_{s2} can be added at source of M2, as is shown in Figure 4.11.

To analyse the relationship between noise (F) and linearity (IIP3) predicted by Figure 3.13, the SGAI architecture was simulated (Simulation C.7) varying the value of R_{s2} and the relationship I_{D2}/I_{D1}, setting for every point the same total current ($I_{D1} + I_{D2} = 1\ mA$), resonance frequency ($f_0 = 2.4\ GHz$) and inversion level of each transistor ($\text{gmoID}_1 = \text{gmoID}_2 = 10\ V^{-1}$). The result is shown in Figure 4.12 with a thermal colour representing the quality factor values. More detail results are shown in Figure C.1 of the appendix C, and in Simulation C.7.

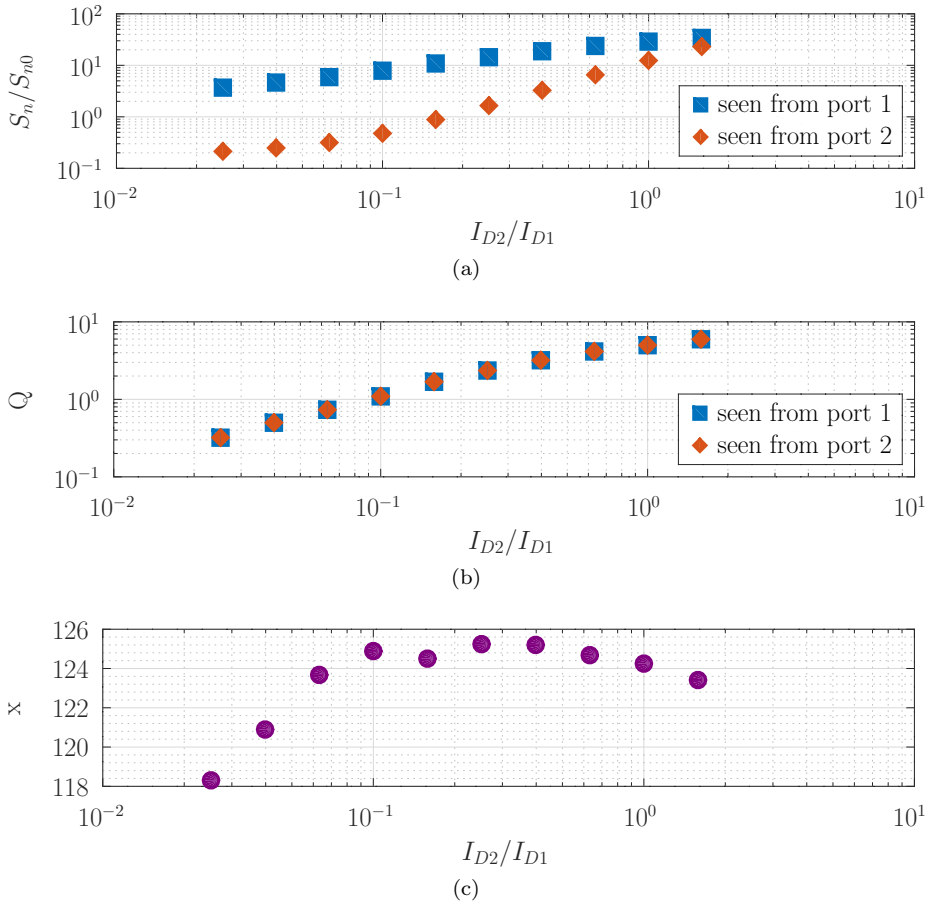

Figure 4.9: Simulation results of SGAI architecture varying the relation I_{D2}/I_{D1} searching for a low noise operating point.

In order to design a low noise amplifier (LNA), the use of the SGAI architecture seen from port 2 can be a good choice if it will be used at the input, while the same applies for that architecture seen from port 1 if it will be used at the output of the LNA. This will be discussed later.

It is important to note that the quality factor values achieved by the architecture seen from one port are quite the same as those achieved by the architecture seen from the other port. The most significant difference are the noise and linearity performance, so, as was previously inferred by Shin and Bult [13], there is no general relationship between noise and quality factor.

Previous works, like Abidi [21], postulates that power spectral density of noise is proportional to the quality factor Q. Those analyses are based on the assumption that the transconductances and the capacitances are fixed, so a change on the quality factor must be done by a change in the parasitic resistances (transconductances output conductance). In the present work, the developed model, shows the real constraints between noise, linearity, quality factor and power consumption, as was presented in Section 3.3.

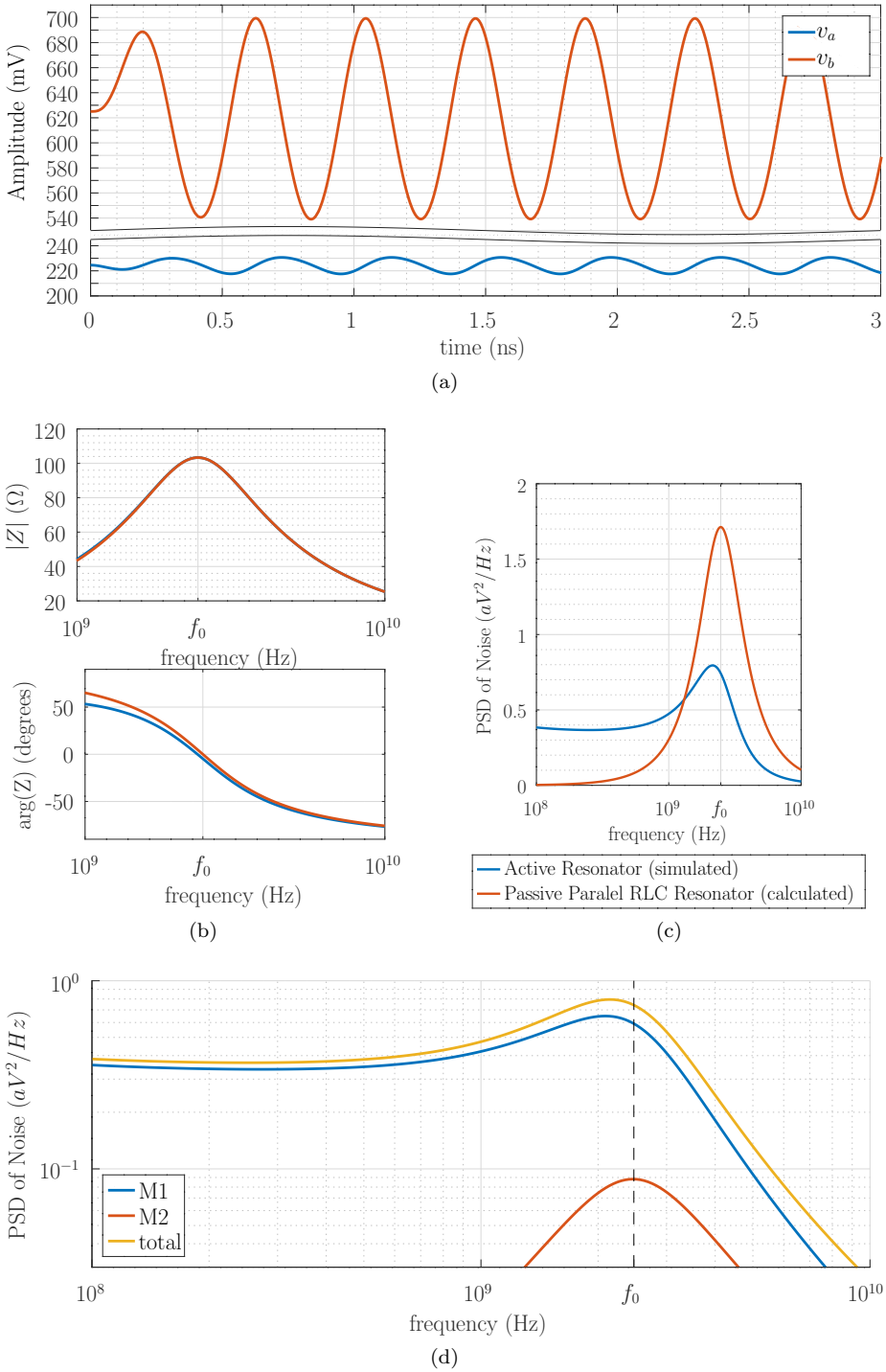

Figure 4.10: Simulation results of SGAI architecture in an operating point in which the PSD of noise at resonance frequency is less than the generated by the passive counterpart. More details in Simulation C.6.

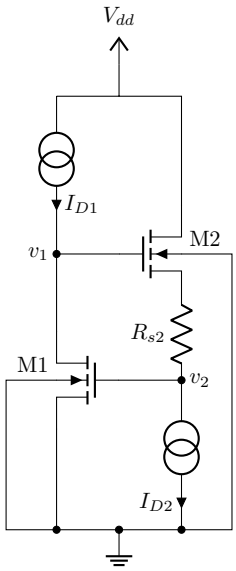

Figure 4.11: Schematic of the SGAI architecture with a series resistance added to the source of transistor M2 with the aim to improve the linearity performance.

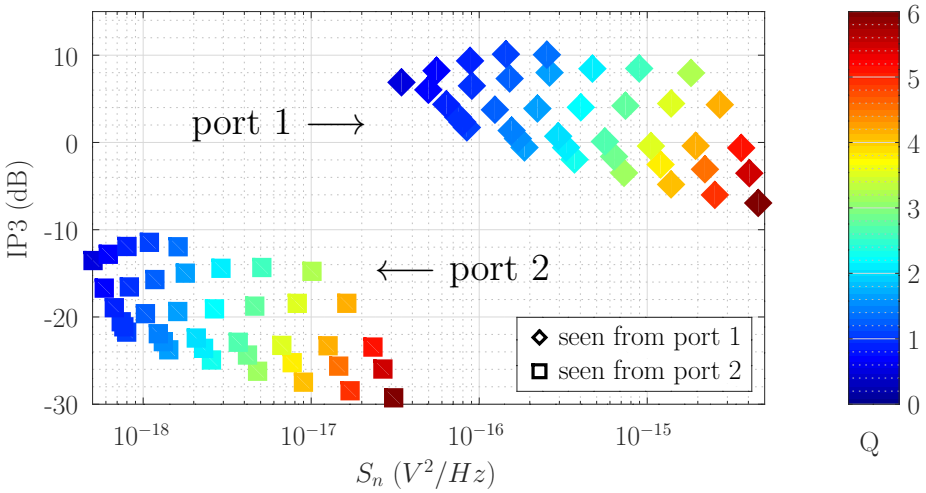

Figure 4.12: Simulation results of the SGAI architecture, varying the value of R_{s2} and the relationship I_{D2}/I_{D1}, with a total current of $1\ mA$, resonance frequency of about $2.4\ GHz$ and $(g_m/I_D) = 10\ V^{-1}$ for both transistors. More details in Simulation C.7.

4.6 Noise and power consumption tradeoff

Figure 4.13 shows the simulation (Simulation C.8) of the SGAI architecture varying the total current consumption. As is predicted by the model, the quality factor (Figure 4.13b) and the normalized power spectral density of noise (Figure 4.13c) at resonance frequency are quite constant. It is also constant the linearity (Figure 4.13d). The relevant change is the equivalent resistance at resonance frequency (Figure 4.13a) and, therefore, the noise power.

The tradeoff between noise and power consumption is, in fact, a tradeoff between power consumption and equivalent parallel resistance of the resonant circuit (i.e. the equivalent resistance at resonance frequency). Going back to the simple LNA model shown in Figure 4.14 (previously presented in Figure 3.12), if the resistor R_{out} is replaced by an active resonator circuit, the tradeoff between noise and power consumption has two aspects:

- The normalized PSD of noise (S_n/S_{n0}) is given by the architecture and the operating point, so more current implies less resistance and also less thermal noise voltage at the output.
- If the transconductor g_m is made with a single transistor, it is a well-known result reference that the noise performance will be better if the value of R_{out} is lower and the value of g_m is greater, i.e. more current consumption from the active resonator circuit and also from the transconductor g_m.

This second fact discourages the use of the SGAI architecture seen from port 1 at the output of an LNA. It was already clear, from Figure 4.12, the larger noise generated by the SGAI architecture seen from port 1. This configuration, used at the output of an LNA, will also need a very large current to reduce its equivalent resistance; otherwise the transconductor, with a low g_m value to achieve the desired gain, will generate a very large noise value. Otherwise, if the SGAI current is low—obtaining a large impedance—and the g_m value is high—generating small noise—the LNA gain will be very large which implies a linearity problem.

With the aim to illustrate this aspect, a theoretical analysis was realized using the schematics idealized in Figure 4.15 showing the core of the LNA (without taking into account the input impedance) loaded with an SGAI architecture seen from both, port 1 (Figure 4.15a) and port 2 (Figure 4.15b). In both cases the transistor M3 implements the transconductance g_m of the schematic of Figure 4.14. Figure 4.16 shows the theoretical result of the relationship between power consumption and noise figure. Figure 4.16a shows the case of seen from port 1 and considering only the noise generated by the transistors M1 and M3, while Figure 4.16b shows the case of seen from port 2 and considering only the noise generated by the transistors M2 and M3. To generate the plots of Figure 4.16, the length and the g_m/I_D ratio are fixed for each transistor, and the sweep was done over the I_{D3} current; for each value of I_{D3}:

1. obtain the g_{m3} value as:
$$g_{m3} = \left(\frac{g_m}{I_D}\right)_{M3} I_{D3}$$
2. obtain the needed impedance of the SGAI architecture to achieve the desired gain value:
$$R_v = \frac{G_v}{g_{m3}}$$
3. obtain the current needed by M1 (seen from port 1) or M2 (seen from port 2) to achieve $R_v = R_a/2$ (assuming the maximum quality factor operating point).

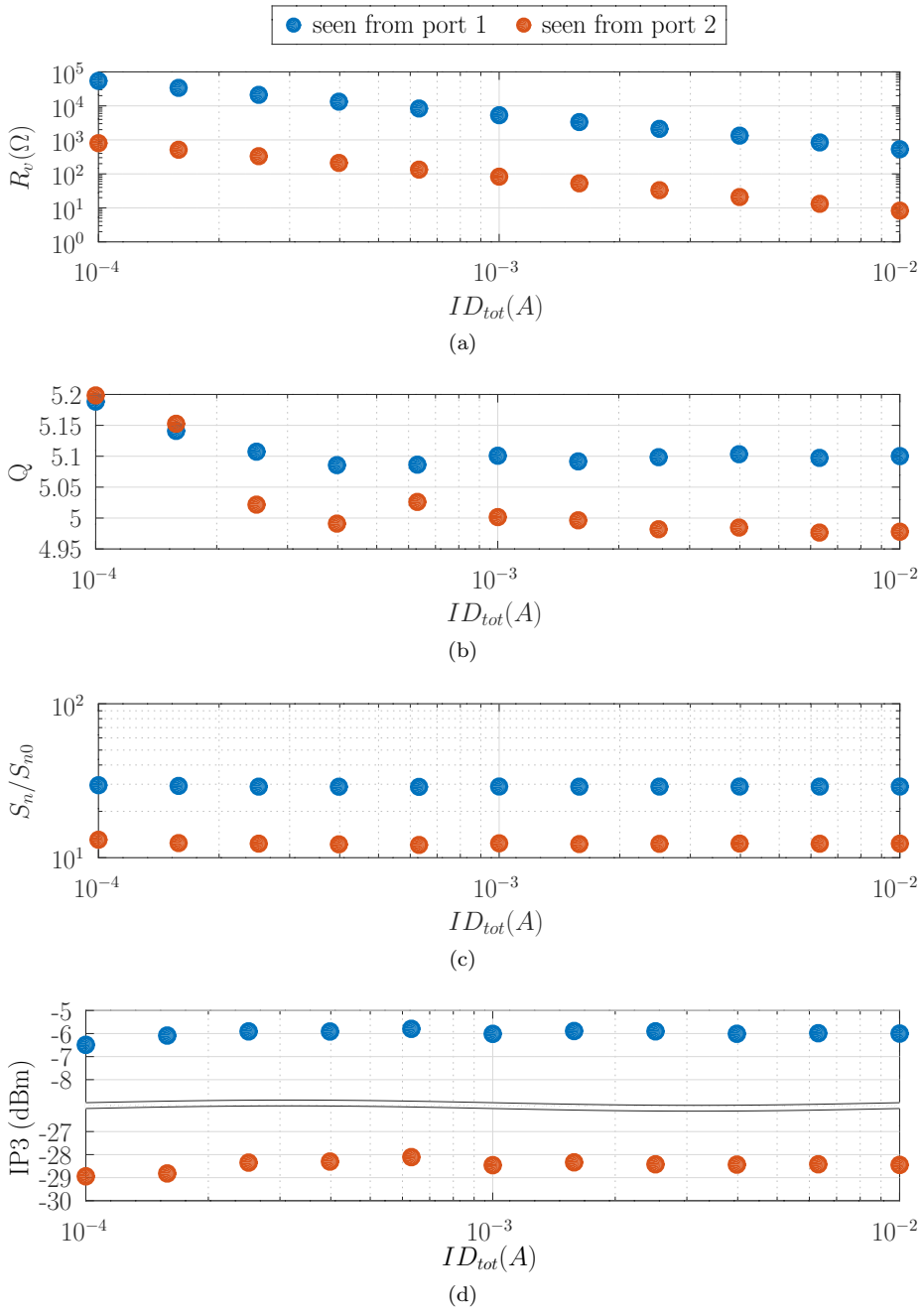

Figure 4.13: Simulation results of the SGAI architecture varying the total current consumption. More details in Simulation C.8.

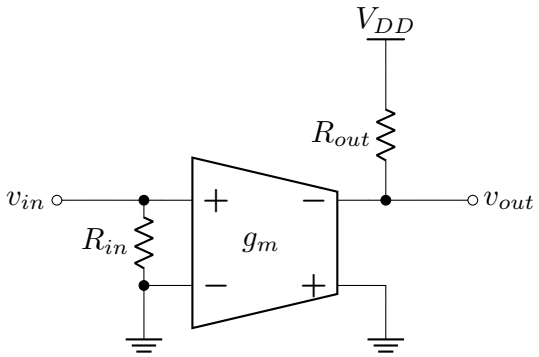

Figure 4.14: Simple LNA model used to analyse the tradeoffs.

4. calculate the noise generated by M1 and M3 (seen from port 1) or M2 and M3 (seen from port 2), and its corresponding noise figure as

$$NF = 10\log_{10}(F) \quad , \quad F = \frac{S_{no}}{GS_{ni}} \tag{4.10}$$

where G is the signal power gain, S_{no} is the PSD of output noise (considering contributions of the LNA transistor, the active inductor and the input noise), and S_{ni} is the PSD of input noise (considering 50 Ω input matching).

From the above sweep is clear that the considered results do not depend on the design of M2 (when seen from port 1) or the design of M1 (when seen from port 2). In both figures (Figures 4.16a and 4.16b) the case of the LNA loaded by a passive resistor is added in violet for reference.

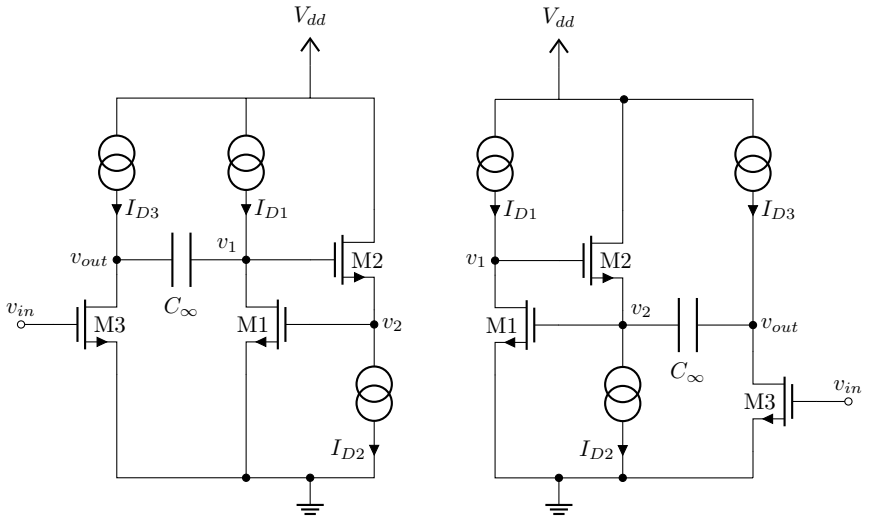

(a) LNA loaded with SGAI seen from port 1. (b) LNA loaded with SGAI seen from port 2.

Figure 4.15: Schematics of the LNA core (without taking into account the input impedance) loaded with an SGAI architecture seen from both, port 1 (a), and port 2 (b).

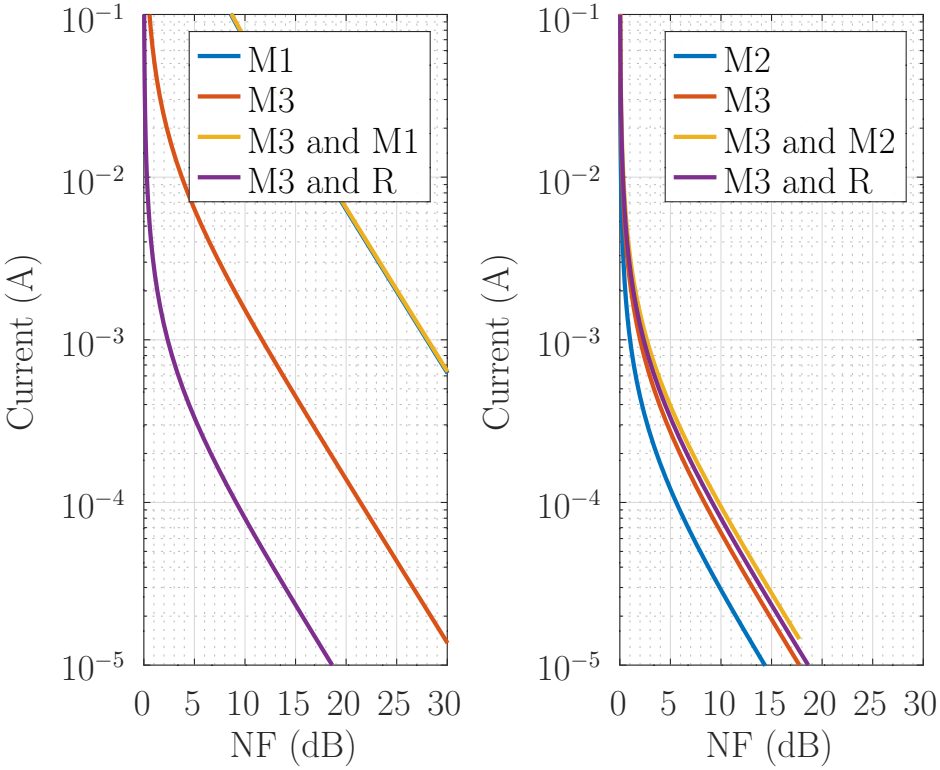

(a) SGAI seen from port 1.

(b) SGAI seen from port 2.

Figure 4.16: Theoretical results of the relationship between power consumption and noise figure for the *simple grounded active inductor* (SGAI) architecture. The curves labelled with "M1" and "M3" in figure (a)—"M2" and "M3" in figure (b)—corresponds to the case in which the LNA is loaded with an active resonator as shows Figure 4.15. The curve "M3 and R" does not have *less noise* than the case of only "M3", but has less current consumption.

4.6.1 Low impedance SGAI

To reduce the equivalent resistance, adding a parallel resistor R_1 on port a (as shown in Figure 4.17a) is not a good solution because it accomplishes a reduction of the quality factor, by the reduction of the value of x:

$$x_1 = x_s \frac{R_{as}||R_1}{R_{as}} \tag{4.11}$$

where x_1 is the new value of x when the resistance R_1 is added, and the subindex s refers to the original parameters of the SGAI architecture seen from port 1.

A more interesting approach, in the case of the SGAI architecture seen from port 1, is to use the current through this resistor, to increase the transconductance g_{mb} (i.e. the generated by M2), as shown in Figure 4.17b (where R_1 was changed by R_2). In this case the new value of x is

$$x_2 = x_s \frac{R_{as}||R_2}{R_{as}} \frac{g_{mbs} + \frac{1}{R_2}}{g_{mbs}} \frac{R_{bs}||R_2}{R_{bs}}. \tag{4.12}$$

Now, the value of g_{mb} is increased but the value of R_b is reduced.

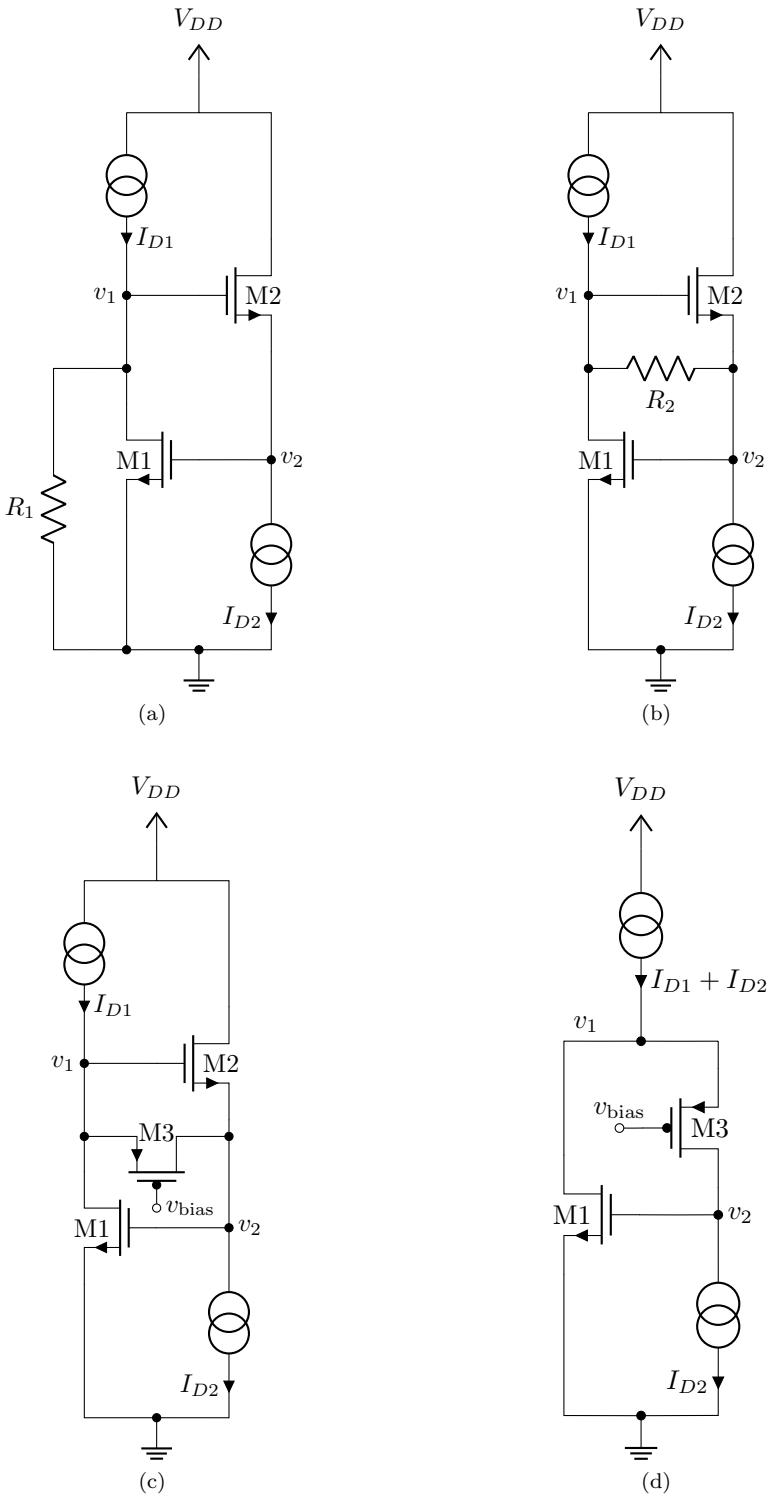

Figure 4.17: Step-to-step deduction of the LI-SGAI architecture.

To avoid this problem, the resistor can be replaced by a PMOS transistor, as shown in Figure 4.17c. With this new approach the resistance R_a is reduced more than the reduction of resistance R_b (because, generally, $g_m > g_{ds}$):

$$x_3 = x_s \frac{R_{as} || \frac{1}{g_{m3}+g_{ds3}}}{R_{as}} \frac{g_{mbs}+g_{m3}+g_d 3}{g_{mbs}} \frac{R_{bs} || \frac{1}{g_{ds3}}}{R_{bs}} \tag{4.13a}$$

$$\approx x_s \frac{R_{as} || \frac{1}{g_{m3}}}{R_{as}} \frac{g_{mbs}+g_{m3}}{g_{mbs}} \frac{R_{bs} || \frac{1}{g_{ds3}}}{R_{bs}} \tag{4.13b}$$

where the relationship $g_{m3} \gg g_{ds3}$ was taken into account.

One more step can be done to simplify the circuit if it is taken into account that the intrinsic gain of M2 as common-drain follower is near 1; then the circuit can be reduced to only two transistors as shown in Figure 4.17d. This new architecture will be denoted as *low impedance simple grounded active inductor*[3] (LI-SGAI) and its x value is

$$x_{\text{li-sgai}} = \frac{g_{m1}(g_{mb3}+gds3)}{g_{ds3}(g_{ds1}+g_{mb3}+g_{ds3})} \tag{4.14a}$$

$$\approx \frac{g_{m1} g_{mb3}}{g_{ds3}(g_{ds1}+g_{mb3})} \qquad g_{m3} \gg g_{ds3} \tag{4.14b}$$

$$\approx \frac{g_{m1}}{g_{ds1}} \frac{g_{mb3}}{g_{ds3}} \qquad \text{if } I_{D1} \ll I_{D3} \tag{4.14c}$$

where, again, the relationship $g_{m3} \gg g_{ds3}$ was taken into account. The x value of this new architecture is larger in the case of $I_{D1} \ll I_{D3}$ (equation 4.14c). In this case it is greater than that of the SGAI architecture (given by equation 4.4a and recalled here):

$$x_{\text{SGAI}} \approx \frac{g_{m1}}{g_{ds1}}. \tag{4.15}$$

A group of simulations (Simulation C.9) of the LI-SGAI architecture is shown in figure 4.18.

4.7 The complete active resonator model

As was shown in Section 4.2, although the transistor level results match qualitatively with the perfect active resonator model, they differ quantitatively. The main reason for that is that the model developed in Chapter 3 does not take into account the transcapacitances between ports a and b.

This section develops a more complete model which incorporates the capacitive terms between ports a and b. As was done before, some mathematical results, which equations are tagged with square brackets, are developed in the Appendix B.

To incorporate the transcapacitances to the model, if these are defined as

$$C_{ab} = -\left.\frac{i_a}{\frac{\partial v_b}{\partial t}}\right|_{v_a=0} \quad \text{and} \quad C_{ba} = -\left.\frac{i_b}{\frac{\partial v_a}{\partial t}}\right|_{v_b=0} \tag{4.16}$$

then, the two-port network matrix of equation 3.40, in steady state, needs to be rewritten as follows:

$$[Y] = \begin{bmatrix} y_{aa} & y_{ab} \\ y_{ba} & y_{bb} \end{bmatrix} = \begin{bmatrix} \frac{1}{R_a}\left(1+j\frac{\omega}{\omega_a}\right) & g_{ma}\left(1+j\frac{\omega}{\omega_{ab}}\right) \\ -g_{mb}\left(1+j\frac{\omega}{\omega_{ba}}\right) & \frac{1}{R_b}\left(1+j\frac{\omega}{\omega_b}\right) \end{bmatrix} \tag{4.17}$$

[3]The adjective *low impedance* is not entirely appropriate because the final situation is similar to the SGAI, from one port the impedance is considerably smaller than the other, but the name responds to the motivation of this new architecture.

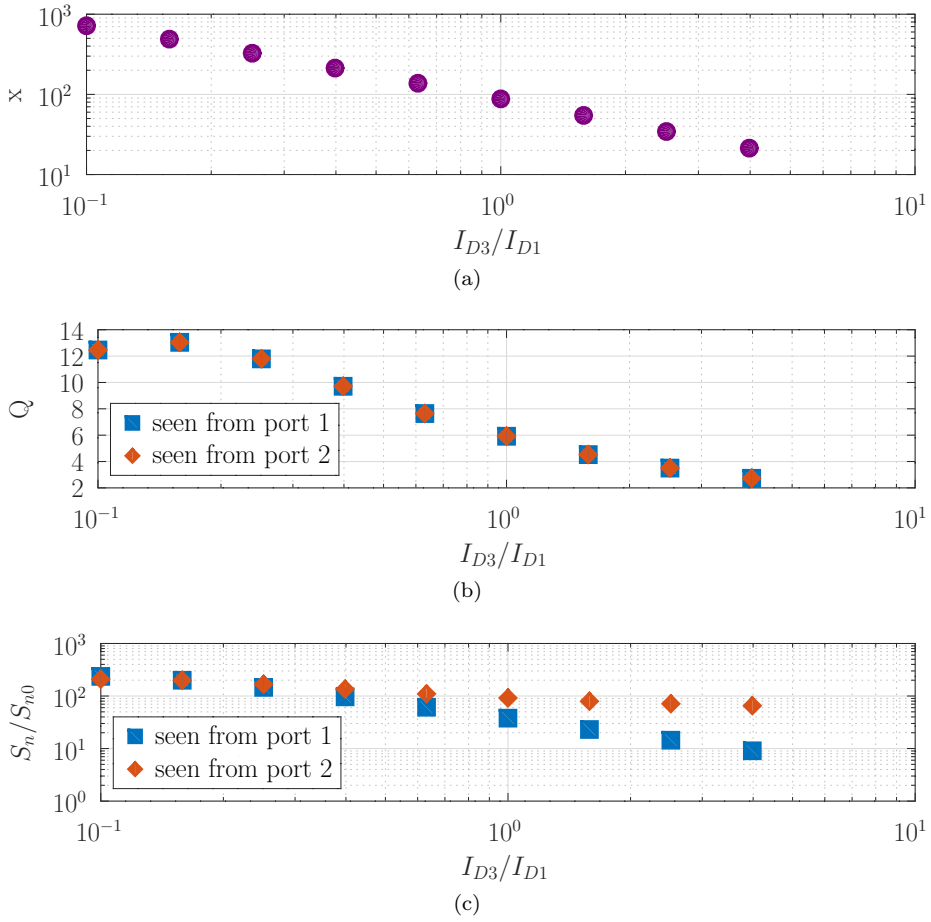

Figure 4.18: Simulations of a new proposed architecture: *low impedance simple grounded active inductor* (LI-SGAI). As was deduced from the equations 4.14, the value of x (and also for Q) is larger when $I_{D3} \ll I_{D1}$. More detailed results are in Simulation C.9.

where $\omega_{ab} = \frac{g_{ma}}{C_{ab}}$ and $\omega_{ba} = \frac{g_{mb}}{C_{ba}}$. The above matrix can still be obtained from simulations, with the same method explained in Section 4.1.

The Thevenin equivalent admittance from port a can be calculated as

$$\frac{1}{Z_v(j\omega)} = Y_v(j\omega) = \frac{i_a}{v_a} = y_{aa} - \frac{y_{ab}y_{ba}}{y_{bb}} = G + jB \tag{4.18}$$

where G and B are the conductance and susceptance given by the following expressions

$$\begin{cases} G = \dfrac{1}{R_a}\left[1 + \dfrac{x}{1+\frac{\omega^2}{\omega_b^2}}\left(1 + \dfrac{\omega^2}{\omega_{ab}\omega ba} + \dfrac{\omega^2}{\omega_b\omega_{ba}} - \dfrac{\omega^2}{\omega_b\omega_{ab}}\right)\right] \\ B = \dfrac{1}{R_a}\left[\dfrac{\omega}{\omega_a} - \dfrac{x}{1+\frac{\omega^2}{\omega_b^2}}\left(\dfrac{\omega}{\omega_b} + \dfrac{\omega}{\omega_{ab}} - \dfrac{\omega}{\omega_{ba}} + \dfrac{\omega^3}{\omega_b\omega_{ab}\omega_{ba}}\right)\right] \end{cases} \tag{4.19}$$

where

$$x = R_a g_{ma} R_b g_{mb} \tag{4.20a}$$
$$\omega_a = \frac{1}{R_a C_a} \tag{4.20b}$$
$$\omega_b = \frac{1}{R_b C_b} \tag{4.20c}$$
$$\omega_{ab} = \frac{g_{ma}}{C_{ab}} \tag{4.20d}$$
$$\omega_{ba} = \frac{g_{mb}}{C_{ba}} \tag{4.20e}$$
$$\tag{4.20f}$$

were already defined.

To work with the equation 4.19, the following modifications will be made: the first is the approximation $1 + \frac{\omega^2}{\omega_b^2} \approx \frac{\omega^2}{\omega_b^2}$, i.e. analyse the system in a region of $\omega \gg \omega_b$. The second is to define two new parameters in place of ω_{ab} and ω_{ba}, as follows

$$\frac{1}{\omega_\Delta} \equiv \frac{1}{\omega_{ab}} - \frac{1}{\omega_{ba}} = \frac{C_{ab}}{g_{ma}} - \frac{C_{ba}}{g_{mb}} \tag{4.21a}$$
$$\frac{1}{\omega_\Pi^2} \equiv \frac{1}{\omega_{ab}\omega_{ba}} = \frac{C_{ab}C_{ba}}{g_{ma}g_{mb}}. \tag{4.21b}$$

With the above modifications, equation 4.19 becomes

$$G = \frac{1}{R_a}\left[1 + \frac{x}{\omega^2/\omega_b^2}\left(1 + \frac{\omega^2}{\omega_\Pi^2} - \frac{\omega^2}{\omega_b\omega_\Delta}\right)\right] \tag{4.22a}$$
$$B = \frac{1}{R_a}\left[\frac{\omega}{\omega_a} - \frac{x}{\omega^2/\omega_b^2}\left(\frac{\omega}{\omega_b} + \frac{\omega}{\omega_\Delta} + \frac{\omega^3}{\omega_b\omega_\Pi^2}\right)\right]. \tag{4.22b}$$

Generally, ω_Π can be neglected because ω_{ab} and ω_{ba} will be much greater than the range of interesting frequencies, around ω_0.

The resonance frequency ω_0 can be calculated by cancelling the susceptance B of equation 4.22b:

$$B(\omega_0) = 0 \iff \frac{1}{R_a}\left[\frac{\omega_0}{\omega_a} - \frac{x}{\omega_0^2/\omega_b^2}\left(\frac{\omega_0}{\omega_b} + \frac{\omega_0}{\omega_\Delta} + \frac{\omega_0^3}{\omega_b\omega_\Pi^2}\right)\right] = 0 \tag{4.23a}$$
$$\iff \frac{\omega_0}{\omega_a} = \frac{x}{\omega_0^2/\omega_b^2}\left(\frac{\omega_0}{\omega_b} + \frac{\omega_0}{\omega_\Delta} + \frac{\omega_0^3}{\omega_b\omega_\Pi^2}\right) \tag{4.23b}$$
$$\iff \omega_0^2 = \frac{x\omega_a\omega_b}{1 - x\frac{\omega_a\omega_b}{\omega_\Pi^2}}\left(1 + \frac{\omega_b}{\omega_\Delta}\right). \tag{4.23c}$$

To simplify the expressions, can be defined ω_x as

$$\omega_x^2 = \frac{x\omega_b^2}{1 - x\left(\frac{\omega_b}{\omega_\Delta} - \frac{\omega_b^2}{\omega_\Pi^2}\right)} \tag{4.24}$$

which—as will be shown later—plays the role of $\omega_b\sqrt{x}$ in the *perfect active resonator model* developed in Chapter 3.

With the above definition, the equivalent resistance is

$$R_v = \frac{1}{G(\omega_0)} = \frac{R_a}{x}\frac{\omega_0^2/\omega_b^2}{1 + \frac{\omega_0^2}{\omega_x^2}}. \tag{4.25}$$

The quality factor Q can be calculated as

$$Q = \frac{R_p}{\omega L_p} \tag{4.26a}$$

$$= R_p \omega C_p \tag{4.26b}$$

where R_p is the equivalent parallel resistance $(1/G)$, L_p is the equivalent parallel inductance and C_p is the parallel capacitance. Since the resonance frequency (ω_0) was obtained after the approximation $1 + \frac{\omega}{\omega_b} \approx \frac{\omega}{\omega_b}$, both expressions of 4.26 will conduct to identical results.

From equation 4.22b,

$$\frac{1}{L_p} \equiv \frac{x\omega_b}{R_a}\left(1 + \frac{\omega_b}{\omega_\Delta}\right) \tag{4.27a}$$

$$C_p \equiv \frac{1}{R_a}\left(\frac{1}{\omega_a} - \frac{x\omega_b}{\omega_\Pi^2}\right) \tag{4.27b}$$

then

$$Q(\omega_0) = \frac{\frac{\omega_0}{\omega_b} + \frac{\omega_0}{\omega_\Delta}}{1 + \frac{\omega_0^2}{\omega_x^2}} \tag{4.28}$$

with a relative maximum in $\omega_0 = \omega_x$ of value

$$Q(\omega_0 = \omega_x) = \frac{1}{2}\left(\frac{\omega_0}{\omega_b} + \frac{\omega_0}{\omega_\Delta}\right). \tag{4.29}$$

This relative maximum of Q makes sense only when $\omega_x^2 > 0$.

On the other hand, for any ω_0, if $\omega_x^2 = -\omega_0^2$, the quality factor (equation 4.28) tends to infinity (also the equivalent resistance by the equation 4.25). And this can be possible; analysing the expression 4.24, it can be see that ω_x^2 can be either positive or negative. For example, if

$$\frac{1}{\omega_{ba}} \sim 0 \tag{4.30a}$$

and

$$\frac{1}{\omega_{ab}} \approx \frac{1}{10\omega_b} \Rightarrow \frac{\omega_b}{\omega_{ab}} \approx \frac{1}{10} \tag{4.30b}$$

then,

$$\frac{1}{\omega_\Pi} \sim 0 \quad \text{and} \quad \frac{1}{\omega_\Delta} \approx \frac{1}{\omega_{ab}} \approx \frac{1}{10\omega_b} \tag{4.30c}$$

and results in

$$\omega_x^2 \approx \frac{x\omega_b^2}{1 - x\frac{\omega_b}{\omega_{ab}}} \approx \frac{x\omega_b^2}{1 - \frac{x}{10}} \tag{4.30d}$$

if, for example, $x = 100$, then

$$\omega_x^2 \approx -10\omega_b^2. \tag{4.31}$$

So, the case in which $\omega_x^2 < 0$, can be possible with an appropriate value of transcapacitances, which implementation is not analysed in this work. This fact was mentioned in Belmas [8] with a different model and approach than the realized here.

Figure 4.19 shows the two cases for the sign of ω_x^2. Figure 4.19a shows a similar behaviour of Figure 3.6 for the *perfect active resonator model* developed in Chapter 3. Figure 4.19b shows the case in which ω_x^2 is negative, where the value of Q tends to infinity when $\omega_0^2 = -\omega_x^2$.

ω_x is the value at which the quality factor is maximum, and also the value at which the equivalent resistance is $R_a/2$; plays the role of $\omega_b\sqrt{x}$ in the *perfect active resonator*

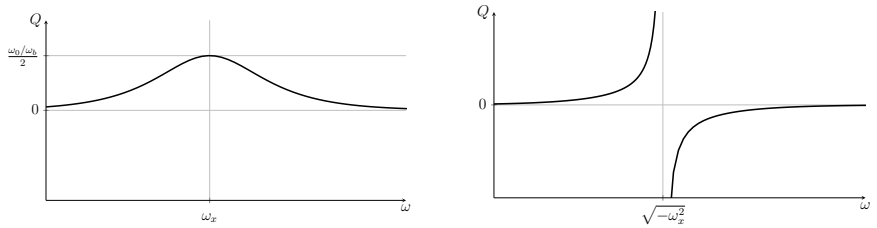

(a) $\omega_x^2 > 0$. (b) $\omega_x^2 < 0$.

Figure 4.19: Plots of the quality factor as a function of the resonance frequency.

model developed in Chapter 3.

The noise can be analysed from the output current noise power of each transconductor as was done in Section 3.2.6. With

$$I_{na}^2 = 2nk_BTg_{ma} \quad \text{and} \quad I_{nb}^2 = 2nk_BTg_{mb} \tag{4.32}$$

I_n^2 results in

$$I_n^2 = I_{na}^2 + \left|\frac{y_{ab}}{y_{bb}}\right|^2 I_{nb}^2 \tag{4.33a}$$

$$= 2nk_BT\left[g_{ma} + \frac{g_{ma}^2 R_b^2}{1+\frac{\omega^2}{\omega_b^2}}\left(1+\frac{\omega^2}{\omega_{ab}^2}\right)g_{mb}\right] \tag{4.33b}$$

$$\approx 2nk_BT\left[g_{ma} + \frac{g_{ma}^2 R_b^2}{\omega^2/\omega_b^2}\left(1+\frac{\omega^2}{\omega_{ab}^2}\right)g_{mb}\right]. \tag{4.33c}$$

The normalized power spectral density of noise becomes

$$\frac{S_n}{S_{n0}} = \frac{n}{2}\frac{R_v}{R_a}g_{ma}\left[R_a + \frac{x}{\omega^2/\omega_b^2}\left(1+\frac{\omega^2}{\omega_{ab}^2}\right)R_b\right]. \tag{4.34}$$

Figure 4.20 shows the results of the same simulations as in Section 4.2 but using three different models to achieve the desired resonance frequency:

1. Perfect active resonator model (PARM), developed in Chapter 3.
2. Complete active resonator model (CARM), developed in this chapter, but neglecting the parameter ω_Π (i.e. $\omega_\Pi \to \infty$).
3. Complete active resonator model (CARM), with all the parameters taken into account.

From these results is not clear that the new *complete active resonator model* (CARM) gives better approach; the resonance frequency for the SGAI architecture is closer to the desired 2.4 GHz if the CARM is used, while for the BFAI architecture, the result is opposite. However, the following results prove the improvement of the CAR model in front of the PAR model.

Figures 4.21 and 4.22 shows the simulation results from Section 4.2 but with the superposition of this new model (with and without neglecting the term ω_Π—i.e. considering ω_Π tends to infinity—). These results prove the CAR model accuracy at the cost of takes into account the transcapacitances between ports a and b.

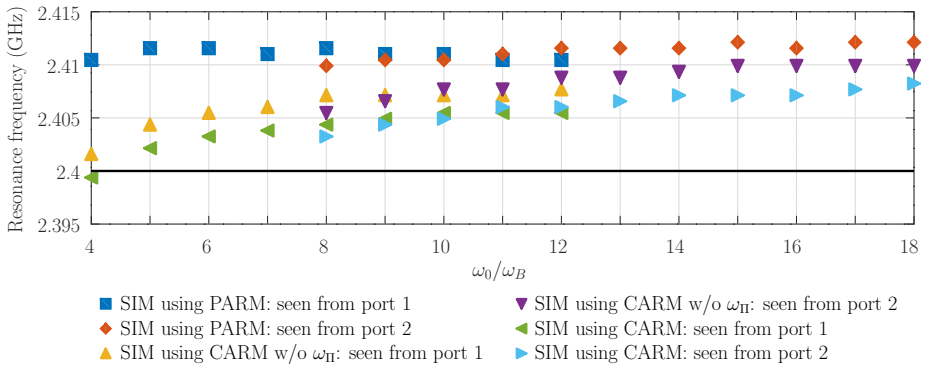

(a) Simple grounded active inductor architecture.

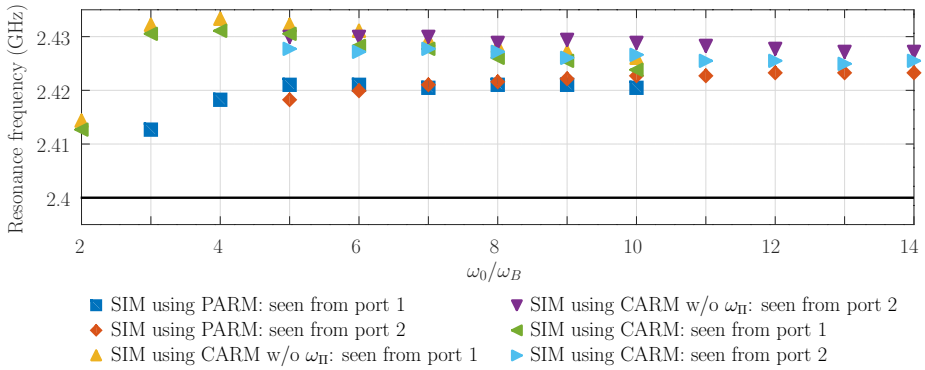

(b) Basic flipped active inductor architecture.

Figure 4.20: Resonance frequency results obtained from simulations trying to reach 2.4 GHz of resonance frequency (marked with continuous black line), using the *perfect active resonator model* (PARM) developed in Chapter 3, and the *complete active resonator model* (CARM) developed in Section 4.7 (with and without the term ω_Π—i.e. considering $\omega_P i$ tends to infinity—).

The differences in the normalized PSD of noise in Figure 4.22c responds to the assumptions in which the model is based; analysing the BFAI architecture, is clear that the noise power sources corresponding to transistors M1 and M2, can not be modelled as was shown in Figure 3.11. The noise introduced by transistor M2 needs to be modelled by a noise current source between ports 1 and 2, or, if it is simplified with two noise current sources between port 1 and ground, and between port 2 and ground, those noise power sources must be correlated, and their values can not be calculated by equations 3.26, 3.27 and 3.30.

It is interesting to compare the Figures 4.21b and 4.22b; in the former, the SGAI simulation results shows larger quality factor than the *perfect active resonator model* (PARM) predictions, while in the latter, the BFAI simulation results shows smaller values of quality factor than the PARM predictions. This motivates the analysis of how to use this new complete model to increase the circuit performance (i.e. how to modify the transcapacitances between ports a and b).

There are publications that add some kind of RC filter at the input of the transconductors to change the equivalent value of transcapacitances between ports a and b. This is the case of Hsiao et al. [30], Szczepkowski and Farrell [10] and Ler et al. [6].

However, maybe a more simple approach, analogous to the tuning of capacitors C_a

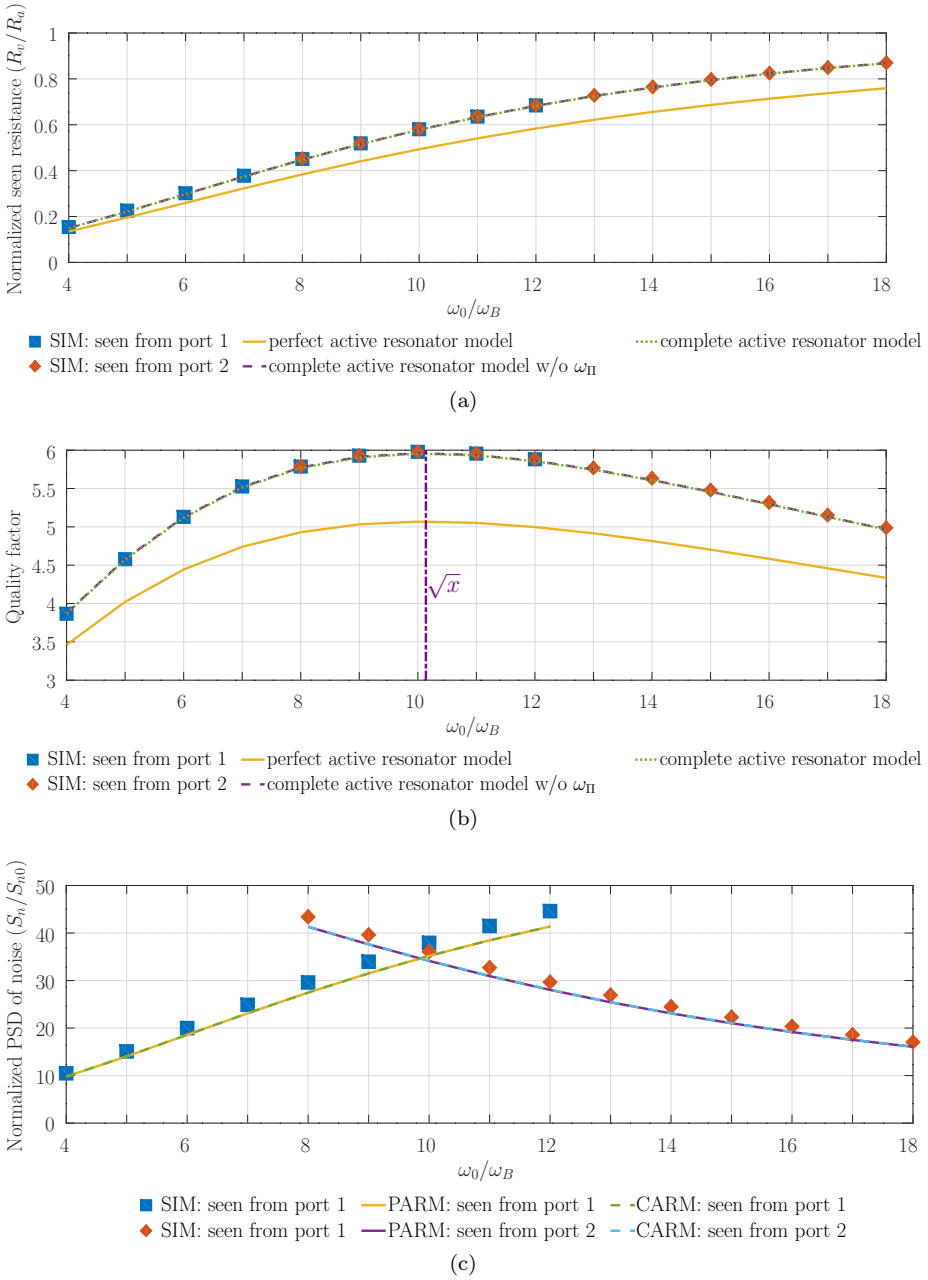

Figure 4.21: Results obtained from simulations of SGAI architecture (using the *perfect active resonator model* to set the resonance frequency), compared with the *perfect active resonator model* (PARM) developed in Chapter 3, and with the *complete active resonator model* (CARM) developed in Section 4.7 (with and without the term ω_Π).

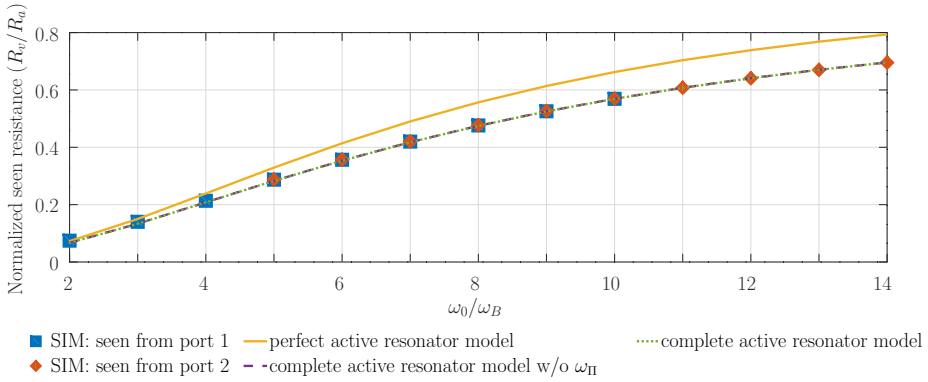

(a)

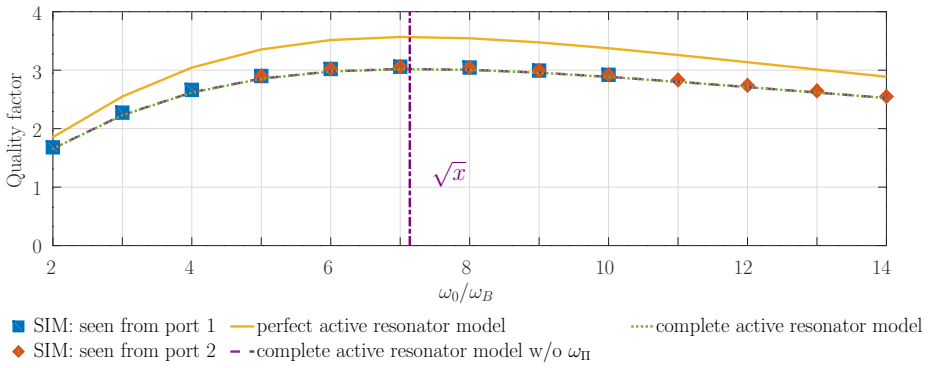

(b)

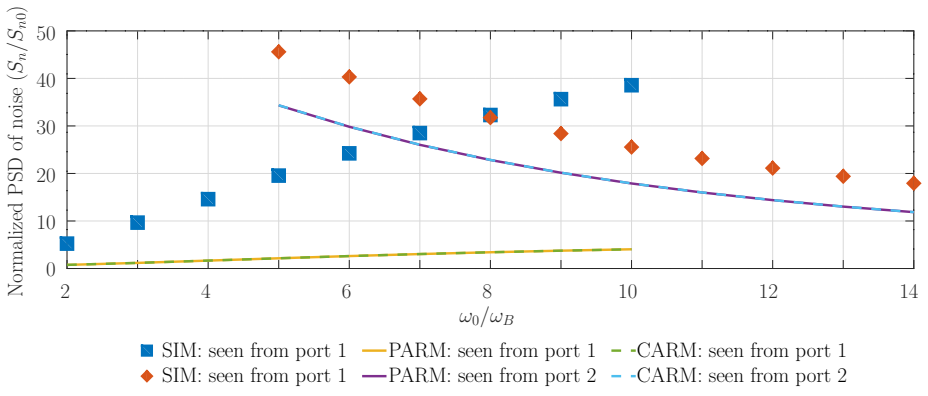

(c)

Figure 4.22: Results obtained from simulations of BFAI architecture (using the *perfect active resonator model* to set the resonance frequency), compared with the *perfect active resonator model* (PARM) developed in Chapter 3, and with the *complete active resonator model* (CARM) developed in Section 4.7 (with and without the term ω_Π).

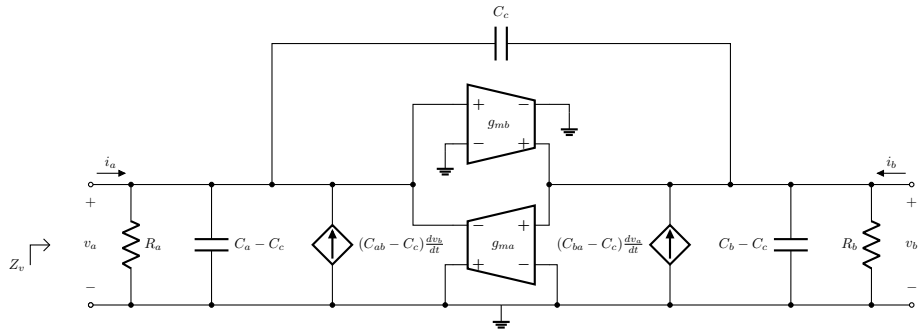

Figure 4.23: Complete model of the active resonator.

and C_b, is to add a cross-capacitor C_c between ports a and b as shown in Figure 4.23. Now, if there are parasitic transcapacitances C_{abp} and C_{bap} (between ports a and b), and parasitic capacitances C_{ap} and C_{bp} (between port a and ground, and between port b and ground respectively), the model parameters can be calculated as follows:

$$\omega_a = \frac{g_{ma}}{C_{ap} + C_{ae} + C_{ce}} \tag{4.35}$$

$$\omega_b = \frac{g_{mb}}{C_{bp} + C_{be} + C_{ce}} \tag{4.36}$$

$$\omega_{ab} = \frac{g_{ma}}{C_{abp} + C_{ce}} \tag{4.37}$$

$$\omega_{ba} = \frac{g_{mb}}{C_{bap} + C_{ce}} \tag{4.38}$$

$$\tag{4.39}$$

where C_{ae}, C_{be} and C_{ce} are the external capacitors used to tune the active resonator circuit.

How to increase the quality factor by the addition of a capacitance C_{ce}? From equation 4.28, an increase of Q implies an increase of ω_x^2 (assuming $\omega_x^2 > 0$). From equation 4.24, an increase of the value of ω_x^2, -and neglecting the factor $\frac{\omega_b}{\omega_\Pi}$-, implies an increase of the following expression:

$$x\frac{\omega_b}{\omega_\Delta} \approx \omega_0\sqrt{x}\frac{1}{\omega_\Delta} \qquad \omega_0/\omega_b \approx \sqrt{x} \tag{4.40a}$$

$$\approx \omega_0\sqrt{R_a R_b g_{ma} g_{mb}}\left(\frac{C_{ab}}{g_{ma}} - \frac{C_{ba}}{g_{mb}}\right) \tag{4.40b}$$

$$\approx \omega_0\sqrt{\frac{R_a R_b g_{mb}}{g_{ma}}}\left[C_{abp} + C_{ce} - \frac{g_{ma}}{g_{mb}}(C_{ba} + C_{ce})\right] \tag{4.40c}$$

$$\approx \omega_0\sqrt{\frac{R_a R_b g_{mb}}{g_{ma}}}(C_{abp} + C_{ce}) \qquad g_{mb} \gg g_{ma} \tag{4.40d}$$

$$\tag{4.40e}$$

which was evaluated near the maximum of the quality factor ($\omega_0/\omega_b \approx \sqrt{x}$). It is clear the need of $g_{ma} << g_{mb}$ and also the need of large values of R_a and R_b because the expression in 4.40 needs to be comparable to 1.

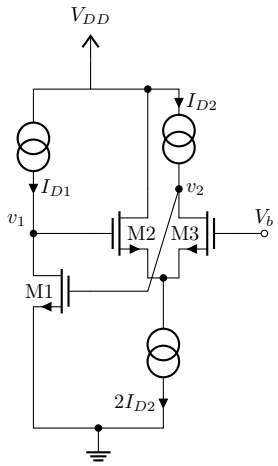

Figure 4.24: Schematic of the *high impedance simple grounded active inductor* (HI-SGAI) architecture.

4.7.1 High impedance SGAI

The expression given by equation 4.40 applied to the SGAI architecture cannot be very large because it requires larger values of C_{ce} that implies negative values of C_{be} (or, otherwise, ω_0/ω_b becomes very large and far from the optimum value $\sqrt{x}$).

This motivates the design of a new architecture, with a larger value of R_{22} than that for the SGAI case. This new architecture, called *high impedance SGAI* (HI-SGAI), is schematized in Figure 4.24 (in which, as before, the external capacitors were omitted).

Figures 4.25 and 4.26 show the simulation results (Simulation C.10) of the HI-SGAI architecture swiping the value of the capacitor C_{ce}. Figure 4.26 shows the equivalent resistance at resonance frequency normalized to the R_a value; the quality factor, the normalized PSD of noise and the third order intercept point (IIP3 if the active resonator is at the input, or OIP3 if it is at the output). Figure 4.25 shows a transient simulation of the $C_{ce} = 20\ fF$ case.

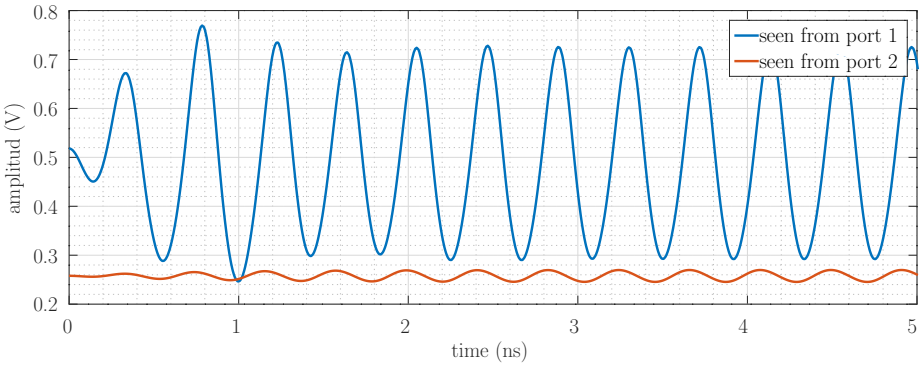

Figure 4.25: Transient simulation results for the new architecture *high impedance simple grounded active inductor* (HI-SGAI), seen from both, port 1 and port 2, using $C_{ce} = 20\ fF$.

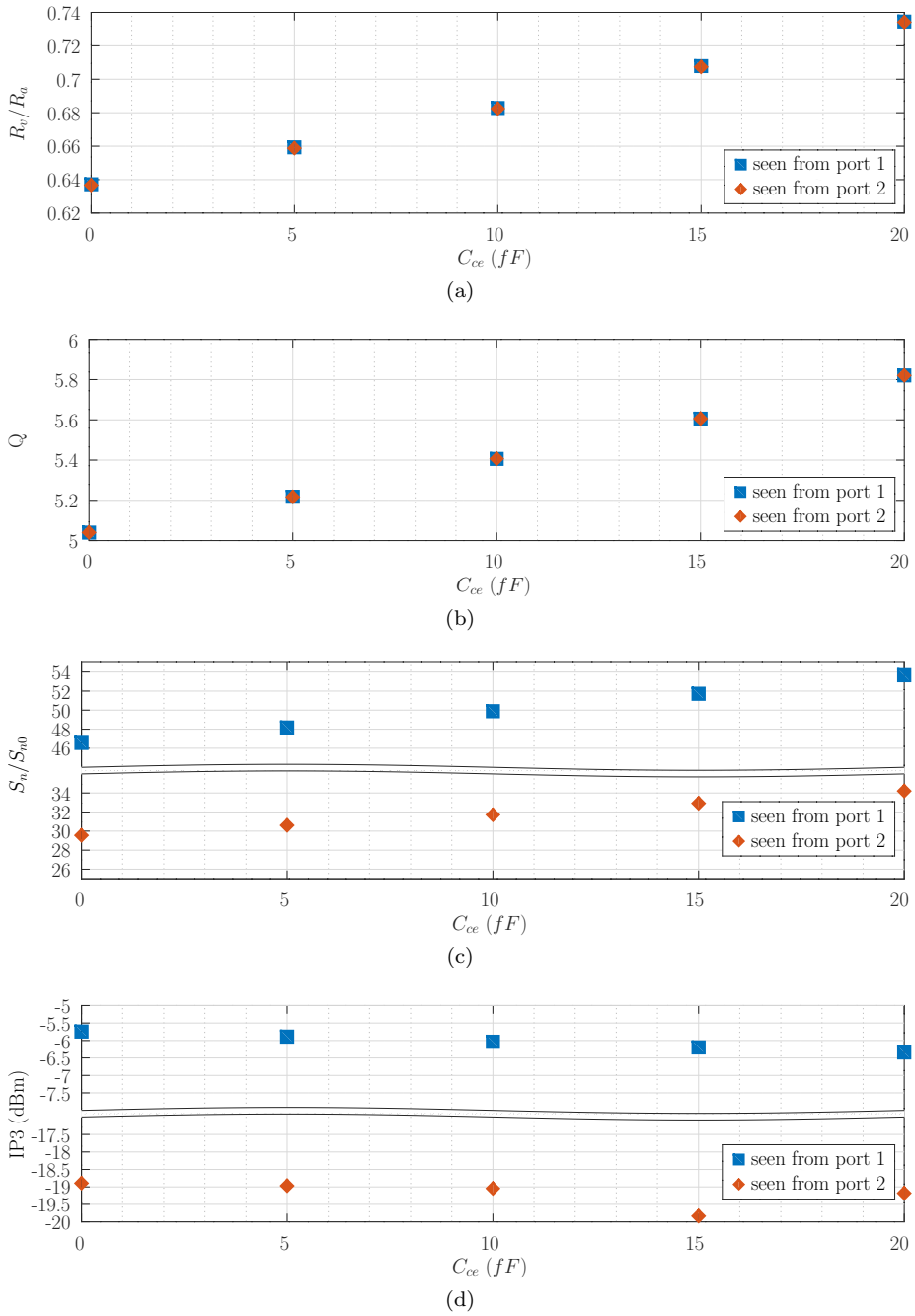

Figure 4.26: Simulation results for the new *high impedance-simple grounded active inductor* (HI-SGAI) architecture, varying the capacitance C_{ce} from 0 to 20 fF and seen from both, port 1 and port 2. More detailed result in Simulation C.10.

This page was intentionally left blank.

Chapter 5

Application example: feasibility of tunable LNA

The aim of this chapter is to show a complete implementation of an active resonator as an input stage of a low noise amplifier (LNA). The design will finish with a design and characterization of the LNA.

The target voltage gain and input impedance will be 10 dB and 50 Ω respectively. Although the previous chapter proposes two novel architectures for active resonators, the present example will be developed over the *simple grounded active inductor* (SGAI), to take advantage of the numerous simulations done to test the model. The use of the novel architectures is left for future works.

As was done before, some simulation details are reported in the Appendix C and referenced here with the simulation number.

5.1 LNA overview

A low noise amplifier (LNA), usually the first active stage in the front end of RF receivers, requires a careful design in several aspects like high gain, unconditional stability, low noise figure, good impedance match at input and at output, high linearity and low power consumption [31].

There are numerous architectures to implement an LNA [32]. The used in this work is the *resistive termination* topology schematized in Figure 5.1. The principal drawbacks of this architecture is its poor noise performance (result of the resistance R_{in}) and the capacitive component of the transistor gate (which leads to a not purely resistive input impedance). However, it is a practical topology to apply the active resonator model:

- it is a very simple design in which one or both resistors (R_{in} and R_{out}) can be easily replaced by active resonators;
- the poor noise performance presents an interesting challenge to explore the results of Section 4.4 (i.e. the possibility of an active resonator to generate less noise than the passive counterpart);
- the capacitive component of the transistor gate can be included in the capacitance C_{ae} added to tune the active resonator.

5.2 Active resonator at the LNA input

To incorporate an active resonator in place of R_{in} (schematic of Figure 5.1), it will be used the *simple grounded active inductor* (SGAI) exposed in previous chapters. From the analysis made of the Figure 4.12, it is clear that the SGAI must be used, in this case, seen from port 2. The operating point will be close to the one used in Section 4.4 (i.e. one in which the generated noise is smaller than the passive counterpart).

The Simulation C.6 (results shown in Figure 4.10) has the following parameters:

- $I_{Dtot} = 1\ mA$ and $I_{D2}/I_{D1} = 0.09$ ($I_{D1} = 917\ \mu A$ and $I_{D2} = 83\ \mu A$)
- $(g_m/I_D)_{M1} = 23.5\ V^{-1}$ and $(g_m/I_D)_{M2} = 10\ V^{-1}$
- $R_v = 103\ \Omega$, $R_{11} = 6.4\ k\Omega$ and $R_{22} = 1.1\ k\Omega$
- $C_{1e} = 31\ fF$ and $C_{2e} = 482\ fF$

The first step is to achieve 50 Ω of equivalent impedance, so the total current needs to be updated as following:

$$I_{Dtot@50\Omega} = I_{Dtot@103\Omega}\frac{103}{50} = 2.06\ mA \tag{5.1}$$

and the simulation (Simulation C.11) results in the following parameters:

- $I_{Dtot} = 2.06\ mA$ and $I_{D2}/I_{D1} = 0.09$ ($I_{D1} = 1.9\ mA$ and $I_{D2} = 170\ \mu A$)
- $(g_m/I_D)_{M1} = 23.5\ V^{-1}$ and $(g_m/I_D)_{M2} = 10\ V^{-1}$
- $R_v = 50.2\ \Omega$, $R_{11} = 3.1\ k\Omega$ and $R_{22} = 529\ \Omega$
- $C_{1e} = 63\ fF$ and $C_{2e} = 975\ fF$

5.2.1 Current sources design

The next step is to design the current sources; they must have less capacitance than the external C_{1e} and C_{2e} used in each port, and also an output resistance much higher than R_{11} and R_{22} respectively:

1. ID1 has the following requirements:
   - $I_D = 1.9\ mA$
   - $R_{out} \gg 3.1\ k\Omega$

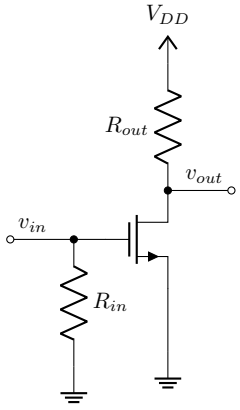

Figure 5.1: Schematic of the *resistive termination* low noise amplifier (LNA).

- $C_{out} \leq 63\ fF$

2. ID2 has the following requirements:
   - $I_D = 170\ \mu A$
   - $R_{out} \gg 529\ \Omega$
   - $C_{out} \ll 975\ fF$[1]

It is clear that the requirements of current source ID1 are more constrained than those of the current source ID2. The design will start with the last one.

The most simple architecture of current source is the MOS current mirror shown in Figure 5.2a. In that circuit, N1 and N2 must have the same length, and the width will determine the copy ratio. In this case, ID2 is about one tenth than the total current consumption, so it is not a bad design if the copy ratio is 1:1 and the current source consumes an extra current of 170 μA.

To evaluate the best performance point of the current source, a group of simulations was done, with N1 equal N2, both with a fixed finger with of 250 nm[2]. The sweep was done over the number of fingers and the channel length. The load was replaced by a voltage source of 650 mV. Results are shown in Figure 5.3. Figure 5.3a shows the constraints between the output capacitance C_o and the output resistance R_o of the current source. In this case (current source ID2) the design is not very restrictive, but there are, also, other considerations that could be taken into account, for example:

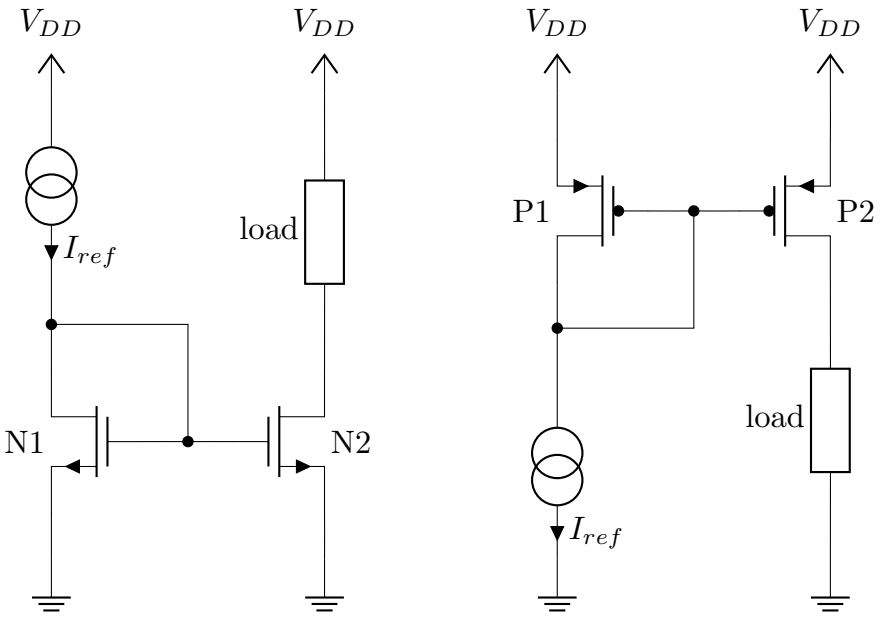

(a) NMOS current mirror. (b) PMOS current mirror.

Figure 5.2: Schematic of NMOS and PMOS current mirrors.

[1]There will be other capacitances attached to this node, later it will be clear the needed of C_{out} *much less* than this value.

[2]The minimum width of the technology is 206 nm, but, for better matching of the current mirror, a finger width of 250 nm was chosen.

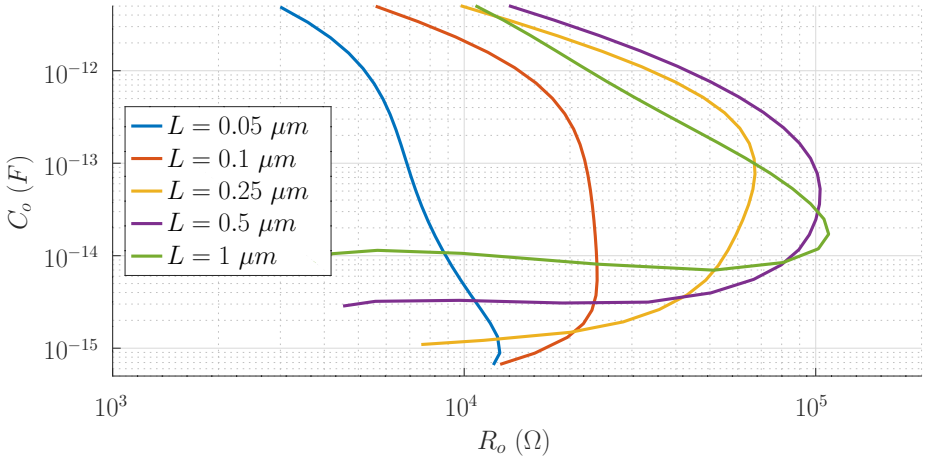

(a)

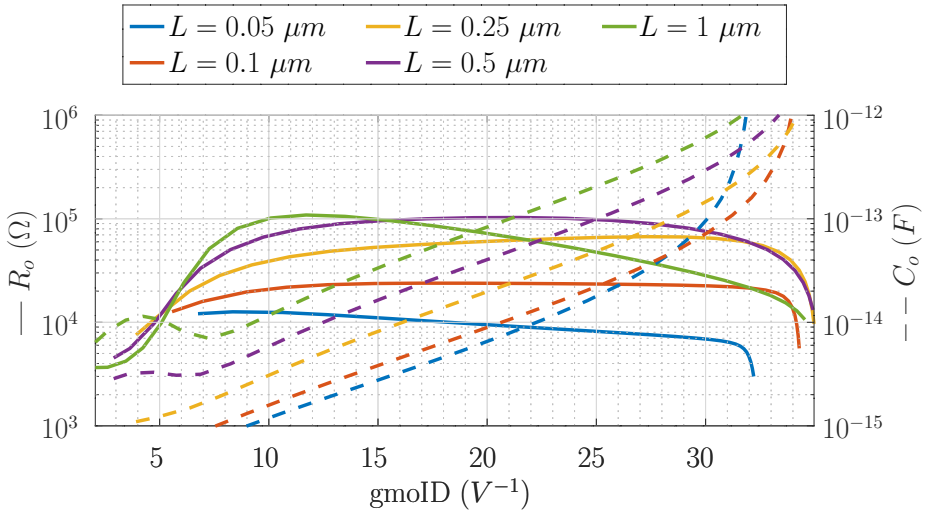

(b) Output resistance (continuous) and output capacitance (dashed).

Figure 5.3: Simulation results of the NMOS current mirror shown in Figure 5.2a, varying the transistor channel length.

- Avoid the use of minimum lengths and widths to get a better matching of the current mirror; 100 nm is a suitable value for the transistors' length.
- Noise of current mirror grows with the gmoID value; Figure 5.3b shows the value of C_o and R_o as a function of the gmoID value of the transistors.

With the simulation results and the above considerations, the chosen design for the NMOS current source ID2 was

- $I_{ref} = 179\ mA$
- $L_{N1} = L_{N2} = 100\ nm$
- $(g_m/I_D)_{N1} = (g_m/I_D)_{N2} = 10\ V^{-1}$

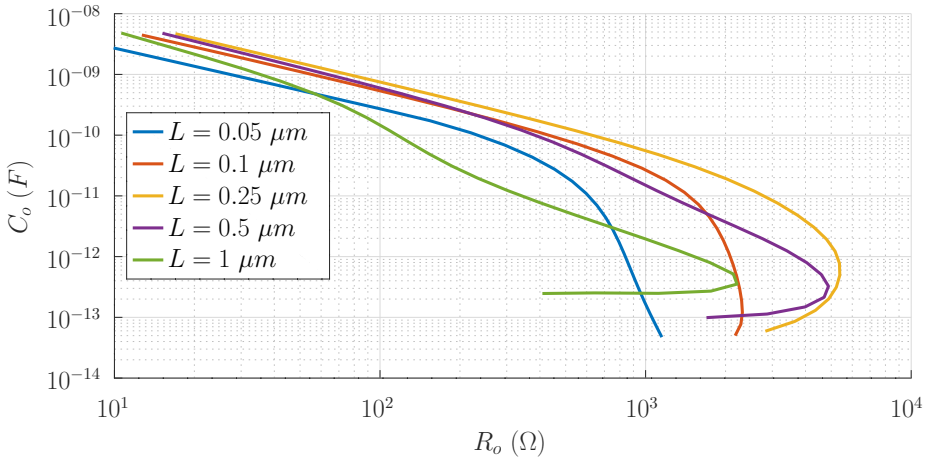

Figure 5.4: Simulation results of the PMOS current mirror shown in Figure 5.2b, for different channel lengths.

The current source ID1 has more restrictive constrains. The dual p-channel of the schematic of Figure 5.2a is shown in Figure 5.2b. This current source must deliver about ten times more current than ID2. In order not to increase the power consumption too much, the copy ratio of this current source will be 1:10, so the channel width of P2 will be ten times larger than the channel width of P1.

Figure 5.4 shows the performance of this current source based on simulations. It is clear that the requirements of ID1 are not covered by the simple architecture of Figure 5.2b.

A workaround to better satisfy the ID1 requirements is to use the cascoded current mirror shown in Figure 5.5 [33]. With this new architecture, the design constraints, based on simulations, are shown in Figure 5.6. This clearly improves the performance of the current source.

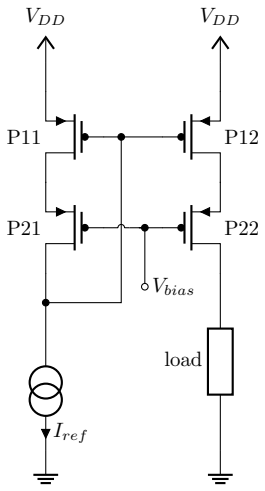

Figure 5.5: Schematic of the cascoded current mirror, taken from [33].

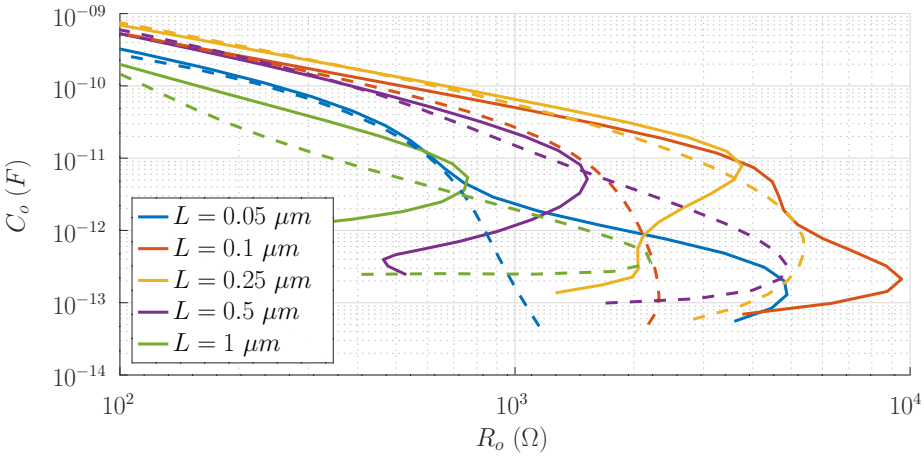

Figure 5.6: Simulation results of the cascoded current mirror (continuous line) superposed with the simple current mirror (dashed line).

Another possible improve is to make the upper transistors P11 and P12 with different widths than the lower transistors P21 and P22. This is sometimes called *triangular* cascode and its simulation results are shown in Figure 5.7.

The results of this *triangular* cascode, shown in Figure 5.7 are not better than the cascode in which upper transistors P11 and P12 are equal to their respectively lower transistors P21 and P22. So the chosen design for the current source ID1 will be the architecture shown in Figure 5.5.

As was shown before, the requirements will not be completely satisfied; either the output capacitance C_o or the output resistance R_o will not cover the initial conditions of $\leq 63\ fF$ and $\gg 3.1\ k\Omega$ respectively. The priority will be over R_o, so the design will be with g_m/I_D of the four transistors equal to 16 V^{-1}. The large capacitance will

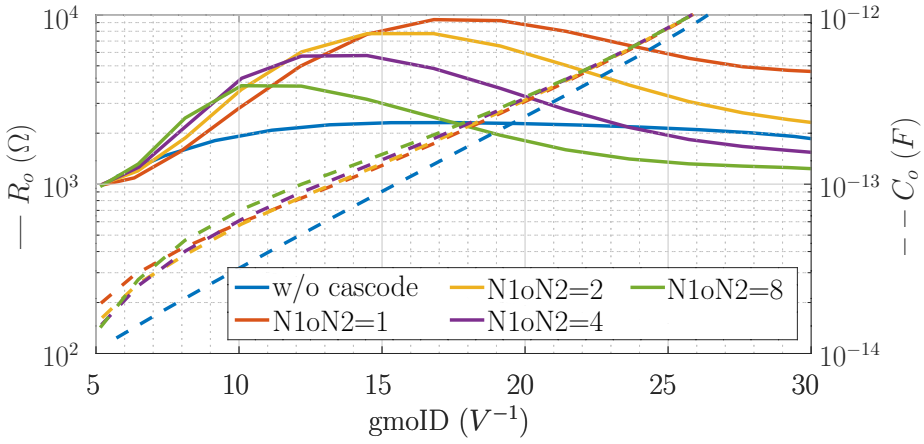

Figure 5.7: Simulation results of the 100 nm channel length, cascoded current mirror varying the relationship between transistor widths $N1/N2$; N1 is the number of fingers of M11 and M12, and N2 is the number of fingers of M21 and M22. The simple current mirror (without cascode) is superposed for reference.

imply that the ω_b will not be the optimum value (in terms of the quality factor) and some adjustments could be needed to approach the initial proposed results.

5.2.2 Overall design

The complete schematic of the low noise amplifier, with the active resonator as the input stage, is shown in Figure 5.8.

M1 and M2 constitute the active resonator, while M3 is the transistor amplifier. P11, P12, P21 and P22 constitutes the PMOS current source ID1 while N1 and N2 the NMOS current source ID2.

Between nodes v_1 and ground, and between the nodes v_2 and ground, capacitors must be connected in order to configure the active resonator at the desired frequency with the required values of ω_a and ω_b. As was explained before, this capacitances will must take in account the parasitic capacitances of all transistors, including the gate capacitances of M3.

What remains to be designed is the transistor M3 and its load resistor R_L. The gate of M3 has the same potential as the gate of M1, so the most simple design is that both transistors have the same channel length and the same inversion level. If $(g_m/I_D)_{M1} = (g_m/I_D)_{M3} = 23.5\ V^{-1}$, the remaining variable to be defined is the current through M3 since the value of R_L will be calculated from the g_m of M3 and

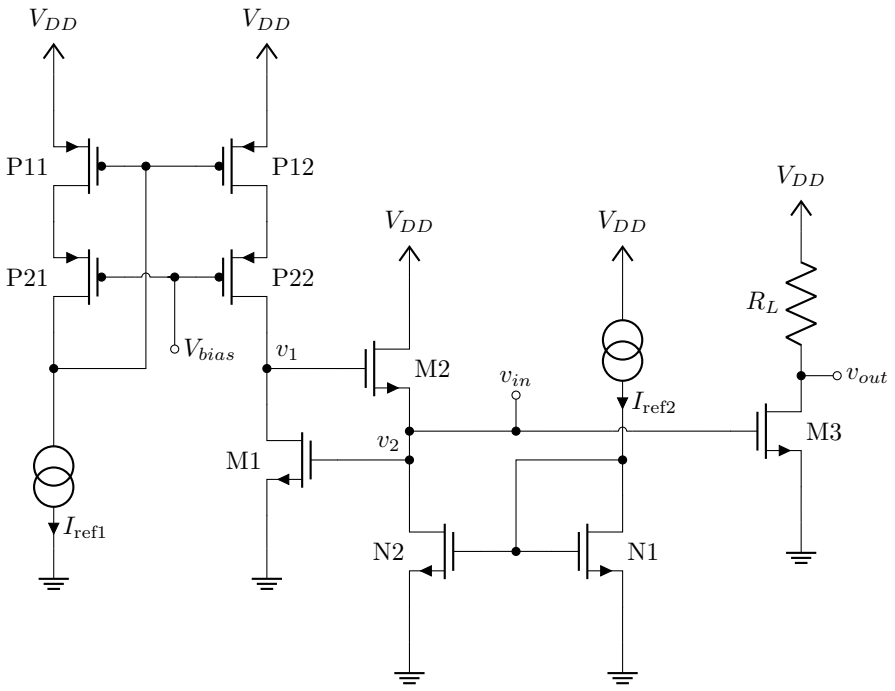

Figure 5.8: Schematic of the overall LNA design with active resonator as the input stage.

the desired voltage gain[3] of 10 dB:

$$G = 20\log_{10}(g_{m3}R_L) = 10 \Longrightarrow R_L = \frac{\sqrt{10}}{g_{m3}}. \tag{5.2}$$

Larger current through M3 implies less noise generated by this transistor but more power consumption, and, also large gate capacitance, so the value of ω_b will move further away from the optimum.

Figures 5.9 and 5.10 shows the results of a group of simulations (Simulation C.12) of the circuit schematized in Figure 5.8 varying the current of M3 (with constant values of $(g_m/I_D)_{M3}$ and gain). The noise figure (Figure 5.9a) is the most relevant

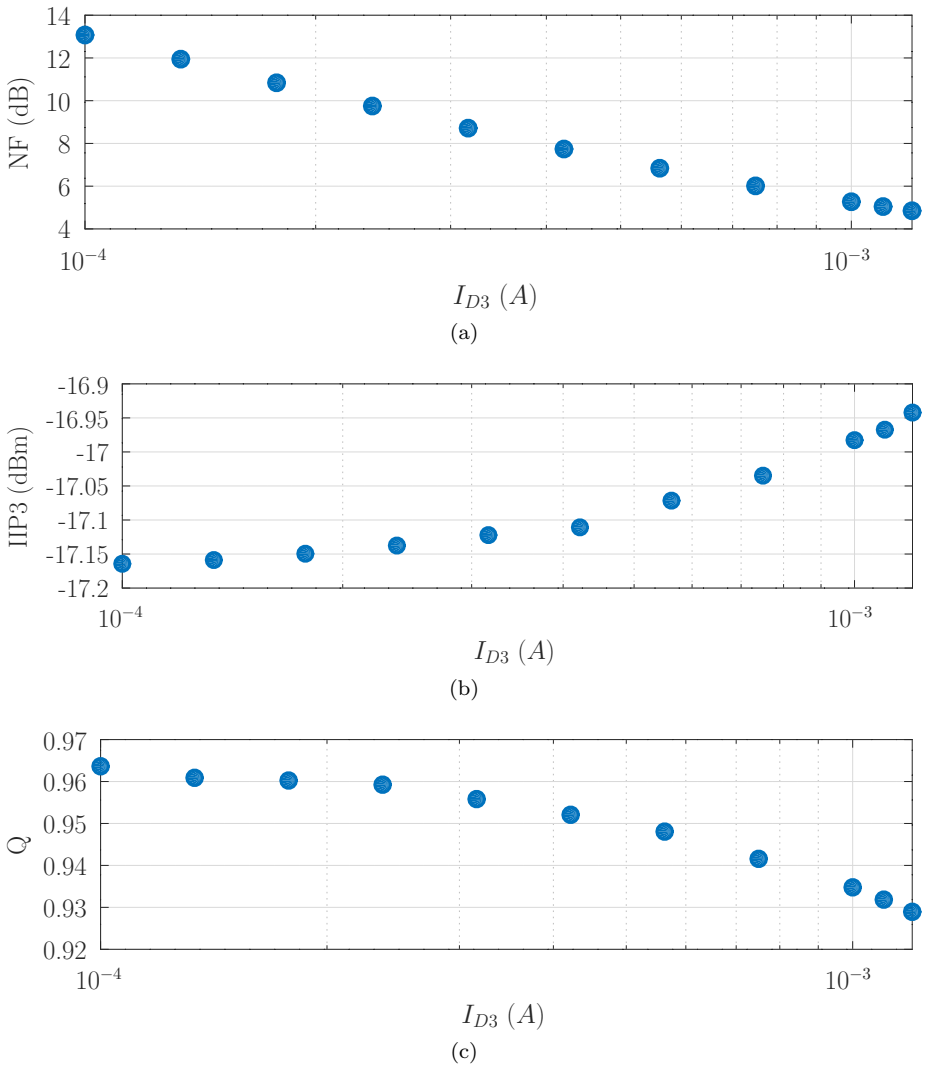

Figure 5.9: Noise figure, linearity, quality factor,—in all cases evaluated at resonance frequency—simulation results for the circuit shown in Figure 5.8 varying the M3 drain current.

[3]Corresponds to the power gain if the output is impedance matched.

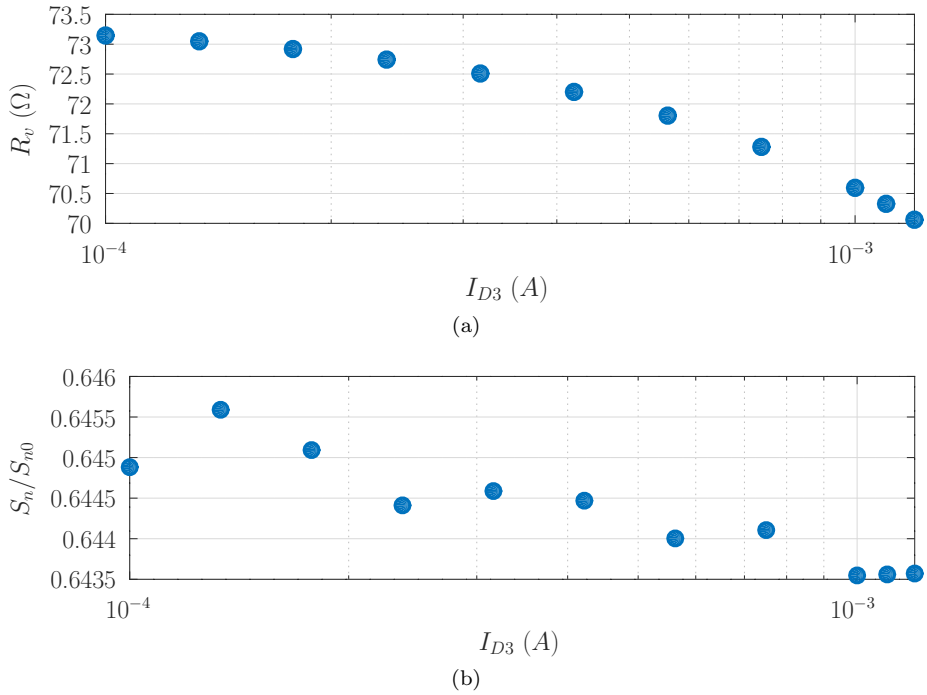

Figure 5.10: Equivalent resistance and normalized noise PSD,—in all cases evaluated at resonance frequency—simulation results for the circuit shown in Figure 5.8 varying the M3 drain current. S_n/S_{n0} is the normalized PSD of noise at the gate of M3, i.e. considering only the active resonator with its current sources.

magnitude in the sweep. It falls with the M3 drain current. Linearity, quality factor, equivalent resistance and normalized PSD of noise (Figures 5.9b 5.9c, 5.10a and 5.10b respectively) are quite constant with I_{D3} current. The sweep was done until 1.2 mA because at this point the additional capacitance at port a (port 2, gate of M3) was less than 50 fF, too small and very susceptible to parasitic capacitances. So the choice to M3 drain current is 1.0 mA in order to stay far from the limit and also obtain a low noise figure.

The quality factor is a bit lower than 1, and the normalized PSD of noise is also considerably lower than 1, so the sweep of I_{D2}/I_{D1} can be performed again, as was done in Section 4.4 but now with the complete system of Figure 5.8. The results of these simulations (Simulation C.13), using 1.0 mA for I_{D3}, are in Figures 5.11, and 5.12.

Linearity, noise figure and normalized noise PSD (Figures 5.12, 5.11a and 5.11b respectively) has better performance for lower values of I_{D2}/I_{D1}. The simulation was done from $I_{D2}/I_{D1} = 0.08$ because in this point, again, the value of C_{ae}, the added capacitor to tune the resonance frequency, has less than 50 fF, so the circuit becomes very susceptible to parasitic capacitances.

Equivalent resistance and quality factor are shown in Figures 5.11d and 5.11c respectively. The counterpart of low values of I_{D2}/I_{D1} are the lower quality factor and higher equivalent resistance (i.e. more current to achieve 50 Ω of input resistance). The new value chosen for this complete design of LNA is $I_{D2}/I_{D1} = 0.1$. So the total

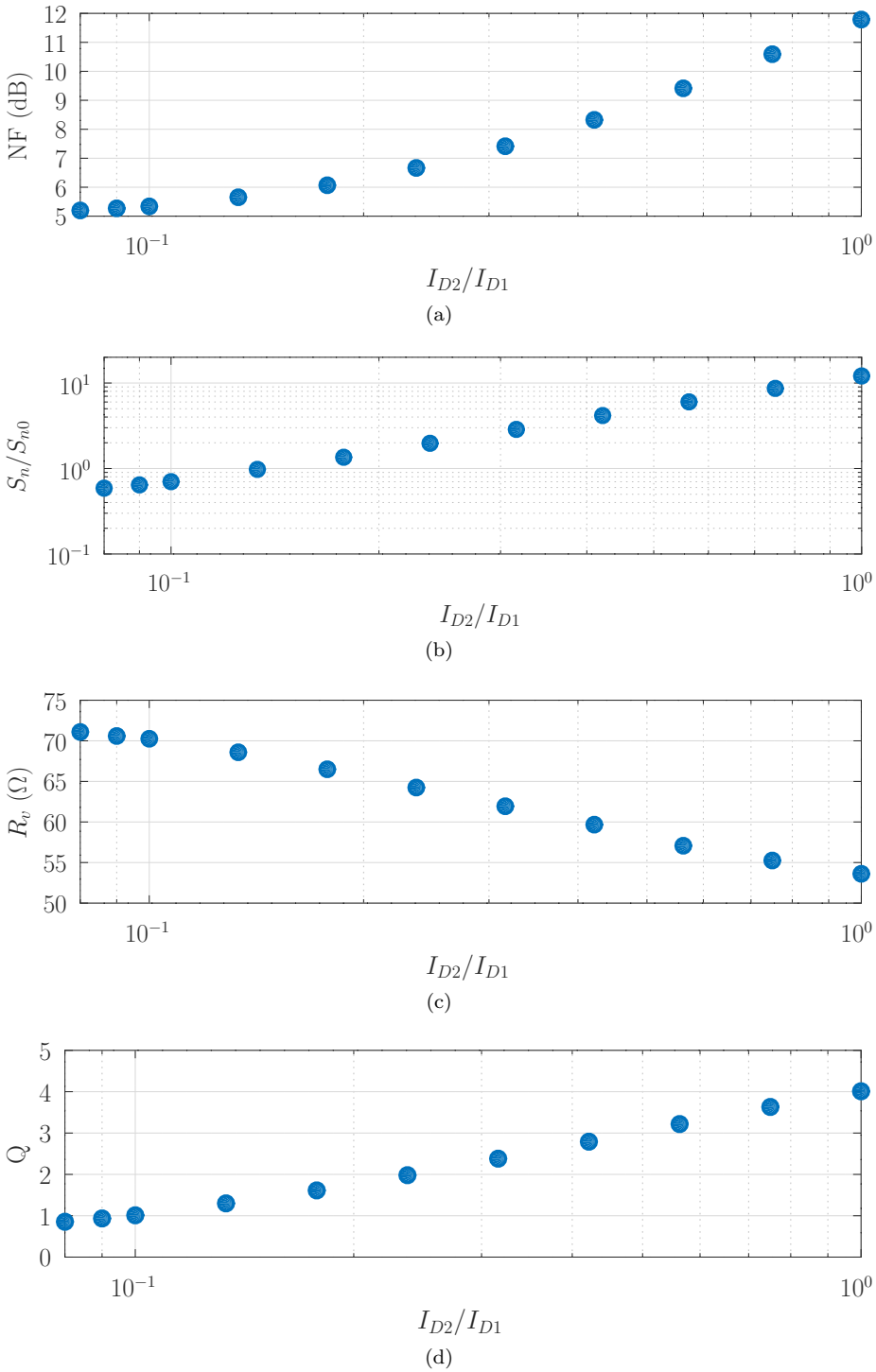

Figure 5.11: Noise figure, normalized noise PSD, equivalent resistance and quality factor,—in all cases evaluated at resonance frequency—simulation results for the circuit shown in Figure 5.8 varying the relation I_{D2}/I_{D1} with a constant sum of both ($I_{D1} + I_{D2} = 2.06\ mA$). S_n/S_{n0} is the normalized PSD of noise at the gate of M3, i.e. considering only the active resonator.

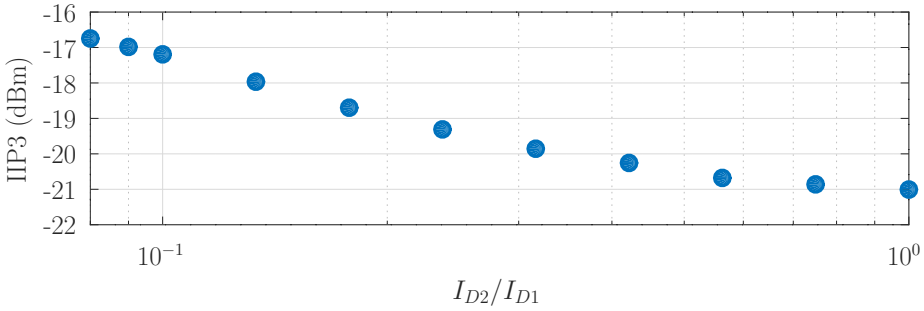

Figure 5.12: Linearity simulation result, evaluated at resonance frequency, for the circuit shown in Figure 5.8 varying the relation I_{D2}/I_{D1} with a constant sum of both ($I_{D1} + I_{D2} = 2.06\ mA$).

SGAI current (i.e. $I_{D1} + I_{D2}$) needs to be scaled again, with a new value

$$I_{D1} + I_{D2} = 2.06\frac{70}{50} = 2.884\ mA. \tag{5.3}$$

Now the design is complete, the LNA of Figure 5.8 is characterized in Figures 5.13, 5.14 and 5.15.

Figures 5.13a and 5.13b shows the performance of the active resonator in comparison with its passive counterpart. Note that this design was done as a proof of concept, in which the consistency and accuracy of the model and their subsequent results could

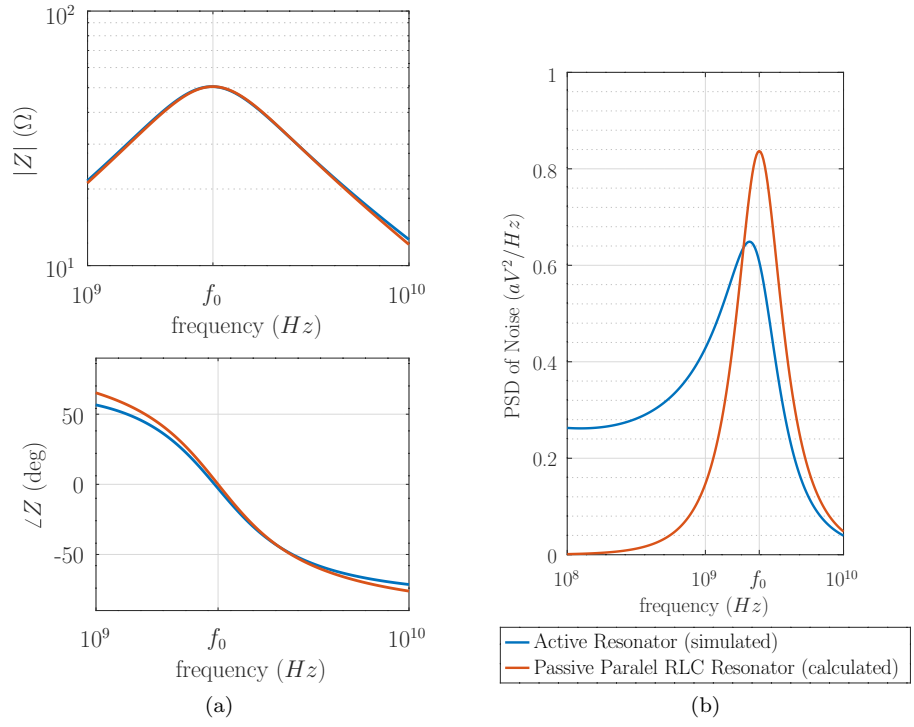

Figure 5.13: Performance of the active resonator used in the circuit of Figure 5.8, in comparison with its passive—theoretical—counterpart. The evaluation is at the gate of M3.

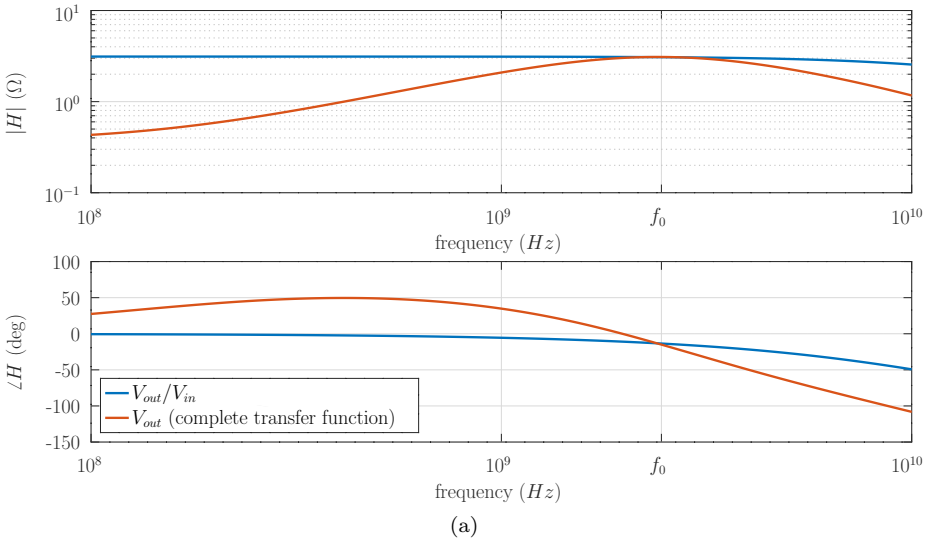

(a)

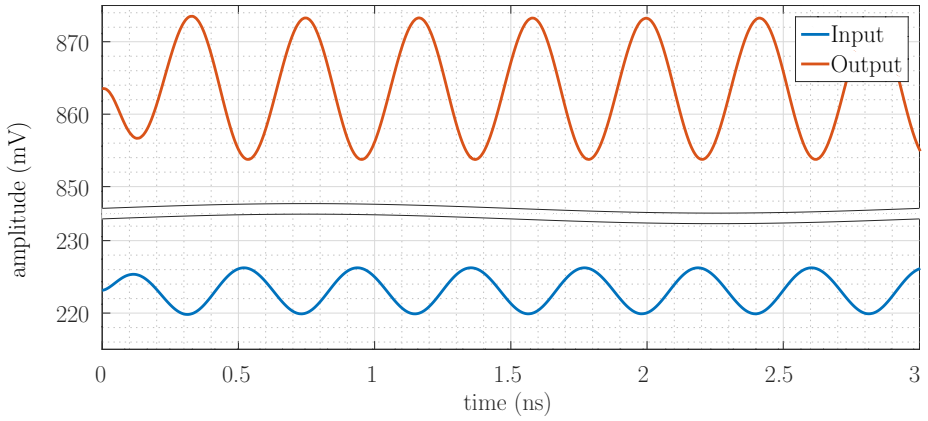

(b)

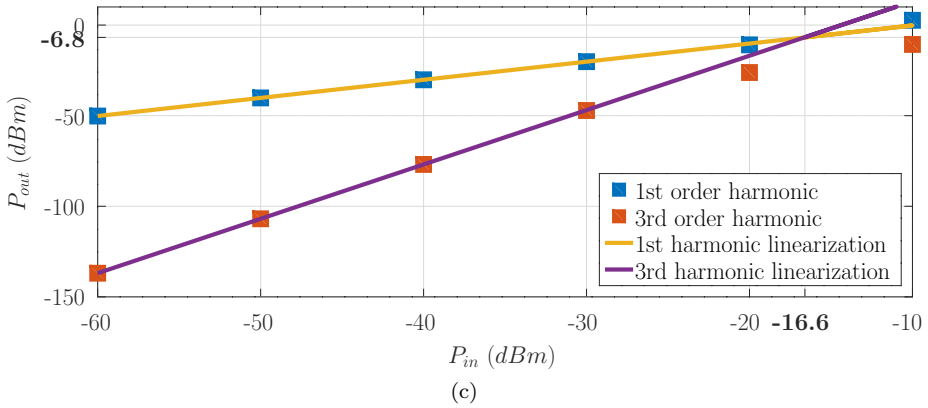

(c)

Figure 5.14: Simulation results of the circuit shown in Figure 5.8.

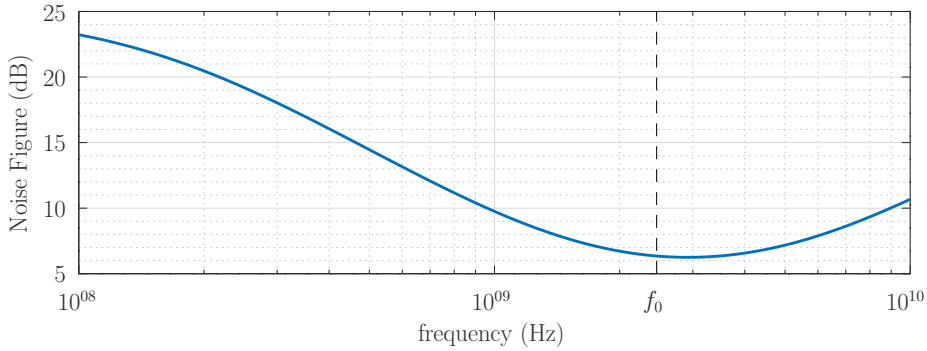

(a)

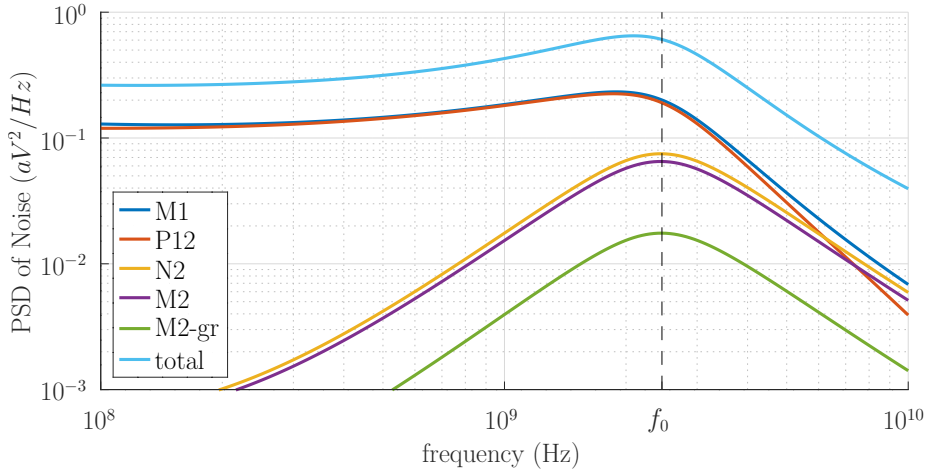

(b) "M2-gr" label corresponds to the contribution of gate resistance of M2 transistor.

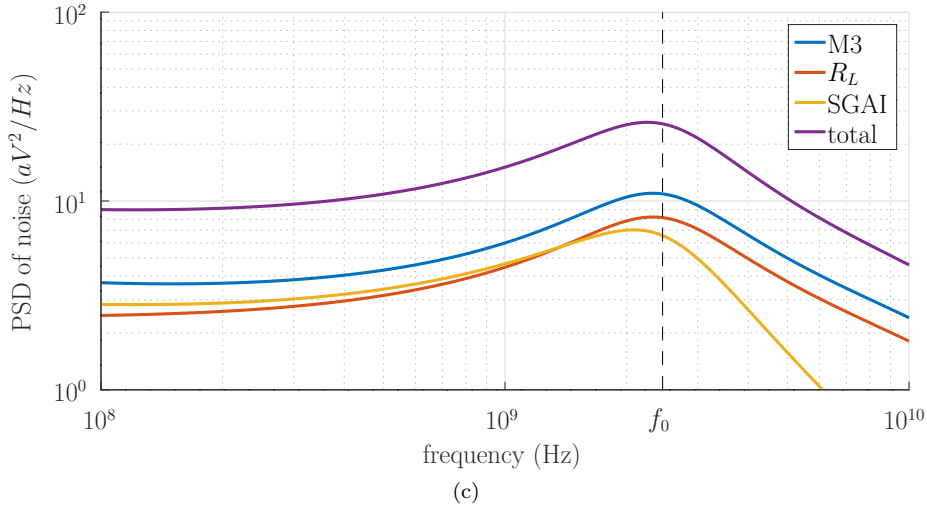

(c)

Figure 5.15: Simulation results of the circuit shown in Figure 5.8.

be tested in a more real environment. This is the context in which the comparison with the passive counterpart is given. The theoretical passive resonator is a parallel RLC with $R = 50\ \Omega$, $L = 3.09\ nH$ and $C = 1.36\ pF$.

Figure 5.14a shows the AC response of the amplifier, discriminating the transfer from the gate transistor and the overall system (considering the 50 Ω source resistance). Figure 5.14b shows a transient simulation with $-40\ dBm$ power input. The linearity (IIP3/OIP3) is shown in Figure 5.14c. The simulation done with a fundamental tone at $2.4\ GHz$ and a secondary tone at $2.35\ GHz$. The noise figure, shown in Figure 5.15a, shows a performance of $6.25\ dB$ at resonance frequency, and grows as it moves away from it. Figure 5.15b, discriminates the noise contributions of the active resonator, while Figure 5.15c, shows it in comparison with the overall amplifier.

At this point, it is interesting to analyse the possibility of obtain a similar behaviour with an SGAI architecture as an output stage of the LNA. The first and most restrictive parameter—as was shown at the end of Chapter 3—is the linearity (IIP3). The obtained IIP3 performance with this example design (with an active resonator at the LNA input) is $-16.6\ dBm$ which implies an OIP3 of $-6.6\ dBm$. Seen the simulations shown in Figure 4.12, it is clear that to achieve an IP3 greater than 10 dBm the SGAI architecture must be seen from port 1. Then, from the analysis done in Section 4.6, in particular from Figure 4.16a, the current consumption needed to achieve a NF less than 7 dB, only taking into account the transistors M1 (of the SGAI) and M3 (LNA transconductance), is greater than 100 mA. This is a very good example that, as discussed at the end of Section 3.3, it is more convenient to place the active resonator at the input instead of at the output of the LNA.

To clarify; the SGAI architecture seen from port 2 has a low impedance, attractive to use as the LNA load. But the linearity of the architecture seen from that port is very poor, so the SGAI architecture to use as the LNA load needs to be seen from port 1 which has a very large impedance. Then, it needs a lot of bias current to reduce its equivalent impedance without reducing the quality factor.

5.2.3 Tunability

Fine and continuous tunability was simulated adjusting the bias current sources I_{D1} and I_{D2} in a range of ±20 %. The simulation was done in steps of 5 % obtaining 64 entries matrix results.

Figure 5.16 shows the resonance frequency, which grows with both bias currents as was predicted by the analysis of equation 4.7.

Figure 5.17a shows the input resistance that falls almost with I_{D1} and smoothly with I_{D2}. To explain this difference in the behaviour depending on the current being adjusted, it is necessary to incorporate the terms ω_x and ω_Δ from the *complete active resonator model* developed in Section 4.7. With this additional complexity, equation 4.8 becomes

$$R_v = \frac{R_a \frac{\omega_0^2}{\omega_b^2}}{x + \frac{\omega_0^2}{\omega_b^2}\left(1 - x\frac{\omega_b}{\omega_\Delta}\right)} = \frac{1/C_a}{\frac{g_{oa}}{C_a} + \frac{g_{ob}}{C_b} + \frac{g_{ma}}{C_a}\frac{C_{ba}}{C_b} - \frac{g_{mb}}{C_b}\frac{C_{ab}}{C_a}}. \tag{5.4}$$

Remembering that g_{mb} is the opposite of the real part of y_{ba} (equation 3.40) which corresponds to y_{12} (equation 4.1c) whose value is g_{m1} (equation 4.3a), the term $-\frac{g_{mb}}{C_b}\frac{C_{ab}}{C_a} = \frac{g_{m1}}{C_b}\frac{C_{ab}}{C_a}$ sums to the term $\frac{g_{ob}}{C_b}$. In a similar way, g_{ma} is the real part of y_{ab} which corresponds to y_{21} whose value is $-g_{m2}$, so the term $\frac{g_{ma}}{C_a}\frac{C_{ba}}{C_b} = \frac{-g_{m2}}{C_a}\frac{C_{ba}}{C_b}$ tends to cancel the term $\frac{g_{oa}}{C_a} = \frac{g_{ds2}+ng_{m2}}{C_a}$ (equation 4.3a), in fact, $C_{ba}/C_b \approx 0.7$ for the design done in this chapter. This analysis explains that the equivalent resistance R_v is more sensitive to changes in I_{D1} than those in I_{D2}.

Quality factor is shown in Figure 5.17b. Figures 5.18a and 5.18b shows the noise figure and the linearity (IIP3) respectively. Those three parameters do not have relevant changes with the tuning current, at least in the range in which was done the simulation.

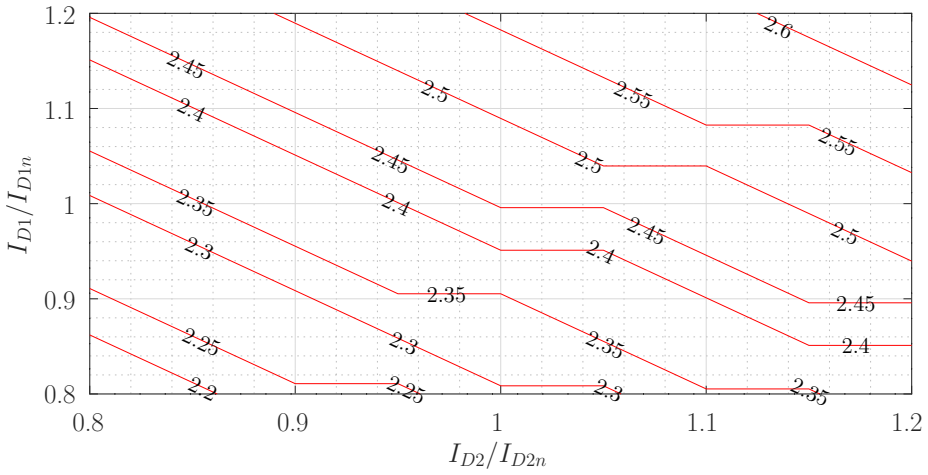

Figure 5.16: Resonance frequency (GHz) simulation results of the fine-tuning of the overall low noise amplifier. I_{D1} and I_{D2} are the simulated bias currents while I_{D1n} and I_{D2n} are the nominal bias currents used in the current design.

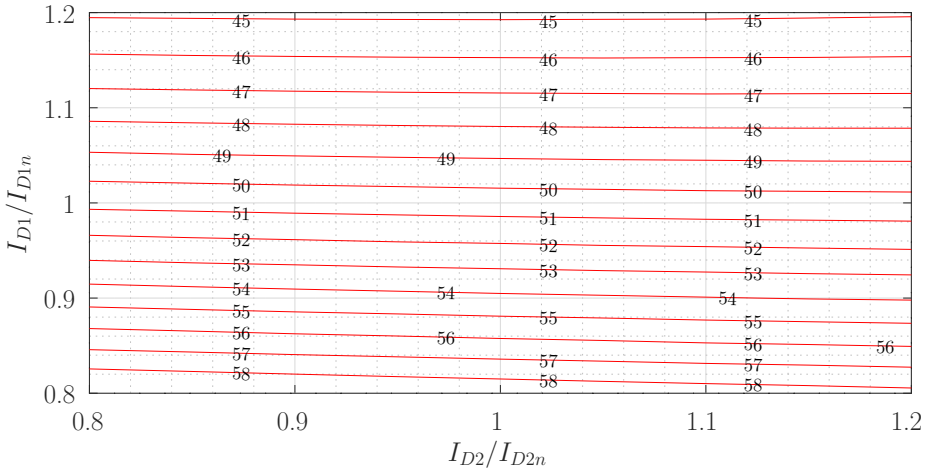

(a) Input resistance (Ω).

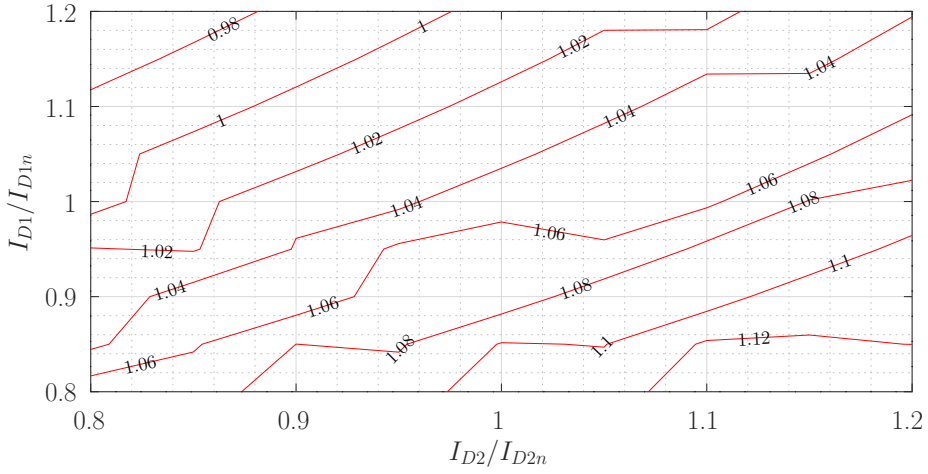

(b) Quality factor.

Figure 5.17: Simulation results of the fine-tuning of the overall low noise amplifier. I_{D1} and I_{D2} are the simulated bias currents while I_{D1n} and I_{D2n} are the nominal bias currents used in the current design.

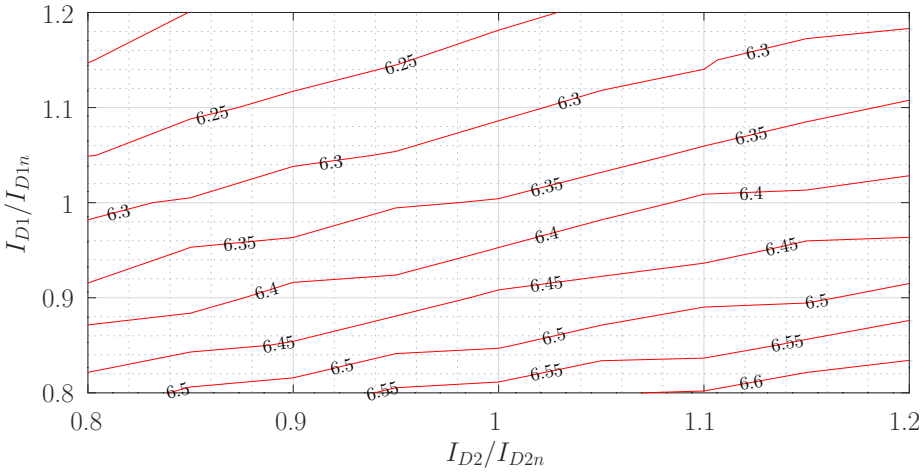

(a) Noise Figure (dB).

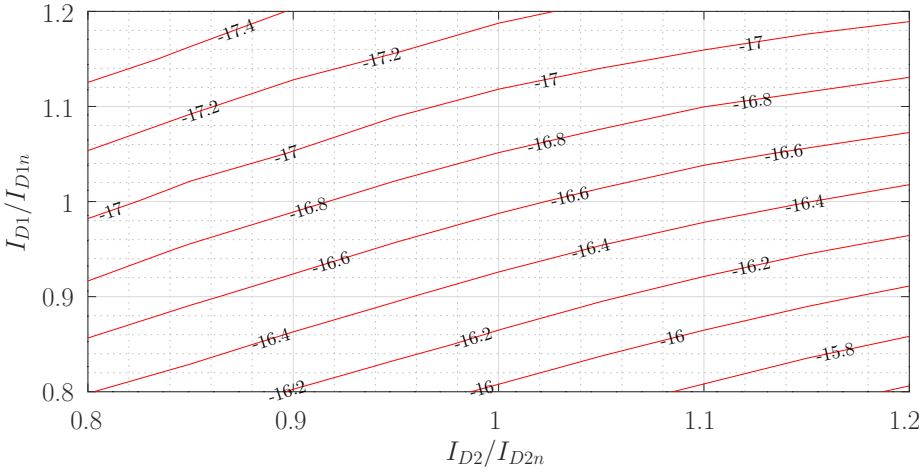

(b) 3rd order input intercept point (dBm).

Figure 5.18: Simulation results of the fine-tuning of the overall low noise amplifier. I_{D1} and I_{D2} are the simulated bias currents while I_{D1n} and I_{D2n} are the nominal bias currents used in the current design.

This page was intentionally left blank.

Chapter 6

Conclusions and future work

6.1 Conclusions

In this thesis, active resonators, built with active inductors, were presented in several levels.

Starting from the motivation, Chapter 1 introduces, in a brief and elementary way, an explanation of the active inductor operation while suggesting the need of the gyrator as its core.

Chapter 2 formalizes the gyrator definition and presents the *ideal active resonator*, from which chapter 3 develops the *perfect active resonator model* (PAR model).

The PAR model introduces some non-idealities (as the output conductance of the transconductors) and allows to easily design in the maximum Q operating point. Defined in Chapter 3, and linked with the transconductors intrinsic gain, x results in a *gyrator quality factor*, or, in other words, a figure of merit of the gyrator, and, therefore, of the active resonator. That chapter introduces the *normalized power spectral density of noise* quantity and shows the key to design an active resonator which generates less noise than its passive counterpart. The linearity is also taken into account in a qualitative approach. The trade-off between noise, linearity and power consumption were also analysed. This analysis concludes, and was shown in an example, that an active resonator will have better performance placed as the input stage than as the output stage of an LNA.

The *perfect active resonator model* (PAR model) was qualitatively validated in Chapter 4 through simulations. The model was applied to two standard architectures of active resonators in a very simple manner with accurate results. In that chapter, a new *low impedance simple active inductor* (LI-SGAI) architecture, deduced from the model characteristics, was proposed and simulated. A more complete model, which takes into account the input-output capacitive effects of the transconductors, was developed to improve the PAR model, whose results was also contrasted with simulations showing a better accuracy. Finally, another new *high impedance simple grounded active inductor* (HI-SGAI) architecture was simulated, and it proofs the possibility of improving the quality factor by the addition of a cross-capacitor between ports a and b.

The *perfect active resonator model* (PAR model) proved to be very powerful to design, analyse and compare qualitatively active resonator architectures, while the more complete model gives accurately results when performing computational analysis.

Finally, one of the standard architectures was tested in an overall design of a low noise amplifier (LNA) as its input stage, in a 28 nm FD-SOI CMOS process, providing

a tunable matching network. The fine and continuous tuning was tested along ±20 % of the nominal currents with results as expected from the perfect active resonator model and, when it was necessary, from the complete active resonator model. It is shown that the model results are still valid in this complete design that incorporates the LNA core transistor and real current sources.

This LNA example was a proof of concept, in which the consistency and accuracy of the model and their subsequent results were tested in a more real environment. That was the focus and in that context the results were highly satisfactory. The noise figure was a quite good result; the noise contribution of the active resonator represents 26 % of the total generated noise. A final LNA design should have a higher gain to compensate the resulting noise figure. The designed active resonator generates, at the end of the design (considering also its real current sources), less noise than its passive counterpart. Linearity (IIP3) must be improved to fulfil many application scenarios, what would require continue the work on modifications of the circuit started in Section 4.5.

Although active inductors were reported since the mid-20th century, they are still a fertile field for research, in particular, in gigahertz radio frequency applications. The model developed in this work, together with the power of the new nanometre scale technologies, allows the development of more complex active resonator architectures that could better deal with the constraints given by noise, power consumption, linearity and quality factor.

6.2 Future work

The LNA example design could be improved to further take into advantage the features of the designed low noise active resonator. It will be interesting, also, to design the layout, manufacture the chip and measure the *real* performance. Other LNA examples with different architectures can also be designed and other integrated active inductor applications can be explored.

The *perfect active resonator model* is an interesting result for a first design and gives very simple relations between the fundamental parameters. On the other hand, the *complete active resonator model* gives very accurate results but is not as simple to understand. In fact, there are relations in which the new parameters (ω_Δ and ω_Π) can be neglected while sometimes they are important. This suggests that the model could be simplified without accuracy loss. This simplification and formalization of the *complete active resonator model* could be an interesting work.

Continuing with the works around the *complete active resonator model*, the use of a more complex architecture (i.e. with differential transconductors) could better deal with the adjustment of the several parameters independently, for example, modifying the transcapacitances to explore the case in which $\omega_x^2 < 0$. On the same way, the use of active resonators in a differential amplifier can take advantage of the availability of the opposite signal, i.e. in the design of an active resonator for a differential amplifier, the signals v_a, v_b, $-v_a$ and $-v_b$ are available.

The new proposed architectures, LI-SGAI and HI-SGAI, needs more exhaustive analysis and testing. LI-SGAI is a very simple design, like SGAI and BFAI. Those three needs to be compared not only in the x value, but also their transcapacitive terms which was proved their relevance in the active resonator performance.

The active resonator linearity could be modelled in a more formal approach, the work of Jespers and Murmann [34] could be a good starting point. Linearity improvement could be realized placing a source resistance (as was done in this work) but there are, also, other strategies that could be explored to linearize the transconductances.

Finally, the tunability is one of the main reasons to apply active inductors and its limits should be further explored.

This page was intentionally left blank.

Apendix A

Annex to Chapter 4

A.1 Applying the model

When trying to apply the model developed in Chapter 3 to some practical circuits such as those shown in Figure A.1, the small-signal model cannot be exactly adapted to the topology shown in Figure 3.2a. However, as it will be shown in this section, the small signal model could be adapted to the topology shown in Figure A.2a which has some relationship with the model of Figure A.2b (and, therefore, with the model of Figure 3.2a).

A.1.1 Matrix decomposition

The schematic of Figure A.2b can be drawn as that shown in Figure A.3a. To find the admittance matrix representation, the circuit can be thought as the superposition of those shown in Figure A.3b and A.3c. Their admittance matrix are

$$[Y_{gyr}] = \begin{pmatrix} 0 & g_{ma} \\ -g_{mb} & 0 \end{pmatrix} \quad \text{and} \quad [Y_{ZaZb}] = \begin{pmatrix} \frac{1}{Z_a} & 0 \\ 0 & \frac{1}{Z_b} \end{pmatrix} \tag{A.1}$$

respectively. Then, the admittance matrix of the circuit in Figure A.3a becomes

$$[Y_m] = [Y_{gyr}] + [Y_{ZaZb}] = \begin{pmatrix} \frac{1}{Z_a} & g_{ma} \\ -g_{mb} & \frac{1}{Z_b} \end{pmatrix} \tag{A.2}$$

Next, it can be done the same for the circuit of Figure A.2a; it can be written as shown in Figure A.4a and its admittance matrix can be easily calculated if the circuit is viewed as a superposition of the quadripoles of Figures A.4b, A.4c and A.4d. Their admittance matrix are

$$[\tilde{Y}_{gyr}] = \begin{pmatrix} -k_a\tilde{g}_{mb} & \tilde{g}_{ma} \\ -\tilde{g}_{mb} & k_b\tilde{g}_{mb} \end{pmatrix}, \tag{A.3a}$$

$$[\tilde{Y}_{Zab}] = \begin{pmatrix} \frac{1}{\tilde{Z}_{ab}} & -\frac{1}{\tilde{Z}_{ab}} \\ -\frac{1}{\tilde{Z}_{ab}} & \frac{1}{\tilde{Z}_{ab}} \end{pmatrix} \quad \text{and} \tag{A.3b}$$

$$[\tilde{Y}_{ZaZb}] = \begin{pmatrix} \frac{1}{\tilde{Z}_a} & 0 \\ 0 & \frac{1}{\tilde{Z}_b} \end{pmatrix} \tag{A.3c}$$

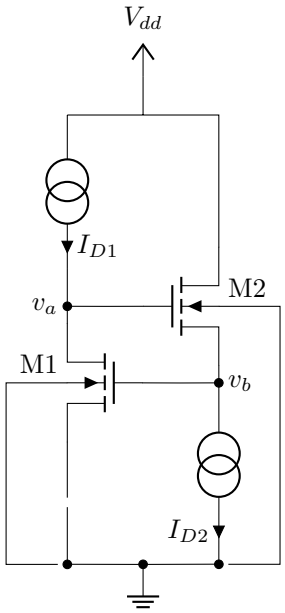

(a) Simple grounded active inductor proposed in Ismail et al. [18].

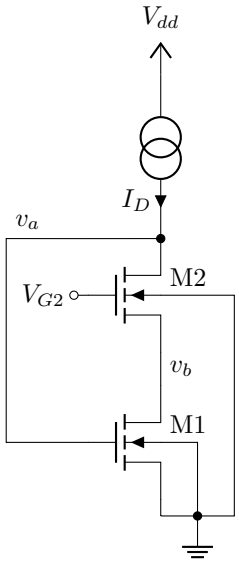

(b) Basic flipped-active inductor proposed in Yue Wu et al. [19].

Figure A.1: Practical implementations examples of active inductors.

respectively[1]. Then, the admittance matrix of the circuit of Figure A.4a becomes

$$[\tilde{Y}_m] = [\tilde{Y}_{gyr}] + [\tilde{Y}_{Zab}] + [\tilde{Y}_{ZaZb}] = \begin{pmatrix} \frac{1}{\tilde{Z}_a} + \frac{1}{\tilde{Z}_{ab}} - k_a\tilde{g}_{ma} & -\frac{1}{\tilde{Z}_{ab}} + \tilde{G}_{ab} \\ -\frac{1}{\tilde{Z}_{ab}} - \tilde{g}_{mb} & \frac{1}{\tilde{Z}_b} + \frac{1}{\tilde{Z}_{ab}} + k_b\tilde{g}_{mb} \end{pmatrix} \quad \text{(A.4)}$$

Then, from equations A.2 and A.4 it follows that circuits from Figures A.2a and A.2b are equivalents when

$$[Y_m] = [\tilde{Y}_m] \Longrightarrow \begin{cases} Z_a = \tilde{Z}_a || \tilde{Z}_{ab} || - \dfrac{1}{k_a\tilde{g}_{ma}} \\ Z_b = \tilde{Z}_b || \tilde{Z}_{ab} || \dfrac{1}{k_b\tilde{g}_{ma}} \\ g_{ma} = \tilde{g}_{ma} - \dfrac{1}{\tilde{Z}_{ab}} \\ g_{mb} = \tilde{g}_{mb} + \dfrac{1}{\tilde{Z}_{ab}} \end{cases} \quad \text{(A.5)}$$

With the above relationships, the model developed in Section 2.2 can be applied to more general topologies as ones shown in Figure A.2a.

[1]The matrix $\tilde{Y}_{Zab}$ is not reversible; impedance matrix does not exist because it corresponds to a degenerated quadripole. Care must be taken when using this result.

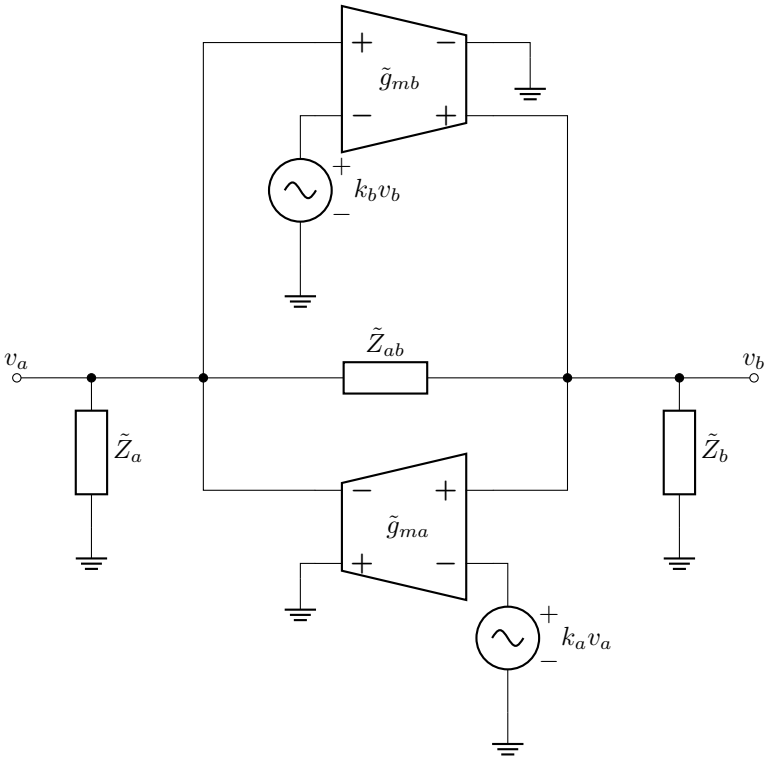

(a) Generic small-signal model of practical active inductor implementations.

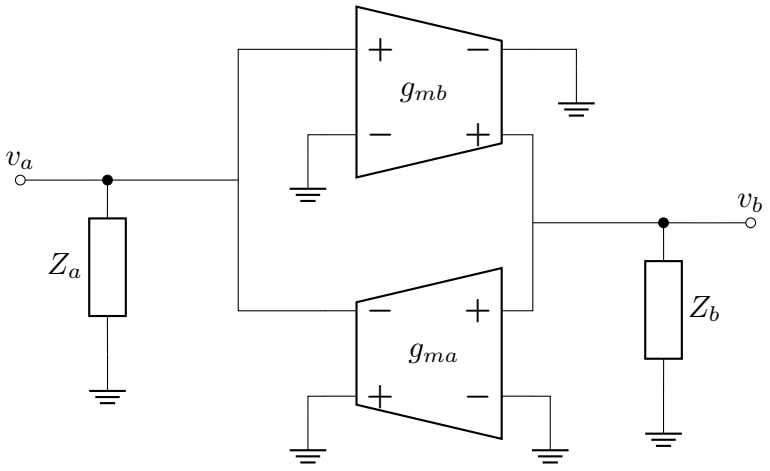

(b) Generic notation for model developed on Section 2.2.

Figure A.2: .

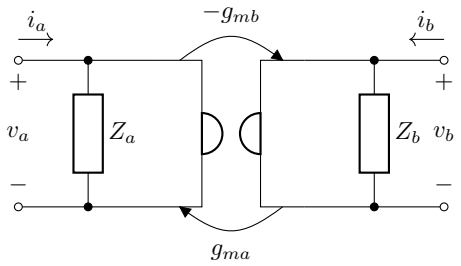

(a) Quadripole Y_m, represents the model developed in Chapter 3.

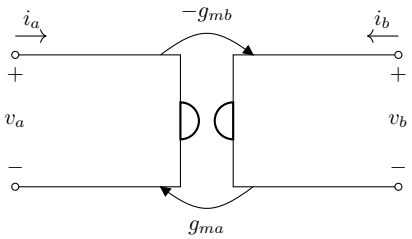

(b) Quadripole Y_{gyr}.

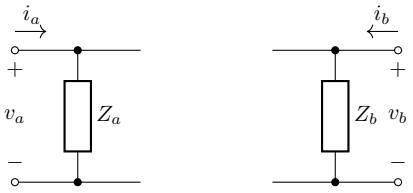

(c) Quadripole Y_{ZaZb}.

Figure A.3: Decomposition of the general model in parallelized quadripoles.

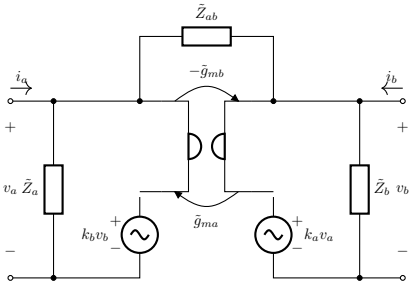

(a) Quadripole $\tilde{Y}_m$ represents the small signal model of practical active inductor implementations.

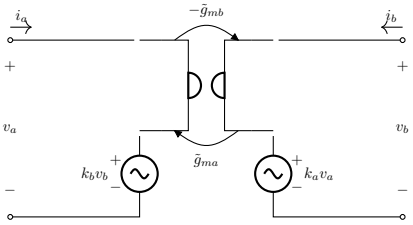

(b) Quadripole $\tilde{Y}_{gyr}$.

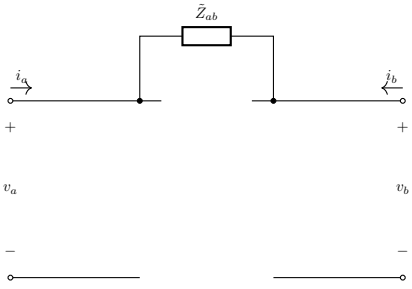

(c) Quadripole $\tilde{Y}_{Zab}$.

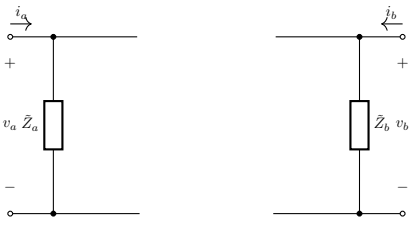

(d) Quadripole $\tilde{Y}_{ZaZb}$.

Figure A.4: Decomposition of the small signal model in parallelized quadripoles.

A.2 Look-up tables

The design methodology in this work was partially based in the use of characteristics of the process collected in Look-up Tables.

Look-up Tables (LUT) are 5 dimension data collection taken from systematized Spectre simulations. The dimensions are length (L), drain-source voltage (V_{ds}), g_m/I_D ratio, width (W) and bias back-plane voltage (V_{bp}). The data collected and used here were gate-source voltage (V_{gs}), the drain current over the aspect ratio ($I_D/(W/L)$), the drain-source saturation voltage (V_{dssat}) and the output conductance over the drain current ratio (g_{ds}/I_D). In all cases, the source is connected to ground.

At the design start, the transistors' width of the LUTs data is selected (for example 10 μm results in a good choice in this work), and, in general, also the bias back-plane voltage (V_{bp}) is selected for all transistors (although in some cases it becomes an interesting variable to sweep). Then, in the LUTs, remains 3 dimension data which allows to perform several sweeps and find the operating points of the designs.

The Look-up Tables turned out to be a powerful tool to find the operating point of a certain circuit, for example, to find the gate bias voltage of transistor M2 in the basic flipped active inductor (BFAI) architecture.

In addition to LUTs, some automated simulations in Spectre were used, e.g. to extract the two-port network parameters of the architecture in order to tune the design.

This page was intentionally left blank.

Apendix B

Equation Proofs

B.1 Proofs of Chapter 3

Equation 3.6:

$$\begin{aligned}
Z_L &= R_a||(R_s + j\omega L_s) \\
&= \frac{1}{\frac{1}{R_a} + \frac{1}{R_s + j\omega L_s}} \\
&= \frac{1}{\frac{1}{R_a} + \frac{1}{\frac{1}{R_b g_{ma} g_{mb}} + \frac{j\omega C_b}{g_{ma} g_{mb}}}} \\
&= \frac{1}{\frac{1}{R_a} + \frac{R_b g_{ma} g_{mb}}{1 + j\omega C_b R_b}} \\
&= \frac{R_a(1 + j\omega C_b R_b)}{1 + j\omega C_b R_b + R_a R_b g_{ma} g_{mb}} \\
&= \frac{R_a\left(1 + \frac{j\omega}{\omega_b}\right)}{x + 1 + \frac{j\omega}{\omega_b}}
\end{aligned}$$

Equation 3.12:

$$\begin{aligned}
Z_v &= Z_L||\frac{1}{j\omega C_a} \\
&= \frac{1}{\frac{1}{Z_L} + j\omega C_a} \\
&= \frac{1}{\frac{1 + x + \frac{j\omega}{\omega_b}}{R_a\left(1 + \frac{j\omega}{\omega_b}\right)} + j\omega C_a} \\
&= \frac{R_a\left(1 + \frac{j\omega}{\omega_b}\right)}{x + 1 + \frac{j\omega}{\omega_b} + j\omega R_a C_a\left(1 + \frac{j\omega}{\omega_b}\right)} \\
&= \frac{R_a\left(1 + \frac{j\omega}{\omega_b}\right)}{\left(1 + \frac{j\omega}{\omega_a}\right)\left(1 + \frac{j\omega}{\omega_b}\right) + x}
\end{aligned}$$

Apendix B. Equation Proofs

Equation 3.14:

$$\begin{aligned}
\operatorname{Im}\{Z_v\} = 0 &\iff \operatorname{Im}\left\{\frac{1}{Z_v}\right\} = 0 \\
&\iff \operatorname{Im}\left\{\frac{\left(1+\frac{j\omega}{\omega_a}\right)\left(1+\frac{j\omega}{\omega_b}\right)+x}{R_a\left(1+\frac{j\omega}{\omega_b}\right)}\right\} \\
&\iff \operatorname{Im}\left\{\left(1+\frac{j\omega}{\omega_a}\right)\left(1+\frac{\omega^2}{\omega_b^2}\right)+x\left(1-\frac{j\omega}{\omega_b}\right)\right\} = 0 \\
&\iff \frac{\omega}{\omega_a}+\frac{\omega^3}{\omega_a\omega_b^2}-x\frac{\omega}{\omega_b} = 0 \\
&\iff \omega^2 = x\omega_a\omega_b - \omega_b^2
\end{aligned}$$

Equation 3.18:

$$\omega_0^2 = x\omega_a\omega_b - \omega_b^2 \Longrightarrow \omega_a = \frac{\omega_0^2+\omega_b^2}{x\omega_b}$$

$$\begin{aligned}
R_v &= Z_v(\omega=\omega_0) \\
&= \left[\frac{R_a\left(1+\frac{j\omega}{\omega_b}\right)}{\left(1+\frac{j\omega}{\omega_a}\right)\left(1+\frac{j\omega_0}{\omega_b}\right)+x}\right]_{\omega=\omega_0} \\
&= \frac{R_a\left(1+\frac{j\omega_0}{\omega_b}\right)}{\left(1+\frac{j\omega_0}{\omega_a}\right)\left(1+\frac{j\omega_0}{\omega_b}\right)+x} \\
&= \frac{R_a\left(1+\frac{j\omega_0}{\omega_b}\right)}{\left[1+\frac{j\omega_0}{\left(\frac{\omega_0^2+\omega_b^2}{x\omega_b}\right)}\right]\left(1+\frac{j\omega_0}{\omega_b}\right)+x} \\
&= \frac{R_a\left(1+\frac{\omega_0^2}{\omega_b^2}\right)}{\left[1+\frac{j\omega_0}{\left(\frac{\omega_0^2+\omega_b^2}{x\omega_b}\right)}\right]\left(1+\frac{\omega_0^2}{\omega_b^2}\right)+x\left(1-\frac{j\omega_0}{\omega_b}\right)} \\
&= \frac{R_a\left(1+\frac{\omega_0^2}{\omega_b^2}\right)}{x+1+\frac{\omega_0^2}{\omega_b^2}+j\left[\frac{x\omega_0\omega_b}{\omega_0^2+\omega_b^2}\left(1+\frac{\omega_0^2}{\omega_b^2}\right)-x\frac{\omega_0}{\omega_b}\right]} \\
&= \frac{R_a\left(1+\frac{\omega_0^2}{\omega_b^2}\right)}{x+1+\frac{\omega_0^2}{\omega_b^2}+j\left[\frac{x\omega_0\omega_b}{\omega_0^2+\omega_b^2}\left(\frac{\omega_b^2+\omega_0^2}{\omega_b^2}\right)-x\frac{\omega_0}{\omega_b}\right]} \\
&= \frac{R_a\left(1+\frac{\omega_0^2}{\omega_b^2}\right)}{x+1+\frac{\omega_0^2}{\omega_b^2}}
\end{aligned}$$

Equation 3.23:

$$\begin{aligned}
\frac{\partial Q}{\partial \omega_b} = 0 &\Longleftrightarrow \frac{\partial}{\partial \omega_b}\frac{x\omega_b\omega_0}{\omega_0^2+\omega_b^2(x+1)} = 0 \\
&\Longleftrightarrow \frac{x\omega_0[\omega_0^2+\omega_b^2(x+1)] - 2\omega_b(x+1)x\omega_b\omega_0}{[\omega_0^2+\omega_b^2(x+1)]^2} = 0 \\
&\Longleftrightarrow \omega_0^2+\omega_b^2(x+1) = 2\omega_b^2(x+1) \\
&\Longleftrightarrow \omega_0^2 = \omega_b^2(x+1)
\end{aligned}$$

Equation 3.35:

$$\begin{aligned}
\frac{S_n}{S_{n0}} &= I_n^2(f)\frac{R_v}{4k_BT} \\
&= \left[V_{na}^2 g_{ma}^2 g_{mb}^2 \frac{R_b^2}{1+\frac{\omega^2}{\omega_b^2}} + V_{nb}^2 g_{ma}^2\right]\frac{R_v}{4k_BT} \\
&= \left[V_{na}^2 g_{ma}^2 g_{mb}^2 \frac{R_b^2}{1+\frac{\omega^2}{\omega_b^2}} + V_{nb}^2 g_{ma}^2\right]\frac{1}{4k_BT}\frac{R_a\left(1+\frac{\omega_0^2}{\omega_b^2}\right)}{x+1+\frac{\omega_0^2}{\omega_b^2}} \\
&= \frac{n}{2}\left(\frac{1}{g_{mb}} g_{ma}^2 g_{mb}^2 \frac{R_b^2}{1+\frac{\omega^2}{\omega_b^2}} + \frac{1}{g_{ma}} g_{ma}^2\right)\frac{R_a\left(1+\frac{\omega_0^2}{\omega_b^2}\right)}{x+1+\frac{\omega_0^2}{\omega_b^2}} \\
&= \frac{n}{2}\left[g_{ma}^2 g_{mb} R_a R_b^2 + g_{ma} R_a\left(1+\frac{\omega_0^2}{\omega_b^2}\right)\right]\frac{1}{x+1+\frac{\omega_0^2}{\omega_b^2}} \\
&= \frac{n}{2}\left[g_{ma} R_b x + g_{ma} R_a\left(1+\frac{\omega_0^2}{\omega_b^2}\right)\right]\frac{1}{x+1+\frac{\omega_0^2}{\omega_b^2}} \\
&= \frac{n}{2} g_{ma} R_a \frac{\frac{R_b}{R_a}x+1+\frac{\omega_0^2}{\omega_b^2}}{x+1+\frac{\omega_0^2}{\omega_b^2}}
\end{aligned}$$

Equation 3.37:

$$\begin{aligned}
\frac{\hat{S}_n}{S_{n0}} &\equiv \frac{S_n}{S_{n0}}\frac{1}{Q} \\
&= \frac{n}{2} g_{ma} R_a \frac{\frac{R_b}{R_a}x+1+\frac{\omega_0^2}{\omega_b^2}}{x+1+\frac{\omega_0^2}{\omega_b^2}}\left[\frac{x\omega_b\omega_0}{\omega_0^2+\omega_b^2(x+1)}\right]^{-1} \\
&= \frac{n}{2} g_{ma} R_a \frac{\frac{R_b}{R_a}x+1+\frac{\omega_0^2}{\omega_b^2}}{x+1+\frac{\omega_0^2}{\omega_b^2}}\frac{x+1+\frac{\omega_0^2}{\omega_b^2}}{x\frac{\omega_0}{\omega_b}} \\
&= \frac{n}{2} g_{ma} R_a \frac{\frac{R_b}{R_a}x+1+\frac{\omega_0^2}{\omega_b^2}}{x\frac{\omega_0}{\omega_b}}
\end{aligned}$$

Equation 3.38:

$$\begin{aligned}
\frac{\partial}{\partial\omega_0}\frac{\hat{S}_n}{S_{n0}} = 0 &\iff \frac{\partial}{\partial\omega_0}\frac{n}{2}g_{ma}R_a\frac{\frac{R_b}{R_a}x+1+\frac{\omega_0^2}{\omega_b^2}}{x\frac{\omega_0}{\omega_b}} = 0 \\
&\iff \frac{\frac{2\omega_0}{\omega_b}x\frac{\omega_0}{\omega_b} - \frac{x}{\omega_b}\left(\frac{Rb}{R_a}x+1+\frac{\omega_0^2}{\omega_b^2}\right)}{x^2\frac{\omega_0^2}{\omega_b^2}} = 0 \\
&\iff \frac{\omega_0^2 x}{\omega_b^3} = \frac{x^2}{\omega_b}\frac{R_b}{R_a}+\frac{x}{\omega_b} \\
&\iff \omega_{\min}^2 = \left(x\frac{R_b}{R_a}+1\right)\omega_b^2
\end{aligned}$$

Equation 3.39:

$$\begin{aligned}
\left.\frac{\hat{S}_n}{S_{n0}}\right|_{\omega=\omega_{\min}} &= \frac{n}{2}g_{ma}R_a\frac{\frac{R_b}{R_a}x+1+\frac{R_b}{R_a}x+1}{x\sqrt{x\frac{R_b}{R_a}+1}} \\
&= n\frac{g_{ma}R_a}{x}\sqrt{\frac{R_b}{R_a}x+1} \\
&= ng_{ma}\sqrt{\frac{R_aR_b}{x}+\frac{R_a^2}{x^2}}
\end{aligned}$$

B.2 Proofs of Chapter 4

Equation 4.19:

$$\begin{aligned}
\frac{1}{Z_v(j\omega)} &= y_{aa} - \frac{y_{ab}y_{ba}}{y_{bb}} \\
&= \frac{1}{R_a}\left(1+j\frac{\omega}{\omega_a}\right) + \frac{g_{ma}\left(1-j\frac{\omega}{\omega_{ab}}\right)g_{mb}\left(1+j\frac{\omega}{\omega_{ba}}\right)}{\frac{1}{R_b}\left(1+j\frac{\omega}{\omega_b}\right)} \\
&= \frac{1}{R_a}\left[1+j\frac{\omega}{\omega_a}+\frac{x}{1+\frac{\omega^2}{\omega_b^2}}\left(1-j\frac{\omega}{\omega_{ab}}+j\frac{\omega}{\omega_{ba}}+\frac{\omega^2}{\omega_{ab}\omega_{ba}}\right)\left(1-j\frac{\omega}{\omega_b}\right)\right] \\
&= \frac{1}{R_a}\left[1+j\frac{\omega}{\omega_a}+\frac{x}{1+\frac{\omega^2}{\omega_b^2}}\left(1+\frac{\omega^2}{\omega_{ab}\omega_{ba}}-\frac{\omega^2}{\omega_b\omega_{ab}}+\frac{\omega^2}{\omega_b\omega_{ba}}-j\frac{\omega}{\omega_b}-j\frac{\omega}{\omega_{ab}}+j\frac{\omega}{\omega_{ba}}-j\frac{\omega^3}{\omega_b\omega_{ab}\omega_{ba}}\right)\right] \\
&= G + jB
\end{aligned}$$

where

$$\begin{cases}
G = \frac{1}{R_a}\left[1+\frac{x}{1+\frac{\omega^2}{\omega_b^2}}\left(1+\frac{\omega^2}{\omega_{ab}\omega ba}+\frac{\omega^2}{\omega_b\omega_{ba}}-\frac{\omega^2}{\omega_b\omega_{ab}}\right)\right] \\
B = \frac{1}{R_a}\left[\frac{\omega}{\omega_a}-\frac{x}{1+\frac{\omega^2}{\omega_b^2}}\left(\frac{\omega}{\omega_b}+\frac{\omega}{\omega_{ab}}-\frac{\omega}{\omega_{ba}}+\frac{\omega^3}{\omega_b\omega_{ab}\omega_{ba}}\right)\right]
\end{cases}$$

Apendix C

Simulation details

C.1 Simulations of Chapter 4

Simulation C.1: SGAI architecture using the perfect active resonator model.

Input parameters:

$L_1 = 100\ nm$	$L_2 = 100\ nm$	$I_{D1} = 500\ \mu A$
$(g_m/I_D)_1 = 16\ V^{-1}$	$(g_m/I_D)_2 = 15\ V^{-1}$	$I_{D2} = 500\ \mu A$
$W_1 = 23.072\ \mu m$	$W_2 = 19.158\ \mu m$	$fingerWidth = 206\ nm$

NMOS bias back-plane voltage: 2 V

Sweep (seen from port 1):

ω_0/ω_b	ω_0/ω_a	$C_{ae}\ (fF)$	$C_{be}\ (pF)$	$f_0\ (GHz)$	$R_v\ (k\Omega)$	Q	S_n/S_{n0}
4	25.9	85.51	2.14	2.399	2.14	3.85	10
5	20.7	60.75	2.69	2.402	3.13	4.56	15
6	17.2	44.29	3.23	2.403	4.19	5.12	20
7	14.8	32.55	3.78	2.404	5.25	5.52	25
8	12.9	23.75	4.33	2.404	6.27	5.78	29
9	11.5	16.92	4.88	2.405	7.22	5.92	34
10	10.3	11.45	5.42	2.405	8.09	5.98	38
11	9.4	6.98	5.97	2.405	8.86	5.96	41
12	8.6	3.26	6.52	2.405	9.54	5.88	45
13	7.9	0.12	7.06	2.405	10.13	5.77	47

Sweep (seen from port 2):

ω_0/ω_b	ω_0/ω_a	$C_{ae}\ (pF)$	$C_{be}\ (fF)$	$f_0\ (GHz)$	$R_v\ (\Omega)$	Q	S_n/S_{n0}
8	12.9	7.02	0.41	2.403	54.60	5.78	43
9	11.5	6.23	5.16	2.404	62.85	5.93	40
10	10.3	5.60	9.91	2.405	70.34	5.98	36
11	9.4	5.09	14.65	2.406	77.03	5.96	33
12	8.6	4.66	19.40	2.406	82.94	5.88	30
13	7.9	4.29	24.15	2.407	88.12	5.77	27
14	7.4	3.98	28.90	2.407	92.62	5.63	25
15	6.9	3.71	33.64	2.407	96.53	5.48	22
16	6.4	3.48	38.39	2.407	99.93	5.32	20
17	6.1	3.27	43.14	2.408	102.87	5.16	19
18	5.7	3.09	47.88	2.408	105.41	4.99	17

Simulation C.2: BFAI architecture using the perfect active resonator model.

Input parameters:

$L_1 = 100\ nm$	$L_2 = 100\ nm$	$I_{D1} = 909\ \mu A$
$(g_m/I_D)_1 = 10\ V^{-1}$	$(g_m/I_D)_2 = 10\ V^{-1}$	$I_{D2} = 90.9\ \mu A$
$W_1 = 16.686\ \mu m$	$W_2 = 1.648\ \mu m$	$fingerWidth = 206\ nm$

NMOS bias back-plane voltage: 2 V

Sweep (seen from port 1):

ω_0/ω_b	ω_0/ω_a	$C_{ae}\ (fF)$	$C_{be}\ (pF)$	$f_0\ (GHz)$	$R_v\ (k\Omega)$	Q	S_n/S_{n0}
1	48.6	240.44	0.14	2.107	0.33	0.68	2
2	24.9	110.21	0.29	2.413	0.91	1.69	5
3	16.7	65.29	0.44	2.431	1.71	2.28	10
4	12.6	42.55	0.59	2.431	2.59	2.67	15
5	10.1	28.81	0.74	2.431	3.48	2.90	20
6	8.4	19.62	0.89	2.428	4.31	3.02	24
7	7.2	13.03	1.04	2.428	5.07	3.06	29
8	6.3	8.08	1.19	2.426	5.75	3.04	32
9	5.6	4.22	1.35	2.425	6.34	2.99	36
10	5.1	1.13	1.50	2.424	6.86	2.92	39

Sweep (seen from port 2):

ω_0/ω_b	ω_0/ω_a	$C_{ae}\ (pF)$	$C_{be}\ (fF)$	$f_0\ (GHz)$	$R_v\ (\Omega)$	Q	S_n/S_{n0}
5	10.1	1.51	0.69	2.428	127	2.90	45
6	8.4	1.26	6.20	2.427	157	3.02	40
7	7.2	1.08	11.70	2.428	185	3.06	36
8	6.3	0.94	17.20	2.427	210	3.04	32
9	5.6	0.84	22.70	2.426	232	2.99	28
10	5.1	0.75	28.20	2.427	251	2.92	25
11	4.6	0.68	33.71	2.425	267	2.83	23
12	4.2	0.63	39.21	2.425	282	2.74	21
13	3.9	0.58	44.71	2.425	295	2.64	19
14	3.6	0.54	50.21	2.425	306	2.55	18

Simulation C.3: Tuning BFAI architecture.

Input parameters:

$L_1 = 100\ nm$	$L_2 = 100\ nm$	$I_{D1} = 625\ \mu A$
$(g_m/I_D)_1 = 16\ V^{-1}$	$(g_m/I_D)_2 = 15\ V^{-1}$	$I_{D2} = 375\ \mu A$
$W_1 = 28.84\ \mu m$	$W_2 = 14.214\ \mu m$	$fingerWidth = 206\ nm$

NMOS bias back-plane voltage: 2 V

Simulation C.4: Tuning SGAI architecture.

Input parameters:

$L_1 = 100\ nm$	$L_2 = 100\ nm$	$I_{D1} = 833\ \mu A$
$(g_m/I_D)_1 = 10\ V^{-1}$	$(g_m/I_D)_2 = 10\ V^{-1}$	$I_{D2} = 167\ \mu A$
$W_1 = 15.244\ \mu m$	$W_2 = 3.09\ \mu m$	$fingerWidth = 206\ nm$

NMOS bias back-plane voltage: 2 V

Simulation C.5: SGAI architecture varying the I_{D2}/I_{D1} ratio.

Input parameters:

$L_1 = 100\ nm$ $\quad$ $L_2 = 100\ nm$

$(g_m/I_D)_1 = 23.5\ V^{-1}$ $\quad$ $(g_m/I_D)_2 = 10\ V^{-1}$

$I_{Dtot} = 1\ mA$ $\quad$ $fingerWidth = 206\ nm$

NMOS bias back-plane voltage: 2 V

Sweep parameters:

I_{D2}/I_{D1}	I_{D1} (μA)	I_{D2} (μA)	W_1 (μm)	W_2 (μm)
$10^{-1.6}$	975	25	182.34	0.359
$10^{-1.4}$	962	38	179.76	0.561
$10^{-1.2}$	941	59	175.83	0.869
$10^{-1.0}$	909	91	169.93	1.332
$10^{-0.8}$	863	137	161.35	2.004
$10^{-0.6}$	799	201	149.39	2.941
$10^{-0.4}$	715	285	133.69	4.171
$10^{-0.2}$	613	387	114.61	5.667
$10^{0.0}$	500	500	93.46	7.324
$10^{0.2}$	387	613	72.31	8.981

Sweep, seen from port 1:

I_{D2}/I_{D1}	C_{ae} (pF)	C_{be} (fF)	f_0 (GHz)	R_v (Ω)	Q	S_n/S_{n0}
$10^{-1.6}$	31.3	8	2.57	0.19	0.32	3.7
$10^{-1.4}$	31.6	125	2.51	0.29	0.50	4.6
$10^{-1.2}$	30.4	275	2.51	0.43	0.73	5.9
$10^{-1.0}$	29.3	526	2.45	0.65	1.09	7.9
$10^{-0.8}$	27.3	948	2.45	1.04	1.69	10.9
$10^{-0.6}$	23.8	1454	2.45	1.55	2.35	14.4
$10^{-0.4}$	19.2	2154	2.45	2.33	3.20	18.8
$10^{-0.2}$	13.5	3040	2.45	3.52	4.15	23.8
$10^{0.0}$	7.3	3970	2.40	5.28	5.00	28.9
$10^{0.2}$	1.0	4890	2.40	8.12	5.96	34.1

Sweep, seen from port 2:

I_{D2}/I_{D1}	C_{ae} (pF)	C_{be} (fF)	f_0 (GHz)	R_v (Ω)	Q	S_n/S_{n0}
$10^{-1.6}$	6	32.3	2.57	106	0.32	0.2
$10^{-1.4}$	122	32.5	2.51	106	0.50	0.2
$10^{-1.2}$	271	31.3	2.51	105	0.73	0.3
$10^{-1.0}$	520	30.2	2.45	103	1.09	0.5
$10^{-0.8}$	939	28.2	2.45	100	1.69	0.9
$10^{-0.6}$	1441	24.6	2.45	96	2.35	1.6
$10^{-0.4}$	2136	19.9	2.45	92	3.20	3.3
$10^{-0.2}$	3015	14.1	2.45	86	4.15	6.5
$10^{0.0}$	3938	7.8	2.40	83	5.00	12.4
$10^{0.2}$	4850	1.4	2.40	81	5.96	23.1

Simulation C.6: SGAI architecture showing an operating point in which the PSD of noise generated by the active resonator, at resonance frequency, is less than the generated by its passive counterpart.

Input parameters:

$L_1 = 100\ nm$	$L_2 = 100\ nm$	$I_{D1} = 917\ \mu A$
$(g_m/I_D)_1 = 23.5\ V^{-1}$	$(g_m/I_D)_2 = 10\ V^{-1}$	$I_{D2} = 83\ \mu A$
$W_1 = 171.39\ \mu m$	$W_2 = 1.236\ \mu m$	$fingerWidth = 206\ nm$

NMOS bias back-plane voltage: 2 V

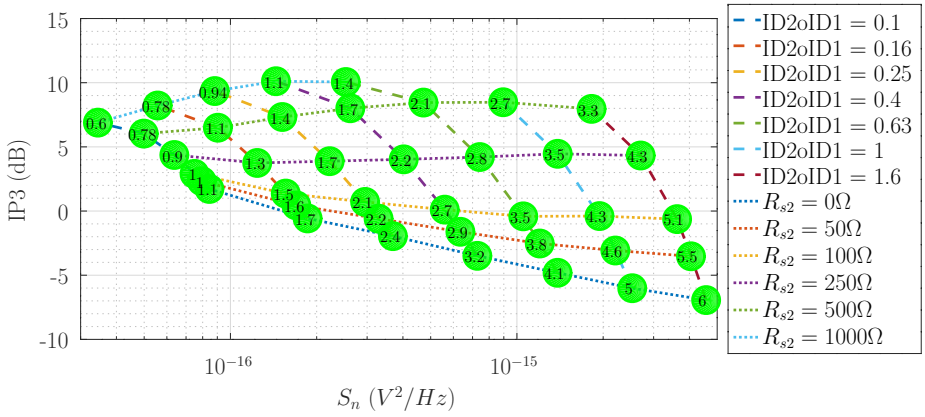

(a)

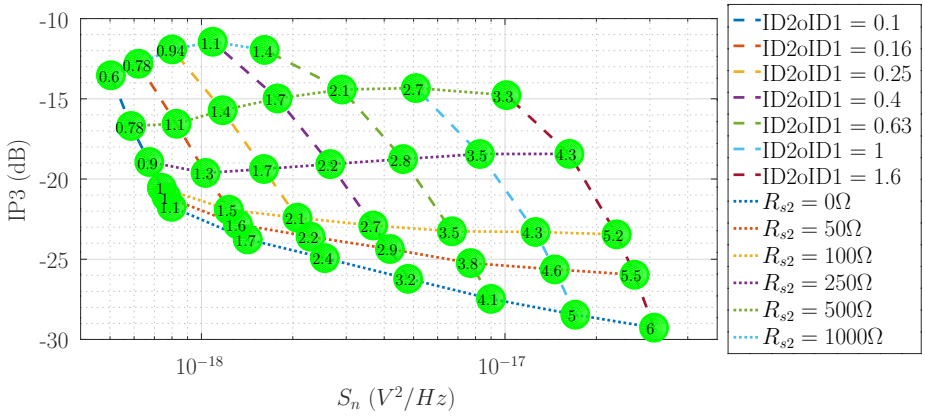

(b)

Figure C.1: Simulation results of the SGAI architecture, varying the value of R_{s2} and the relationship I_{D2}/I_{D1}, with a total current of 1 mA, resonance frequency of about 2.4 GHz and $(g_m/I_D) = 10\ V^{-1}$ for both transistors. More details in Simulation C.7.

Simulation C.7: .

Input parameters:

$L_1 = 100\ nm$ $L_2 = 100\ nm$ $I_{Dtot} = 1\ mA$

$(g_m/I_D)_1 = 23.5\ V^{-1}$ $(g_m/I_D)_2 = 10\ V^{-1}$ $fingerWidth = 206\ nm$

NMOS bias back-plane voltage: 2 V

Sweep general parameters:

$R_s(\Omega)$	I_{D2}/I_{D1}	$I_{D1}\ (\mu A)$	$I_{D2}\ (\mu A)$	$W_1\ (\mu m)$	$W_2\ (\mu m)$
0	$10^{-1.0}$	909	91	169.95	1.236
50	$10^{-1.0}$	909	91	169.95	1.236
100	$10^{-1.0}$	909	91	169.95	1.236
250	$10^{-1.0}$	909	91	169.95	1.236
500	$10^{-1.0}$	909	91	169.95	1.236
1000	$10^{-1.0}$	909	91	169.95	1.236
0	$10^{-0.8}$	863	137	161.30	2.060
50	$10^{-0.8}$	863	137	161.30	2.060
100	$10^{-0.8}$	863	137	161.30	2.060
250	$10^{-0.8}$	863	137	161.30	2.060
500	$10^{-0.8}$	863	137	161.30	2.060
1000	$10^{-0.8}$	863	137	161.30	2.060
0	$10^{-0.6}$	799	201	149.35	2.884
50	$10^{-0.6}$	799	201	149.35	2.884
100	$10^{-0.6}$	799	201	149.35	2.884
250	$10^{-0.6}$	799	201	149.35	2.884
500	$10^{-0.6}$	799	201	149.35	2.884
1000	$10^{-0.6}$	799	201	149.35	2.884
0	$10^{-0.4}$	715	285	133.69	4.120
50	$10^{-0.4}$	715	285	133.69	4.120
100	$10^{-0.4}$	715	285	133.69	4.120
250	$10^{-0.4}$	715	285	133.69	4.120
500	$10^{-0.4}$	715	285	133.69	4.120
1000	$10^{-0.4}$	715	285	133.69	4.120
0	$10^{-0.2}$	613	387	114.54	5.768
50	$10^{-0.2}$	613	387	114.54	5.768
100	$10^{-0.2}$	613	387	114.54	5.768
250	$10^{-0.2}$	613	387	114.54	5.768
500	$10^{-0.2}$	613	387	114.54	5.768
1000	$10^{-0.2}$	613	387	114.54	5.768
0	$10^{0.0}$	500	500	93.52	7.416
50	$10^{0.0}$	500	500	93.52	7.416
100	$10^{0.0}$	500	500	93.52	7.416
250	$10^{0.0}$	500	500	93.52	7.416
500	$10^{0.0}$	500	500	93.52	7.416
0	$10^{0.2}$	387	613	72.31	9.064
50	$10^{0.2}$	387	613	72.31	9.064
100	$10^{0.2}$	387	613	72.31	9.064
250	$10^{0.2}$	387	613	72.31	9.064
500	$10^{0.2}$	387	613	72.31	9.064

Sweep seen from port 1:

$R_s(\Omega)$	I_{D2}/I_{D1}	C_{ae} (fF)	C_{be} (fF)	f_0 (GHz)	R_v (Ω)	Q	V_n (aV^2/Hz)
0	$10^{-1.0}$	29.3	526	2.45	652.40	1.09	84
50	$10^{-1.0}$	29.0	494	2.45	628.92	1.05	79
100	$10^{-1.0}$	28.8	466	2.45	607.33	1.01	75
250	$10^{-1.0}$	28.1	393	2.45	550.49	0.90	64
500	$10^{-1.0}$	27.3	303	2.51	477.54	0.78	50
1000	$10^{-1.0}$	25.5	189	2.51	379.55	0.60	34
0	$10^{-0.8}$	27.3	948	2.45	1035.16	1.69	186
50	$10^{-0.8}$	27.1	872	2.45	983.37	1.59	170
100	$10^{-0.8}$	27.0	805	2.45	936.52	1.51	156
250	$10^{-0.8}$	26.0	650	2.45	820.60	1.30	124
500	$10^{-0.8}$	25.0	480	2.45	682.28	1.06	90
1000	$10^{-0.8}$	22.7	293	2.51	514.98	0.78	56
0	$10^{-0.6}$	23.8	1454	2.45	1548.45	2.35	369
50	$10^{-0.6}$	23.6	1301	2.45	1453.12	2.19	329
100	$10^{-0.6}$	23.4	1175	2.45	1368.53	2.05	295
250	$10^{-0.6}$	22.6	904	2.45	1167.40	1.72	222
500	$10^{-0.6}$	21.5	641	2.45	941.31	1.35	152
1000	$10^{-0.6}$	18.7	383	2.45	687.70	0.94	88
0	$10^{-0.4}$	19.2	2154	2.45	2333.73	3.20	728
50	$10^{-0.4}$	19.2	1857	2.45	2168.08	2.95	635
100	$10^{-0.4}$	19.0	1630	2.45	2025.09	2.73	560
250	$10^{-0.4}$	18.5	1187	2.45	1691.55	2.24	402
500	$10^{-0.4}$	16.9	805	2.45	1334.64	1.70	262
1000	$10^{-0.4}$	14.0	471	2.45	953.71	1.15	144
0	$10^{-0.2}$	13.5	3040	2.45	3515.24	4.15	1386
50	$10^{-0.2}$	13.8	2504	2.45	3256.80	3.81	1201
100	$10^{-0.2}$	13.8	2128	2.45	3034.38	3.52	1052
250	$10^{-0.2}$	13.4	1465	2.45	2515.63	2.84	742
500	$10^{-0.2}$	12.3	958	2.45	1967.93	2.14	472
1000	$10^{-0.2}$	8.9	552	2.45	1395.61	1.41	253
0	$10^{0.0}$	7.3	3970	2.40	5283.94	5.00	2527
50	$10^{0.0}$	8.2	3124	2.40	4916.61	4.60	2205
100	$10^{0.0}$	8.6	2578	2.40	4595.05	4.26	1942
250	$10^{0.0}$	8.3	1697	2.45	3847.74	3.53	1387
500	$10^{0.0}$	7.1	1083	2.45	3044.43	2.67	895
0	$10^{0.2}$	1.0	4890	2.40	8116.97	5.96	4575
50	$10^{0.2}$	2.6	3684	2.40	7613.18	5.54	4051
100	$10^{0.2}$	3.3	2964	2.40	7178.58	5.15	3623
250	$10^{0.2}$	3.6	1884	2.40	6148.53	4.26	2704
500	$10^{0.2}$	2.7	1184	2.40	4986.46	3.28	1822

Sweep seen from port 2:

R_s (Ω)	I_{D2}/I_{D1}	C_{ae} (fF)	C_{be} (fF)	f_0 (GHz)	R_v (Ω)	Q	V_n (aV^2/Hz)
0	$10^{-1.0}$	520	30.2	2.45	103	1.09	0.80
50	$10^{-1.0}$	489	29.9	2.45	104	1.05	0.77
100	$10^{-1.0}$	461	29.7	2.45	104	1.01	0.74
250	$10^{-1.0}$	388	29.0	2.45	105	0.90	0.67
500	$10^{-1.0}$	299	28.1	2.51	107	0.78	0.59
1000	$10^{-1.0}$	186	26.3	2.51	108	0.60	0.50
0	$10^{-0.8}$	939	28.2	2.45	100	1.69	1.42
50	$10^{-0.8}$	863	27.9	2.45	101	1.59	1.32
100	$10^{-0.8}$	798	27.8	2.45	103	1.51	1.23
250	$10^{-0.8}$	643	26.9	2.45	105	1.30	1.03
500	$10^{-0.8}$	475	25.8	2.45	109	1.06	0.83
1000	$10^{-0.8}$	289	23.5	2.51	111	0.78	0.62
0	$10^{-0.6}$	1441	24.6	2.45	96	2.35	2.55
50	$10^{-0.6}$	1289	24.4	2.45	99	2.19	2.29
100	$10^{-0.6}$	1165	24.2	2.45	102	2.06	2.07
250	$10^{-0.6}$	896	23.3	2.45	107	1.72	1.61
500	$10^{-0.6}$	635	22.2	2.45	112	1.35	1.17
1000	$10^{-0.6}$	379	19.3	2.45	116	0.94	0.80
0	$10^{-0.4}$	2136	19.9	2.45	92	3.20	4.80
50	$10^{-0.4}$	1841	19.9	2.45	97	2.95	4.18
100	$10^{-0.4}$	1616	19.7	2.45	102	2.73	3.68
250	$10^{-0.4}$	1177	19.1	2.45	111	2.24	2.66
500	$10^{-0.4}$	798	17.5	2.45	119	1.70	1.78
1000	$10^{-0.4}$	467	14.6	2.45	125	1.15	1.09
0	$10^{-0.2}$	3015	14.1	2.45	86	4.15	8.99
50	$10^{-0.2}$	2483	14.5	2.45	96	3.81	7.71
100	$10^{-0.2}$	2110	14.4	2.45	103	3.52	6.69
250	$10^{-0.2}$	1453	14.0	2.45	118	2.84	4.61
500	$10^{-0.2}$	950	12.8	2.45	131	2.14	2.90
1000	$10^{-0.2}$	548	9.3	2.45	139	1.41	1.61
0	$10^{0.0}$	3938	7.8	2.40	83	5.00	17.04
50	$10^{0.0}$	3098	8.7	2.40	96	4.60	14.58
100	$10^{0.0}$	2558	9.1	2.40	107	4.27	12.60
250	$10^{0.0}$	1684	8.8	2.45	130	3.53	8.26
500	$10^{0.0}$	1075	7.5	2.45	149	2.67	5.08
0	$10^{0.2}$	4850	1.4	2.40	81	5.96	30.97
50	$10^{0.2}$	3654	3.0	2.40	99	5.54	26.72
100	$10^{0.2}$	2941	3.6	2.40	114	5.15	23.31
250	$10^{0.2}$	1870	3.9	2.40	146	4.26	16.29
500	$10^{0.2}$	1175	3.0	2.40	176	3.28	10.11

Simulation C.8: .

Input parameters:

$L_1 = 100\ nm$ $L_2 = 100\ nm$ $I_{D2}/I_{D1} = 1$

$(g_m/I_D)_1 = 23.5\ V^{-1}$ $(g_m/I_D)_2 = 10\ V^{-1}$ $fingerWidth = 206\ nm$

NMOS bias back-plane voltage: 2 V

Sweep general parameters:

I_{Dtot}	I_{D1} (μA)	I_{D2} (μA)	W_1 (μm)	W_2 (μm)
0.10	50	50	9.35	0.732
0.16	79	79	14.81	1.161
0.25	126	126	23.48	1.840
0.40	199	199	37.21	2.916
0.63	315	315	58.97	4.621
1.00	500	500	93.46	7.324
1.58	792	792	148.12	11.607
2.51	1256	1256	234.76	18.396
3.98	1991	1991	372.07	29.156
6.31	3155	3155	589.69	46.209
10.00	5000	5000	934.60	73.237

Sweep seen from port 1:

I_{Dtot}	C_{ae} (fF)	C_{be} (fF)	f_0 (GHz)	R_v $(k\Omega)$	Q	S_n/S_{n0}
0.10	0.5	416	2.45	54.35	5.19	29.6
0.16	1.0	644	2.44	33.87	5.14	29.3
0.25	1.9	995	2.42	21.11	5.11	28.9
0.40	3.0	1564	2.42	13.30	5.09	28.9
0.63	5.1	2468	2.42	8.37	5.09	28.8
1.00	7.3	3970	2.42	5.31	5.10	29.0
1.58	12.0	6239	2.42	3.35	5.09	28.9
2.51	18.5	9901	2.43	2.11	5.10	29.0
3.98	29.2	15742	2.43	1.33	5.10	29.0
6.31	46.3	24882	2.43	0.84	5.10	29.0
10.00	73.2	39488	2.43	0.53	5.10	29.0

Sweep seen from port 2:

I_{Dtot}	C_{ae} (fF)	C_{be} (fF)	f_0 (GHz)	R_v (Ω)	Q	S_n/S_{n0}
0.10	413	0.6	2.45	800	5.20	13.1
0.16	639	1.1	2.45	513	5.15	12.4
0.25	987	2.0	2.40	332	5.02	12.3
0.40	1551	3.2	2.40	210	4.99	12.2
0.63	2448	5.4	2.40	134	5.03	12.1
1.00	3938	7.8	2.40	83	5.00	12.4
1.58	6187	12.8	2.40	53	5.00	12.3
2.51	9819	19.8	2.40	33	4.98	12.3
3.98	15612	31.3	2.40	21	4.98	12.4
6.31	24678	49.5	2.40	13	4.98	12.3
10.00	39164	78.3	2.40	8	4.98	12.3

Simulation C.9: .

Input parameters:

$L_1 = 100\ nm$ $L_3 = 100\ nm$ $I_{Dtot} = 1\ mA$
$(g_m/I_D)_1 = 10\ V^{-1}$ $(g_m/I_D)_3 = 10\ V^{-1}$ $fingerWidth = 206\ nm$
NMOS bias back-plane voltage: 2 V

Sweep general parameters:

I_{D2}/I_{D1}	$I_{D1}\ (\mu A)$	$I_{D2}\ (\mu A)$	$W_1\ (\mu m)$	$W_2\ (\mu m)$
$10^{-1.0}$	909	91	13.30	4.90
$10^{-0.8}$	863	137	12.63	7.38
$10^{-0.6}$	799	201	11.69	10.82
$10^{-0.4}$	715	285	10.46	15.35
$10^{-0.2}$	613	387	8.97	20.86
$10^{0.0}$	500	500	7.31	26.96
$10^{0.2}$	387	613	5.66	33.05
$10^{0.4}$	285	715	4.16	38.56
$10^{0.6}$	201	799	2.94	43.09

Sweep seen from port 1:

I_{D2}/I_{D1}	$C_{ae}\ (pF)$	$C_{be}\ (fF)$	$f_0\ (GHz)$	$R_v\ (\Omega)$	Q	S_n/S_{n0}
$10^{-1.0}$	1.85	0.09	2.399	443	12.5	236
$10^{-0.8}$	2.25	3.71	2.399	382	13.0	199
$10^{-0.6}$	2.66	6.80	2.410	291	11.8	146
$10^{-0.4}$	3.01	9.66	2.415	211	9.7	96
$10^{-0.2}$	3.25	11.49	2.415	154	7.6	61
$10^{0.0}$	3.33	11.49	2.427	116	5.9	38
$10^{0.2}$	3.18	9.88	2.443	92	4.5	23
$10^{0.4}$	2.91	6.45	2.466	78	3.5	14
$10^{0.6}$	2.51	1.98	2.518	69	2.7	9

Sweep seen from port 2:

I_{D2}/I_{D1}	$C_{ae}\ (fF)$	$C_{be}\ (pF)$	$f_0\ (GHz)$	$R_v\ (k\Omega)$	Q	S_n/S_{n0}
$10^{-1.0}$	0.06	1.86	2.399	38.15	12.5	209
$10^{-0.8}$	3.66	2.25	2.399	34.15	13.0	199
$10^{-0.6}$	6.71	2.67	2.410	26.90	11.8	167
$10^{-0.4}$	9.50	3.03	2.415	19.87	9.7	135
$10^{-0.2}$	11.24	3.28	2.415	14.60	7.6	110
$10^{0.0}$	11.09	3.37	2.427	11.09	5.9	92
$10^{0.2}$	9.27	3.24	2.443	8.82	4.5	79
$10^{0.4}$	5.57	3.00	2.466	7.47	3.5	71
$10^{0.6}$	0.75	2.63	2.518	6.68	2.7	65

Simulation C.10: .

Input parameters:

$L_1 = 50\ nm$	$L_2 = 100\ nm$	$I_{D1} = 250\ \mu A$
$(g_m/I_D)_1 = 16\ V^{-1}$	$(g_m/I_D)_2 = 15\ V^{-1}$	$I_{D2} = 750\ \mu A$
$W_1 = 8.47\ \mu m$	$W_2 = 28.6\ \mu m$	$fingerWidth = 206\ nm$

NMOS bias back-plane voltage: 2 V

Sweep seen from port 1:

$C_c\ (fF)$	$C_{ae}\ (fF)$	$C_{be}\ (pF)$	$f_0\ (GHz)$	$R_v\ (k\Omega)$	Q	S_n/S_{n0}
0	25.1	1.906	2.410	5.79	5.04	47
5	20.1	1.901	2.410	5.99	5.22	48
10	15.3	1.896	2.409	6.21	5.41	50
15	10.4	1.891	2.408	6.44	5.61	52
20	5.6	1.886	2.407	6.68	5.82	54

Sweep seen from port 2:

$C_c\ (fF)$	$C_{ae}\ (pF)$	$C_{be}\ (fF)$	$f_0\ (GHz)$	$R_v\ (\Omega)$	Q	S_n/S_{n0}
0	1.919	24.7	2.410	170	5.04	30
5	1.917	19.7	2.409	176	5.22	31
10	1.915	14.7	2.409	183	5.41	32
15	1.915	9.7	2.408	189	5.61	33
20	1.915	4.7	2.407	196	5.82	34

C.2 Simulations of Chapter 5

Simulation C.11: SGAI architecture, similar to the Simulation C.6, but trying to reach 50 Ω of equivalent series resistance.

Input parameters:

$L_1 = 100\ nm$	$L_2 = 100\ nm$	$I_{D1} = 1.89\ mA$
$(g_m/I_D)_1 = 23.5\ V^{-1}$	$(g_m/I_D)_2 = 10\ V^{-1}$	$I_{D2} = 170\ \mu A$
$W_1 = 356.26\ \mu m$	$W_2 = 2.491\ \mu m$	$fingerWidth = 206\ nm$

NMOS bias back-plane voltage: 2 V

Simulation C.12: .

Input parameters:

$L_1 = L_3 = 100\ nm$	$L_2 = 100\ nm$	$I_{D1} = 1.89\ mA$
$(g_m/I_D)_1 = (g_m/I_D)_3 = 16\ V^{-1}$	$(g_m/I_D)_2 = 15\ V^{-1}$	$I_{D2} = 170\ \mu A$
$W_1 = 353.26\ \mu m$	$W_2 = 2.491\ \mu m$	$fingerWidth = 206\ nm$

NMOS bias back-plane voltage: 2 V

Sweep input parameters:

$I_{D3}\ (mA)$	$W_3\ (\mu m)$	$R_L\ (\Omega)$	$C_{ae}\ (fF)$	$C_{be}\ (fF)$
0.100	18.746	1346	439	0.00
0.133	24.926	1009	428	0.00
0.178	33.166	757	412	0.00
0.237	44.290	567	390	0.00
0.316	59.122	426	362	0.00
0.422	78.898	319	324	0.00
0.562	105.060	239	274	0.00
0.750	140.080	179	207	0.00
1.000	186.842	135	117	0.00
1.100	205.588	122	81	0.00
1.200	224.334	112	45	0.00

Sweep results:

$I_{D3}\ (mA)$	$f_0\ (GHz)$	$R_{in}\ (\Omega)$	Q	S_n/S_{n0}	$NF\ (dB)$	$IIP3\ (dBm)$
0.100	2.466	73.1	0.96	0.645	13.1	−17.16
0.133	2.460	73.0	0.96	0.646	11.9	−17.16
0.178	2.460	72.9	0.96	0.645	10.8	−17.15
0.237	2.460	72.7	0.96	0.644	9.8	−17.14
0.316	2.455	72.5	0.96	0.645	8.7	−17.12
0.422	2.449	72.2	0.95	0.644	7.7	−17.11
0.562	2.443	71.8	0.95	0.644	6.8	−17.07
0.750	2.432	71.3	0.94	0.644	6.0	−17.03
1.000	2.421	70.6	0.93	0.644	5.3	−16.98
1.100	2.415	70.3	0.93	0.644	5.0	−16.97
1.200	2.410	70.1	0.93	0.644	4.8	−16.94

Simulation C.13: .

Input parameters:

$L_1 = L_3 = 100\ nm$	$L_2 = 100\ nm$	$I_{D1} + I_{D2} = 2.06\ mA$
$(g_m/I_D)_1 = (g_m/I_D)_3 = 16\ V^{-1}$	$(g_m/I_D)_2 = 15\ V^{-1}$	$I_{D3} = 1\ mA$
$R_L = 134.57\ \Omega$	$fingerWidth = 206\ nm$	$W_3 = 187\ \mu m$

NMOS bias back-plane voltage: 2 V

Sweep input parameters:

I_{D2}/I_{D1}	$I_{D1}\ (mA)$	$I_{D2}\ (mA)$	$C_{ae}\ (fF)$	$C_{be}\ (fF)$
0.080	1.907	0.153	32	0.00
0.090	1.890	0.170	117	0.00
0.100	1.873	0.187	198	0.00
0.133	1.818	0.242	510	0.00
0.178	1.749	0.311	877	0.00
0.237	1.665	0.395	1332	0.00
0.316	1.565	0.495	1853	0.00
0.422	1.449	0.611	2431	0.00
0.562	1.319	0.741	3090	0.00
0.750	1.177	0.883	3742	0.00
1.000	1.030	1.030	4369	0.00

Sweep results:

I_{D2}/I_{D1}	$f_0\ (GHz)$	$R_{in}\ (\Omega)$	Q	S_n/S_{n0}	$NF\ (dB)$	$IIP3\ (dBm)$
0.080	2.415	71.1	0.85	0.588	5.2	−16.75
0.090	2.421	70.6	0.93	0.644	5.3	−16.98
0.100	2.421	70.3	1.01	0.702	5.3	−17.19
0.133	2.427	68.6	1.30	0.977	5.7	−17.96
0.178	2.427	66.5	1.61	1.354	6.1	−18.70
0.237	2.421	64.2	1.98	1.972	6.7	−19.31
0.316	2.421	61.9	2.38	2.868	7.4	−19.86
0.422	2.415	59.7	2.79	4.164	8.3	−20.26
0.562	2.415	57.1	3.22	6.019	9.4	−20.68
0.750	2.410	55.2	3.63	8.652	10.6	−20.86
1.000	2.410	53.6	4.01	12.092	11.8	−21.01

References

[1] Alireza Saberkari, Saman Ziabakhsh, Herminio Martinez, and Eduard Alarcón. Active inductor-based tunable impedance matching network for RF power amplifier application. *Integration*, 52:301–308, Jan 2016. ISSN 01679260. doi: 10.1016/j.vlsi.2015.07.013.

[2] Ting Ma and Feng Hu. A wideband flat gain low noise amplifier using active inductor for input matching. *IEEE Transactions on Circuits and Systems II: Express Briefs*, 66(6):904–908, Jun 2019. ISSN 1549-7747, 1558-3791. doi: 10.1109/TCSII.2018.2872068.

[3] A. Saberkari, Sh Kazemi, V. Shirmohammadli, and M.C.E. Yagoub. gm-boosted flat gain UWB low noise amplifier with active inductor-based input matching network. *Integration*, 52:323–333, Jan 2016. ISSN 01679260. doi: 10.1016/j.vlsi.2015.06.002.

[4] Rishab Mehra, Vikash Kumar, and Aminul Islam. Reliable and Q-enhanced floating active inductors and their application in RF bandpass filters. *IEEE Access*, 6:48181–48194, 2018. ISSN 2169-3536. doi: 10.1109/ACCESS.2018.2868181.

[5] Behzad Razavi. The active inductor [a circuit for all seasons]. *IEEE Solid-State Circuits Magazine*, 12(2):7–11, 2020. doi: 10.1109/MSSC.2020.2987500.

[6] Chun-Lee Ler, A. A'ain, and A.V. Kordesch. CMOS active inductor linearity improvement using feed-forward current source technique. *IEEE Transactions on Microwave Theory and Techniques*, 57(8):1915–1924, Aug 2009. ISSN 0018-9480, 1557-9670. doi: 10.1109/TMTT.2009.2025426.

[7] Bernard D. H. Tellegen. The gyrator, a new electric network element. *Philips Res. Rept.*, 3(2):81–101, 1948.

[8] Francois Belmas. *Etude de structures innovantes pour la réalisation d'amplificateur RF faible bruit sans inductance et à très faible consommation.* PhD thesis, Université de Grenoble, Mar 2013. URL `https://tel.archives-ouvertes.fr/tel-00934813`.

[9] Grzegorz Szczepkowski. *Analysis and design of wideband voltage controlled oscillators using self-oscillating active inductors.* PhD thesis, National University of Ireland Maynooth, 2010. URL `http://mural.maynoothuniversity.ie/2670/`.

[10] Grzegorz Szczepkowski and Ronan Farrell. Noise and dynamic range of CMOS degenerated active inductor resonators. In *2009 European Conference on Circuit Theory and Design*, page 595–598, Aug 2009. doi: 10.1109/ECCTD.2009.5275052.

[11] Grzegorz Szczepkowski and Ronan Farrell. Analysis and design of oscillators based on low-voltage self-oscillating active inductors. In *IET Irish Signals and Systems Conference (ISSC 2010)*, page 135–140, Jun 2010. doi: 10.1049/cp.2010.0501.

[12] Risto Kaunisto. *Monolithic active resonator filters for high frequencies*. Helsinki University of Technology, Nov 2000. ISBN 978-951-22-5207-7. URL `https://aaltodoc.aalto.fi:443/handle/123456789/2300`. Accepted: 2012-02-13T12:10:53Z.

[13] Y.J. Shin and K. Bult. An inductorless 900 MHz RF low-noise amplifier in 0.9 um CMOS. In *Proceedings of CICC 97 - Custom Integrated Circuits Conference*, page 513–516, May 1997. doi: 10.1109/CICC.1997.606678.

[14] F.E. Van Vliet, F.L.M. Van Den Bogaart, J.L. Tauritz, and R.G.F. Baets. Systematic analysis, synthesis and realization of monolithic microwave active inductors. In *1996 IEEE MTT-S International Microwave Symposium Digest*, volume 3, page 1659–1662 vol.3, Jun 1996. doi: 10.1109/MWSYM.1996.512258.

[15] G. Leuzzi, V. Stornelli, L. Pantoli, and S. Del Re. Single transistor high linearity and wide dynamic range active inductor: Single transistor active inductor. *International Journal of Circuit Theory and Applications*, 43(3):277–285, Mar 2015. ISSN 00989886. doi: 10.1002/cta.1938.

[16] W.B. Kuhn, D. Nobbe, D. Kelly, and A.W. Orsborn. Dynamic range performance of on-chip RF bandpass filters. *IEEE Transactions on Circuits and Systems II: Analog and Digital Signal Processing*, 50(10):685–694, Oct 2003. ISSN 1558-125X. doi: 10.1109/TCSII.2003.818364.

[17] G. Efthivoulidis, L. Toth, and Y.P. Tsividis. Noise in Gm-C filters. *IEEE Transactions on Circuits and Systems II: Analog and Digital Signal Processing*, 45(3): 295–302, Mar 1998. ISSN 1558-125X. doi: 10.1109/82.664235.

[18] M. Ismail, R. Wassenaar, and W. Morrison. A high-speed continuous-time bandpass VHF filter in MOS technology. In *1991 IEEE International Symposium on Circuits and Systems (ISCAS)*, pages 1761–1764 vol.3, 1991.

[19] Yue Wu, M. Ismail, and H. Olsson. A novel CMOS fully differential inductorless RF bandpass filter. In *2000 IEEE International Symposium on Circuits and Systems (ISCAS)*, volume 4, pages 149–152 vol.4, 2000.

[20] Franco Di Paolo. *Networks and devices using planar transmission lines*. CRC Press, 2000. ISBN 9780849318351.

[21] A. A. Abidi. Noise in active resonators and the available dynamic range. *IEEE Transactions on Circuits and Systems I: Fundamental Theory and Applications*, 39(4):296–299, April 1992. doi: 10.1109/81.129457.

[22] Marcio Cherem Schneider and Carlos Galup Montoro. *CMOS Analog Design Using All-Region MOSFET Modeling*. Cambridge University Press, 2010. doi: 10.1017/CBO9780511803840.

[23] Rahul Sarpeshkar, Tobi Delbruck, and Carver Mead. White noise in MOS transistors and resistors. *IEEE Circuits and Devices Magazine*, 9:23–29, 1993.

[24] Yannis Tsividis and Colin McAndrew. *Operation and modeling of the MOS transistor; 3rd ed.* Oxford series in electrical and computer engineering. Oxford Univ. Press, 2011.

[25] David M. Pozar. *Microwave engineering*. Wiley, 4th ed edition, 2012. ISBN 9780470631553. OCLC: ocn714728044.

[26] B. Razavi. *Design of Integrated Circuits for Optical Communications*. McGraw-Hill Series in Electrical and Computer Engineering. McGraw-Hill, 2003. ISBN 9780072822588. URL https://books.google.com.uy/books?id=vysQEjz0UicC.

[27] C. Fenouillet-Beranger, P. Perreau, S. Denorme, L. Tosti, F. Andrieu, O. Weber, S. Barnola, C. Arvet, Y. Campidelli, S. Haendler, R. Beneyton, C. Perrot, C. de Buttet, P. Gros, L. Pham-Nguyen, F. Leverd, P. Gouraud, F. Abbate, F. Baron, A. Torres, C. Laviron, L. Pinzelli, J. Vetier, C. Borowiak, A. Margain, D. Delprat, F. Boedt, K. Bourdelle, B.-Y. Nguyen, O. Faynot, and T. Skotnicki. Impact of a 10nm Ultra-Thin BOX (UTBOX) and Ground Plane on FDSOI devices for 32nm node and below. In *2009 Proceedings of the European Solid State Device Research Conference*, page 89–92. IEEE, Sep 2009. ISBN 978-1-4244-4351-2. doi: 10.1109/ESSDERC.2009.5331588. URL http://ieeexplore.ieee.org/document/5331588/.

[28] Jack Ou and Pietro M. Ferreira. Design considerations of CMOS active inductor for low power applications. *Analog Integrated Circuits and Signal Processing*, 94(3):347–356, Mar 2018. ISSN 0925-1030, 1573-1979. doi: 10.1007/s10470-017-1059-3.

[29] Toru Masuda and Hiroshi Mori. Active resonant circuit with resonant-frequency tunability, Nov 2010. URL https://patents.google.com/patent/US7843287B2/en.

[30] Chao-Chih Hsiao, Chin-Wei Kuo, Chien-Chih Ho, and Yi-Jen Chan. Improved quality-factor of 0.18-um CMOS active inductor by a feedback resistance design. *IEEE Microwave and Wireless Components Letters*, 12(12):467–469, 2002. doi: 10.1109/LMWC.2002.805931.

[31] Ariel Luzzatto and Motti Haridim. *Wireless Transceiver Design: Mastering the Design of Modern Wireless Equipment and Systems*. John Wiley and Sons, Ltd, Nov 2016. ISBN 978-1-119-31565-0. doi: 10.1002/9781119315650. URL http://doi.wiley.com/10.1002/9781119315650.

[32] D.K. Shaeffer and T.H. Lee. A 1.5-V, 1.5-GHz CMOS low noise amplifier. *IEEE Journal of Solid-State Circuits*, 32(5):745–759, 1997. doi: 10.1109/4.568846.

[33] Vadim V Ivanov and Igor M Filanovsky. *Analog Circuit Design with Structural Methodology*. Kluwer Academic Publishers, 2004. ISBN 1-4020-2517-3.

[34] Paul G. A. Jespers and Boris Murmann. Calculation of MOSFET distortion using the transconductance-to-current ratio (gm/ID). In *2015 IEEE International Symposium on Circuits and Systems (ISCAS)*, page 529–532. IEEE, May 2015. ISBN 978-1-4799-8391-9. doi: 10.1109/ISCAS.2015.7168687. URL http://ieeexplore.ieee.org/document/7168687/.

This page was intentionally left blank.

Index of tables

This page was intentionally left blank.

Index of figures

This is the last page.
Compiled on 2022-07-01.
http://iie.fing.edu.uy/